공학박사 학위논문

Minimally Invasive Medical Procedures Utilizing Adhesion Property of Multifunctional Nanoparticles

다기능성 나노입자의
접착 성질을 활용한
최소침습시술의 구현

2018년 2월

서울대학교 대학원
화학생물공학부
신 광 수

Abstract

Minimally Invasive Medical Procedures Utilizing Adhesion Property of Multifunctional Nanoparticles

Kwangsoo Shin

School of Chemical and Biological Engineering

The Graduate School

Seoul National University

Minimally invasive procedures are replacing a variety of open surgeries as medical technologies advance. Thanks to the limited incision technique, many patients have been able to avoid suffering from inflammation, complications, and long recovery time. Highly sensitive imaging modalities and probes can help clinicians to identify the operation site, while tissue adhesives and sealants can promote wound closure. The cell-based therapy is considered as an alternative to surgery or organ transplantation, in which the cells are labeled with imaging probes to enable tracking and visualization of their therapeutic function. Nanoparticles are the ideal candidates for imaging probes that offer high contrast enhancement and biocompatibility. Modifying the surface of nanoparticles to enhance their adhesion to cells and biological tissues allows efficient cell labeling and closure of internal wound for therapeutic purposes.

Following the Introduction chapter, Chapter 2 describes the development of multifunctional adhesives for minimally invasive procedures. By modifying their surface with silica, tantalum oxide nanoparticles can strongly adhere to biological tissues and provide contrast enhancement effects for real-time imaging modalities including

X-ray fluoroscopy, X-ray computed tomography, ultrasonography, and fluorescence imaging. The thin silica coating allows the tantalum oxide nanoparticles to be dispersed stably and to adhere to substrates with a force that is comparable to clinically employed cyanoacrylate-based adhesives. Moreover, these nanoparticles overcome the limitations of cyanoacrylate such as cytotoxicity and induction of inflammation, and are thus more suitable for intracorporeal use in minimally invasive procedures. Real-time image-guided procedures, immediate sealing of puncture wounds in liver and marking of tumor, are demonstrated using surface-modified tantalum oxide nanoparticles in animal experiments.

In Chapter 3, I present a simple method for efficient labeling of therapeutic cells with multifunctional nanoparticles. Disulfide bonds in cell membrane proteins are reduced to active thiol groups, and the mesoporous silica nanoparticles (MSN) with maleimide group are used to coat mammalian cells via chemical conjugation. The fluorophore-labeled mesoporous silica nanoparticles allow tracking of the coated cells and their visualization were done by intra-vital microscopy. Drug molecules can be loaded into the mesoporous silica nanoparticles for local delivery through cell implantation. Furthermore, the activities of

injected cells can be enhanced via conjugation of immunosuppressant-loaded MSNs and polymers to overcome innate immune rejection.

Keywords: nanoparticle, biomedical application, minimally invasive procedures, tissue adhesive, cell surface engineering

Student number: 2011-22921

Contents

List of Schemes

List of Tables

List of Figures

Chapter 1. Introduction:

Cell- and Tissue-Adhesive Nanoparticles, and their Applications to Minimally Invasive procedures

1.1 Introduction

Nanoparticles (NPs) have been extensively studied for various biomedical applications. Their applicability to various biomedicine fields is broadened by unique physical properties that are attributable to their inorganic crystal structure, large surface area, and extremely small sizes.[1,2] NPs are particularly useful for cancer diagnosis and therapy: they can target tumors due to their enhanced permeation and retention (EPR) effect and drug-loading capacity.[3] Their unique physical properties ensure a strong signal for an efficient contrast effect in cancer imaging.[4-9] The surface structure of NPs can be modified by functional molecules. For example, attaching fluorescent dyes or chelating ligands confers an additional contrast effect, whereas conjugation with specific

ligands or antibodies provides a targeting capability. [10,11] NPs can be designed to have both diagnostic and therapeutic functions[12-15] for the applications in cancer treatment. Exploitation of the catalytic nanomaterials allows the modulation of reactive oxygen species and the control of cell signaling, enabling their applications to regenerative medicine. [16-19]

One of the biomedical applications of multifunctional NPs is minimally invasive procedure.[20,21] Strong contrast enhancement with high sensitivity enables the visualization of the NPs distributed throughout the body, providing accurate spatiotemporal information for minimally invasive procedures.[22] In addition, their efficient thermal conversion of light energy as well as inducible drug release are useful for the treatment of remote areas.

Many studies have examined the interface between biological environment and NP surface to maximize the applicability of NPs in the medical applications. NPs form colloids of various materials in dispersive media, while physiological environments consist of a variety of biological molecules in water. Interactions among them can be understood in terms of adhesion and adsorption. Many recent studies

investigated the interactions between nanomaterials and serum proteins. NPs encounter serum proteins upon systemic administration, and adsorption occurs before NPs reaching receptors in target tissues. Cellular uptake is governed by the interaction/adhesion of NPs to cell membrane proteins.[23] The biodistribution of NPs depends on their interaction with immune cells, that is, their uptake by macrophages or binding to receptors in target tissues. Therefore, optimization of the adhesion and adsorption interactions between the NP surface and biological molecules, cells, and tissue is necessary to broaden the applications of nanomaterials in biomedicine, including minimally invasive procedures.

1.2 Nanomaterial adhesion in biological systems

Nanomaterial surface has a much higher free energy than that of bulk material. Therefore, the large surface area of NPs is useful for selective adsorption of biomolecules as NPs contact biological fluids.[24] Although the stealth effect of NPs can be derived from the modification of their surface with polymers such as polyethylene glycol (PEG). The active NP surface is usually covered with biomolecules that spontaneously adhere and alter the surface properties of the NPs.[25] Thus, the adhesion of biomolecules onto the NP surface influences the interaction between NPs and cells or administered tissues. The nonspecific adhesion of biomolecules due to high free energy can be modulated by coating NPs with polymers,[26] or transformed into a specific interaction by functionalizing of the NP surface with specific targeting ligands or proteins.

High free energy of the NP surface can promote NP adsorption onto cell surface and efficient cellular uptake, which are influenced by various factors including particle size, morphology, surface charge, and surface modification.[25] A recent study reported that surface free energy can be exploited to increase NP adhesion to biological tissues.[27] In this

section, I describe factors that influence the interactions between NPs and cells and tissues. In this context, I also discuss various applications that depend on the modulation of interactions between NPs and biomolecules.

1.2.1 Adhesion of nanoparticles on cell surface

Adhesion of molecules to substrate or between distinct substrates is a complex phenomenon because it often involves combinations of multiple interactions: molecular adsorption, electromagnetic attraction, diffusional entanglement, and mechanical force.[28,29] Surface contamination, substrate roughness, and friction are also factors that affect the adhesion properties. In the case of the adhesion between biological molecules and NPs, however, the adhesion properties of NPs are governed by fewer mechanisms. Adhesion strength is minimally affected by mechanical force due to the small size of NPs. The adhesion derived from of the diffusion of polymeric chains into substrates, which polymer-based adhesives have, can be excluded in colloidal NP-based adhesives. Colloidal NPs interact with biomolecules only through hydrophobic/Coulombic interactions and hydrogen bonding.

1.2.2 NP attachment to cells

The interaction between NPs and cells is governed by the NP surface characteristics such as surface charge, polymer density, and nature of the inorganic NPs.[30] Because NPs are mainly internalized into the cells through endocytosis;[31] their initial adhesion or binding to cells is critical for this process (**Figure 1.1**). The rate of NP uptake by cells depends on the amount of NPs that adhere to the cell surface.[32] The adhered NPs can enter cells through energy-dependent intake or energy-independent insertion. Endocytosis includes clathrin- and caveolae-mediated pathways, phagocytosis, and macropinocytosis.[23]

The surface characteristics of NPs play a key role in the interaction between NPs and cells. For biomedical applications, NPs must be well dispersed in physiological media such as water or saline at neutral pH. An electrical double layer and electrostatic repulsive force are frequently used to achieve colloidal stability. Carboxylates, amine, sulfate, or zwitterionic ligands contribute to the stable dispersion of NPs. Polymers are also frequently-used coating materials to create a sterically repulsive layer on NP surface. PEG-based non-ionic surfactants are used as stabilizing agents for NPs in aqueous media.[33-40]

The distinct electrostatic and electrodynamic properties of NPs conferred by surface potential and capping ligands modulate their interactions with cells. Most animal cells have a negatively charged surface that preferentially attracts positively charged NPs. The effective surface charge density of NPs determines their electrostatic interaction with cells (**Figure 1.2**);[41] this applies to quantum dots and gold, silica, and magnetic NPs.[42] Atomic force microscopy observations have confirmed that positively charged NPs can adhere to the cellular surface.[44] Although attachment of serum proteins can change their zeta potential from −40 to −20 mV [43], this does not affect NP internalization (**Figure 1.3**).[41] Cytotoxicity is also influenced by interaction of NPs with the cell membrane during uptake.[45] Neutral or negatively charged NPs can also attach to the cell surface in the absence of PEG or serum in the medium.[46]

Although generally positively charged NPs adhere to the cell membrane, this does not apply to the neuronal surface, which attract only negatively charged NPs at the synaptic cleft. This is because neurons in the resting state have a positively charged outer surface. Depolarization creating an action potential transiently alters the counterions surrounding negatively charged NPs, resulting in a stable electrostatic interaction

between the negatively charged NPs and the positively charged outer surface of the neuronal membrane.[47]

Target-specific biomolecules can also modulate NP adhesion and internalization. For instance, antibodies or their fragments, targeting peptides, and folic acid, which can interact with the specific receptors, can enhance NP adhesion to the cell surface.[48] Although targeting ligands alter the rate of NP internalization, serum proteins can non-specifically adhere to the NP surface, forming a protein corona that may block the active targeting moiety[49] and NP adsorption to the cell membrane. The amount of NPs that adhere to cells can be altered by incubation in serum-free medium, as observed for silica and polystyrene NPs.[46]

Chemical modification of the NP surface can promote adhesion of NPs to cells. Thiol groups on the T cell, B cell, and hematopoietic stem cell surface enable attachment of liposome NPs to the cell surface through a strong covalent bonding (**Figure 1.4**).[50]

The attraction of the NPs with cells can control the adhesion of cells onto substrate by coating plain substrate with NPs. Such an approach has been used in the preparation of a solid scaffold for tissue

regeneration; additionally, various biocompatible nanomaterials have been incorporated onto implant surfaces.[51] NP adhesion onto the cell surface can also be used as nanostickers that promote the formation of cell-NP hybrid aggregates. The cells adhere to each other through homotypic interactions between membrane proteins known as cadherins; cells lacking cadherin form cell clusters that are promoted by NPs.[52]

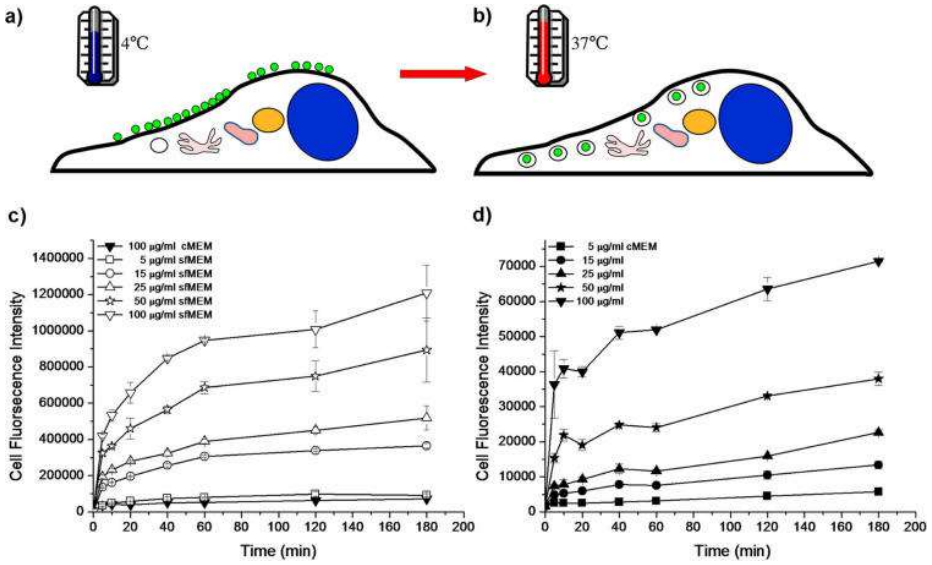

Figure 1.1. Adhesion of 40-nm phosphatidyl serine-COOH NPs onto the A549 cell membrane, as determined by flow cytometry. (a, b) Schematic illustration of the procedures used to measure NP adhesion to the cell membrane. (c, d) Experimental data showing the amount of adsorbed NP as a function of time under serum-free conditions (c) and in complete medium (d).[46]

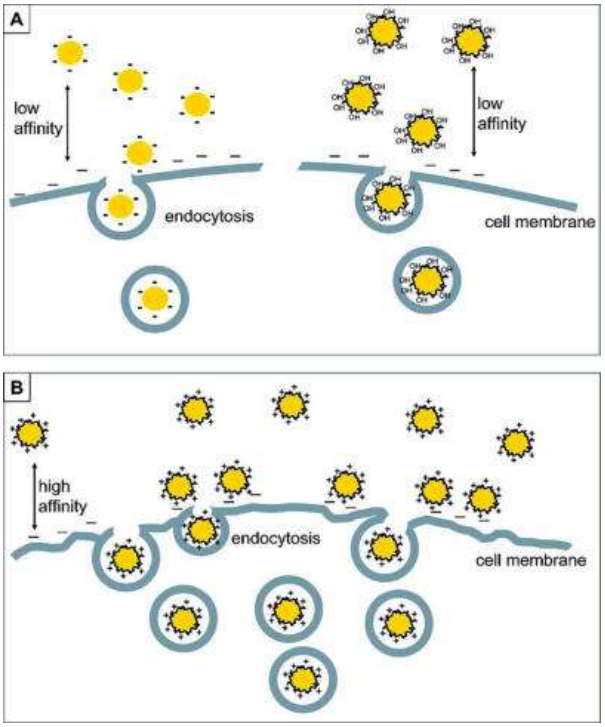

Figure 1.2. Schematic illustration of the interactions between cells and NPs with different types of surface charge. (A) Neutral and negatively charged NPs. (B) Positively charged NPs.[42]

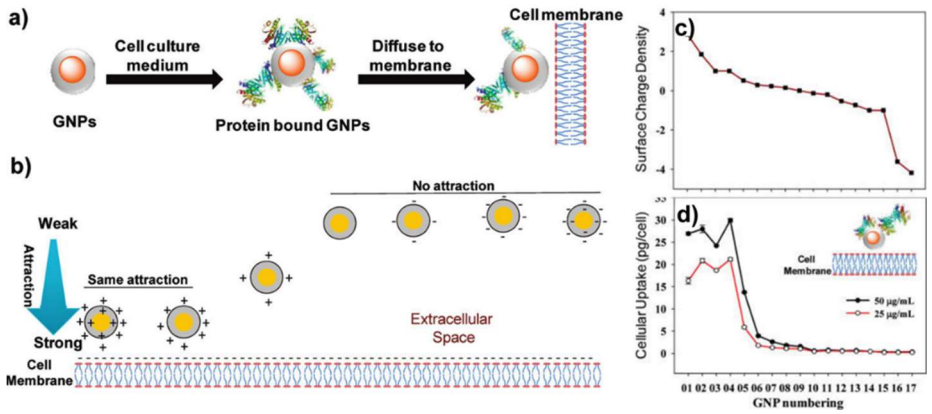

Figure 1.3. Electrostatic attraction between NPs and cells. (a, b) Schematic illustration depicting how protein-bound gold nanoparticles (GNPs) attach to cells. (c) Surface charge density (SCD) based on ligand quantification. (d) Cellular uptake of the GNP array by HeLa cells with a continuous change in SCD. Data represent ± standard deviation.[41]

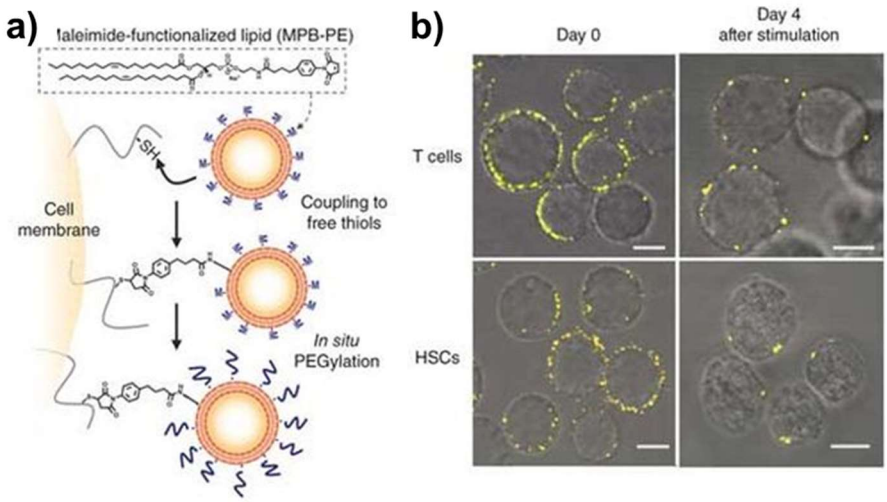

Figure 1.4. Stable conjugation of NPs to the surface of T cells and hematopoietic stem cells (HSCs) via cell-surface thiols. (a) Schematic illustration of maleimide-based conjugation to cell surface thiols. (b) Confocal micrographs of clusters of differentiation 8+ effector T cells and Sca-1+c-Kit+ HSCs immediately after conjugation with fluorescent 1,1-dioctadecyl-3,3,3,3-tetramethylindodicarbocyanine-labeled multilamellar lipid NPs (left) and after 4 days of in vitro expansion (right). Scale bars = 2 μm.

1.2.3 Adhesion of NPs to biological tissue

NP interactions with biological tissue are chemically and physically complex. Intravenously delivered NPs are removed from the blood via renal clearance, uptake by macrophages, and the reticuloendothelial system. The interaction of NPs with biological tissue occurs within a confined environment; however, the adherence of biomolecules to NPs due to high free energy prevents the direct observation of this interaction, as confirmed by studies on the interaction of NPs in hydrogel, which has similar properties to biological tissue.[53] Interestingly, it was reported that NP solution can act as an adhesive for hydrogels and biological tissues.[27] For instance, strong, rapid adhesion between two hydrogels was achieved at room temperature by spreading a droplet of a NP solution on the surface of one gel and then bringing the other gel into contact with the droplet (**Figure 1.5**). Adsorption of NPs onto the polymer gel can connect polymer chains. In addition, pieces of calf liver can be glued together using a silica NP solution; furthermore, NP solution has been used as a hemostatic agent for bonding of medical devices,[54] since it can adhere to the wound without dislocating or blocking the tissues, unlike sutures or polymeric adhesives (**Figure 1.6**). This reduces trauma to soft tissues and avoids the inflammation induced

by or toxicity associated with polymeric cross-linkers. The NP adhesion strength can be increased by enlarging the NP surface area. For example, mesoporous silica NPs with a pore diameter of 6.45 nm have 35 J/m^2 of adhesion energy, which is five times higher than that of non-porous silica NPs even at low concentrations.[55]

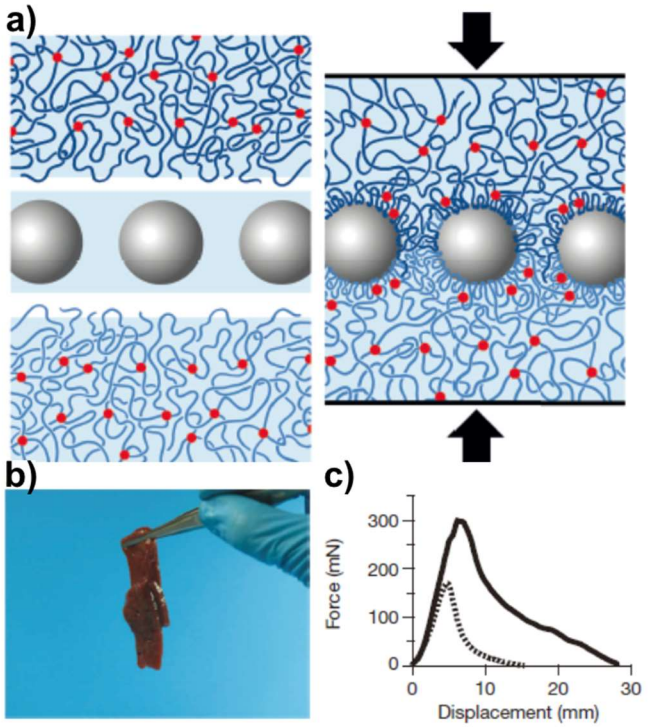

Figure 1.5. NP solution as an adhesive for hydrogels and biological tissues. a) Schematic illustration of gluing swollen polymer networks using NPs. b) Gluing of biological tissues with silica NPs. Two pieces of calf liver were glued together by spreading TM-50 nanosilica solution between them and then pressing them together by using the fingers. c) Normalized force-displacement curves for lap joints made of ribbons of cut calf liver glued together with TM-50 silica solution.

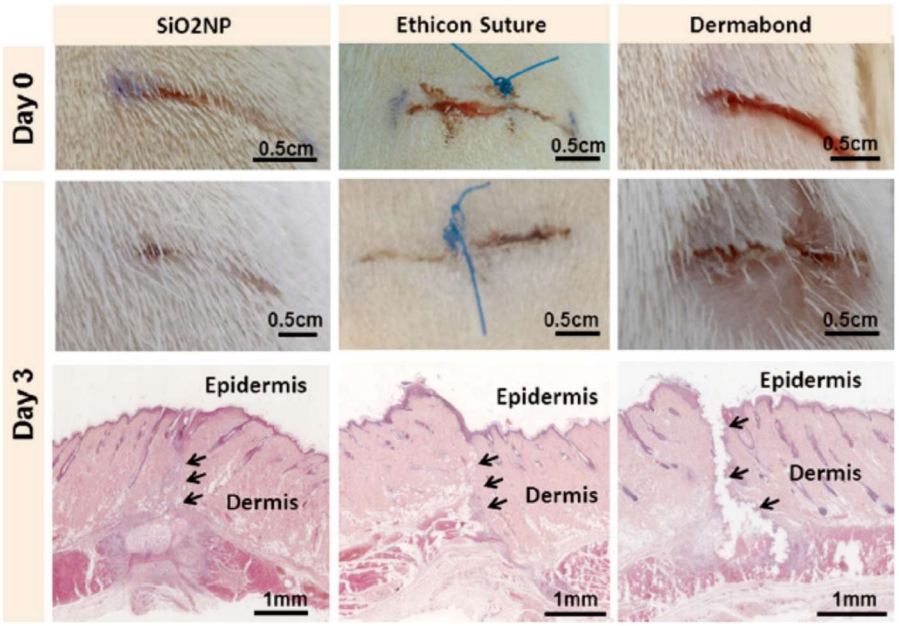

Figure 1.6. Tissue repair in a full-thickness dorsal skin wound by SiO_2NP nanobridging, suturing, or gluing with cyanoacrylate glue in a rat model. A drop of SiO_2 NP solution was placed on the wound edge with a brush and the two wound edges were gently pressed into contact for about 1 min. The other wounds were closed with a non-resorbable suture (Ethicon 4/0) or 2-octyl cyanoacrylate (Dermabond).[54]

1.3 Application of NPs in minimally invasive procedures

1.3.1 Minimally invasive procedures

Incisions made in open surgery leave large wounds that are painful and require a long recovery time. The limited size of the incision during minimally invasive surgery reduces healing time as well as pain and risk of infection.[56] Minimally invasive approaches are used for endovascular aneurysm repair, embolization, and chemo-embolization in interventional radiology.[57] Remote ablation or treatment of target tissue can be achieved using an instrument generating gamma rays, laser light, or high-intensity ultrasound; these procedures are non-invasive since they do not involve injury to the skin or the introduction of foreign materials. Thermal ablation, photodynamic therapy, high-intensity focused ultrasound, and radiotherapy are also widely used non-invasive procedures.[58-61]

Stem cell therapy is used to treat congenital diseases or to enhance regeneration of damaged tissues, and can replace conventional open surgeries. Providing therapeutic cells with an appropriate scaffold can contribute to the repair of structural damage in target tissue without pain and risks associated with surgery.[62-65]

A minimally invasive procedure typically involves the use of an endoscope, interventional medical modalities, and remote manipulation of instruments. Imaging modalities to visualize damaged tissues or lesions and appropriate agents to enhance the contrast between target and normal tissues are also required. Diagnostic pre-operative, interventional intra-operative, and post-operative imaging for tracking and follow-up is typically performed.[66] Since minimally invasive procedures are carried out in a limited space and with a small-sized incision, suitable medical materials including needle, stents, and markers are required. Moreover, internal soft tissue cannot be sutured or stapled in the limited space; only an adhesive on the incision can close the wound created during the procedure.[67,68]

1.3.2 NPs in minimally invasive procedures

Nanomaterials play important roles in imaging by delivering large imaging payloads, improving sensitivity, providing multiplexing capacity, and allowing modularity in design.[69] The magnetic, optical, acoustic, and X-ray-attenuating properties of NPs allows them to be combined with minimally invasive procedures (**Figure 1.7**).[70,71]

Various nanomaterials, including upconverting lanthanides, iron oxide, tantalum oxide, gold, and silica NPs, exhibit contrast enhancement capacity along with high sensitivity and biocompatibility.[72-74] The clinical application of NP-based contrast agents has recently increased following U.S. Food and Drug Administration approval. Minimally invasive procedures using NPs are being developed in various fields.[75]

Biocompatibility and contrast enhancement can improve minimally invasive procedures by allowing accurate positioning and tracking of physiological movement. Moreover, conversion of light or sound energy into thermal energy using NPs can increase the efficacy of ablation therapies. Wound closure adhesives consisting of multifunctional NPs stimulate rapid recovery while minimizing inflammation and complications. The endoscope system combined with theranostic NPs allows the clinical application of fluorescence imaging and surface-enhanced Raman spectroscopy (SERS) for molecular imaging of gastrointestinal tract organs.

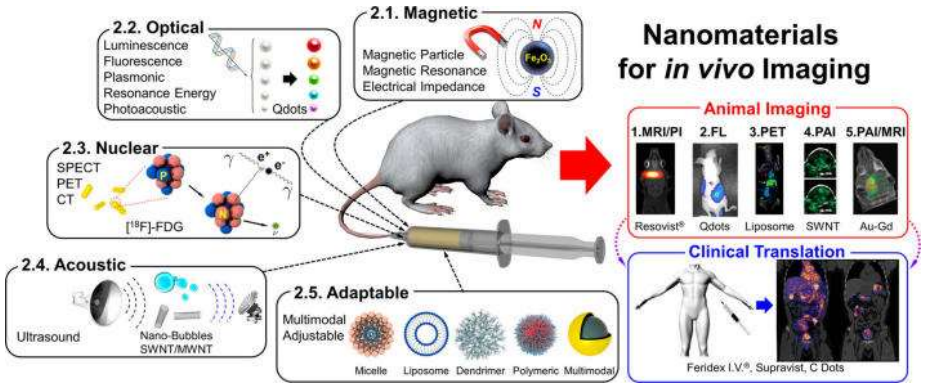

Figure 1.7. Nanomaterials for in vivo imaging. Schematic illustration of magnetic, optical, nuclear, acoustic, and adaptable nanomaterials for injection into living organisms.[69]

1.3.3 NPs for tracking therapeutic cells

Cell-based therapies including immunotherapy and stem cell therapy (SCT) are novel therapeutic approaches in oncology. Limitations to SCT include cell death, contamination by undifferentiated cells, and cell delivery to non-targeted areas. Imaging can enhance the efficacy of SCT by enabling the proper delivery of cells and the monitoring of cell fate over the short and long terms.[76]

Imaging is critical for determining the location and quantity of stem cells during transplantation as well as their redistribution during tissue repair.[77] Tracking implanted cells requires their labeling prior to administration. Cells can be genetically modified to express fluorescent protein so that they can be distinguished within tissue, but these cells can be tracked only by fluorescence imaging. Moreover, cellular activity is lost during transfection and exogenous protein expression. NP labeling provides other imaging modalities including magnetic resonance imaging (MRI), photoacoustic, and computed tomography (CT). MRI exhibits excellent resolution, soft tissue contrast, and high sensitivity; cell tracking by MRI was first reported nearly a decade ago and single-cell imaging is now possible.[78-82]

Magnetosome-like NPs have been prepared by coating PEG-phospholipid on ferromagnetic iron oxide nanocubes (FIONs). Pancreatic islet grafts and their rejection have been imaged using FIONs on a 1.5 T clinical MRI scanner.[83] Silica-coated gold nanorods can serve as a contrast agent for photoacoustic imaging and were used for quantitation of mesenchymal stem cells (MSCs) in rodent muscle tissue (**Figure 1.8**).[84]

The positively charged NP surface is associated with a higher uptake ratio and efficient labeling. A simple method for rendering human MSCs sufficiently radiopaque via complexation of 40 nm citrate-stabilized gold nanoparticles (AuNPs) with poly-L-lysine, and rhodamine B isothiocyanate is shown in **Figure 1.9**. AuNPs-labeled human MSCs can be clearly visualized *in vitro* and *in vivo* using a micro-CT scanner.[85] Using a similar approach, human MSCs have been labeled with positively charged Prussian blue NPs and visualized by photoacoustic imaging (**Figure 1.10**).[86]

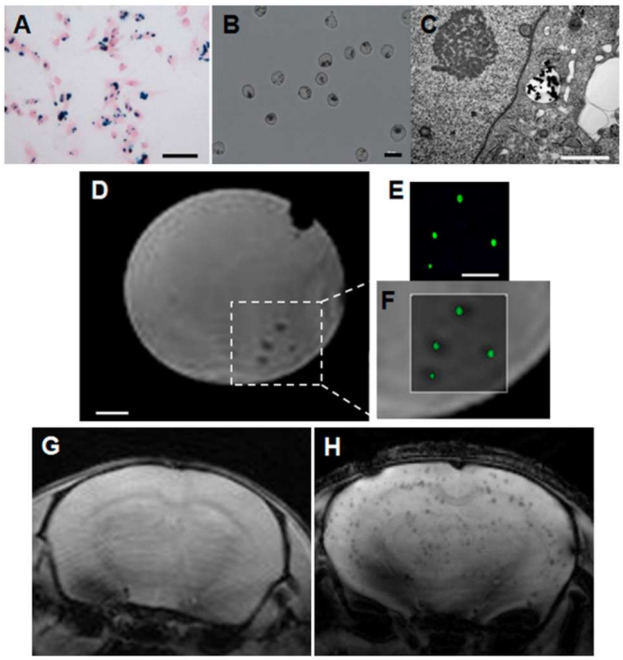

Figure 1.8. Iron oxide NPs for cell tracking. Cellular uptake of FIONs and MR images of single cells. (A) Prussian blue staining of MDA-MB-231 breast cancer cells. (B) Trypsinized MDA-MB-231 cells; FIONs are visible as dark spots within the cells. (C) Transmission electron micrograph of FIONs trapped in an intracellular vesicle. (D) MR image of four labeled cells sandwiched between two Gelrite layers. (E) Fluorescence image of cells stained with calcein-AM. (F) Merged image of corresponding regions in panels (D) and (E).[84]

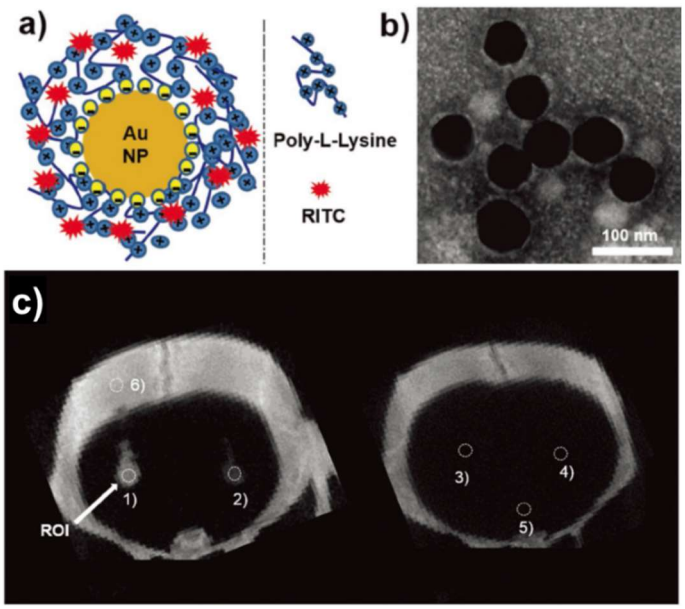

Figure 1.9. Positively charged AuNPs for labeling human MSCs. a) Schematic illustration and b) transmission electron micrograph of 40-nm core-diameter AuNP–poly-L-lysine–rhodamine B isothiocyanate complexes. c) In vivo micro-CT images of AuNP–poly-L-lysine-rhodamine B isothiocyanate-labeled human MSCs after 30 min of transplantation into the striatum.[85]

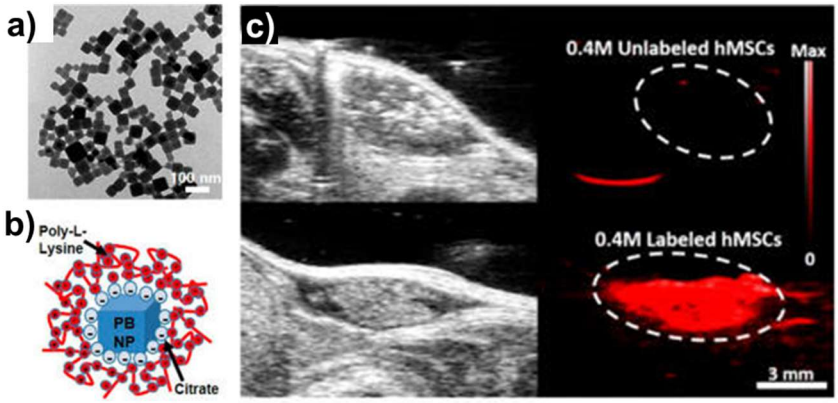

Figure 1.10. Positively charged Prussian blue nanocomposite for cell tracking by photoacoustic imaging (a) Transmission electron micrograph of Prussian blue NPs. (b) Schematic illustration of PB−poly-L-lysine nanocomplex. Negatively charged, citrate-stabilized Prussian blue NPs are electrostatically complexed with positively charged poly-L-lysine. (c) B-mode ultrasound (gray scale) and photoacoustic (red) images of unlabeled (top) and labeled (bottom) human MSCs subcutaneously injected into nude mice.[86]

1.3.4 Enhanced remote ablation therapy using NPs

Among non-invasive procedures, ablation therapy for tumor treatment [87] involves the delivery of incident energy through X-ray, laser, or focused ultrasound to damage tumor tissue.[88,89] Imaging and tracking of the tumor tissue is necessary to ensure effective ablation. Various contrast effects of NPs have been exploited to visualize tumors in an in vivo condition.[90-92]

The therapeutic effect of ablation therapy can be enhanced by using energy-converting nanomaterials, which are delivered to tumor tissue prior to X-ray or near-infrared (NIR) laser irradiation. The selective ablation of target tissue prevents damaging normal tissues. In photothermal therapy, gold nanorods absorb NIR light and the resultant thermal energy can destroy tumors.[93] Various materials, including carbon nanotubes, FeS NPs, Cu_2S NPs, graphene oxide, and nanoshell-structured materials, can be used for photothermal therapy.[92,94].

Multifunctional NPs can enhance the efficiency of ablation therapy using high-intensity focused ultrasound (HIFU). Converting ultrasound energy into regional hyperthermia can induce tissue necrosis. However, the energy rapidly dissipates with increasing penetration depth,

and the thermal energy can damage tumor tissue only when the ultrasound beam is focused. Multifunctional NPs loaded with perfluorohexane can overcome these limitations by providing the spatiotemporal specificity to the targeting and by enhancing the conversion of ultrasound into the thermal energy.[95-98] Gold nanoshelled lipid perfluorocarbon magnetic nanocapsules, mesoporous silica-encapsulating AuNPs, and magnetite-perfluorocarbon-loaded hybrid vesicle are the examples of theranostic NPs designed for image-guided HIFU treatment.[95-98]

Magnetic NPs with ferromagnetic properties can be used for another type of ablation therapy. When alternating magnetic waves are applied to ferromagnetic NPs, the particles emit heat during relaxation. Since attenuation of magnetic fields in the body is negligible compared to that of visible or NIR light waves and does not result in the ionization of biological molecules, only tissue with magnetic NPs are ablated by magnetic thermal therapy or hyperthermia. Iron oxide and metal ferrite NPs are the main materials used for this treatment (**Figure 1.11**).[74,99]

Reactive oxygen species (ROS) generated by photocatalytic reaction of NPs also enhance the efficiency of photodynamic therapy.

Increased ROS levels induce apoptosis of cancer cells, thereby decreasing tumor volume. Titanium dioxide and graphene oxides have photocatalytic properties in the absence of photodynamic drugs.[100,101] Materials with sonocatalytic effects generate ROS by absorbing sound energy.[102-104] The efficacy of radiation therapy using X- or gamma rays can be enhanced by NPs based on their contrast effect and scintillation properties. Several scintillating NPs are known to convert the high energy of X- or gamma rays into ultraviolet–visible light, enabling the combination of photodynamic and radiation therapies.[91,105,106] NPs for remote ablation therapies can also be used for diagnostic purposes. These multifunctional theranostic agents allow minimally invasive procedures to be efficiently carried out.

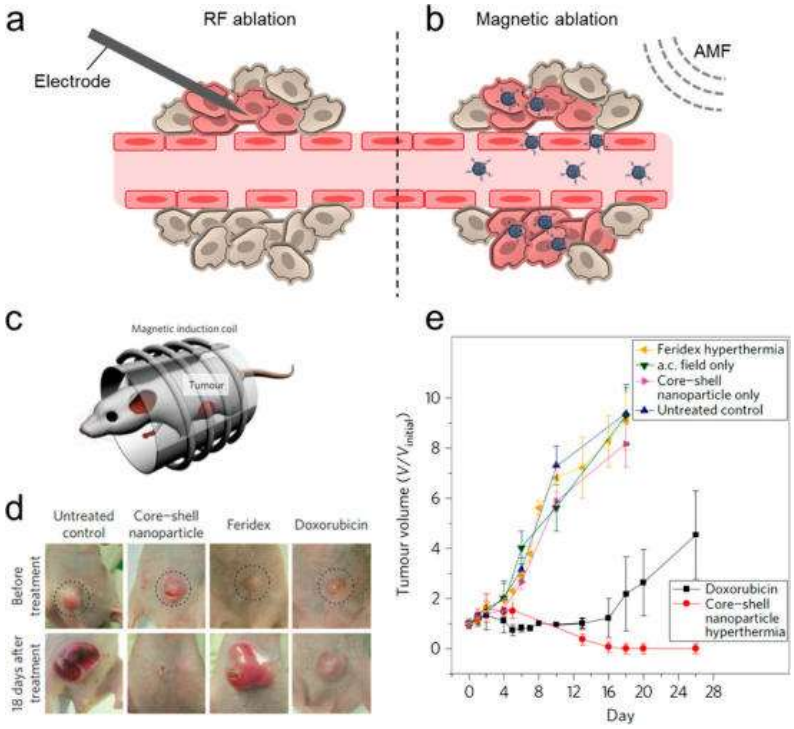

Figure 1.11. Remote ablation therapy using magnetic NPs. (a) Radiofrequency (RF) ablation. (b) Magnetic thermal ablation with alternating magnetic field (AMF) (c) Schematic illustration of magnetic in vivo hyperthermia treatment to a mouse. (d) Nude mice xenografted with cancer cells (U87MG) before (upper row, dotted circle) and 18 days after (lower row) treatment. (e) Plot of tumor volume vs. time after treatment.[99]

1.3.5 NP-based wound closure materials

Conventional polymeric tissue adhesives usually require complex *in vivo* control of polymerization or crosslinking. They may also be toxic, weak, or ineffective in an aqueous environment.[67] These disadvantages limit their usage for closing wounds inside the body. Nanotechnology has improved the properties and function of tissue adhesives for clinical use.[107] For example, NP solutions are used as adhesives and hemostatic materials to strongly bind the biological tissues together and stop the internal bleeding without the need for in situ polymerization. Surface modification of NPs can enhance their adsorption to tissues.[27,54] Silica NPs are highly effective for wound closure owing to their strong capacity for tissue adhesion; other metal oxide NPs including borate and bioactive glass, ceria and iron oxide NPs have also been investigated for their potential as adhesive materials.[108] Bioactive glass exhibits the strongest adhesion, whereas the iron oxide is comparable to silica and has been successfully used to stimulate the closure of a full-thickness skin incision. Iron oxide NPs can also serve as imaging probes to monitor the wound healing (**Figures 1.12**).[54]

Tissue adhesives with antibacterial properties can be generated

through incorporation of antimicrobial NPs. Also hemostatic bioadhesives can be engineered by encapsulating the NPs into polymeric adhesives. Titanium dioxide and zinc oxide NPs have antimicrobial activities. By exploiting these properties along with their capacity for adsorption to hydrogel and soft tissue, NPs can serve as wound closure adhesives.[109]

Increased ROS production at an injured site has deleterious effects such as cellular senescence, fibrotic scarring, and inflammation. The ROS-scavenging activity of ceria NPs can restrict the damage caused by oxidative stress. Immobilizing ultra-small ceria nanocrystals onto the surface of uniform MSNs yields ROS-scavenging nanocomposites that exhibit strong tissue adhesion and accelerate the wound healing (**Figure 1.13**).[110] Polymeric adhesives composited with upconverting NPs can promote the closure of wounds inside the body when stimulated by tissue-penetrating NIR light. A poly(allylamine)-modified upconverting NP/hyaluronate−rose bengal conjugate complex was developed for photochemical bonding to deep tissue in response to NIR illumination (**Figure 1.14**).[111] The triggered-adhesion technology can be applied to the development of more sophisticated minimally invasive procedures.

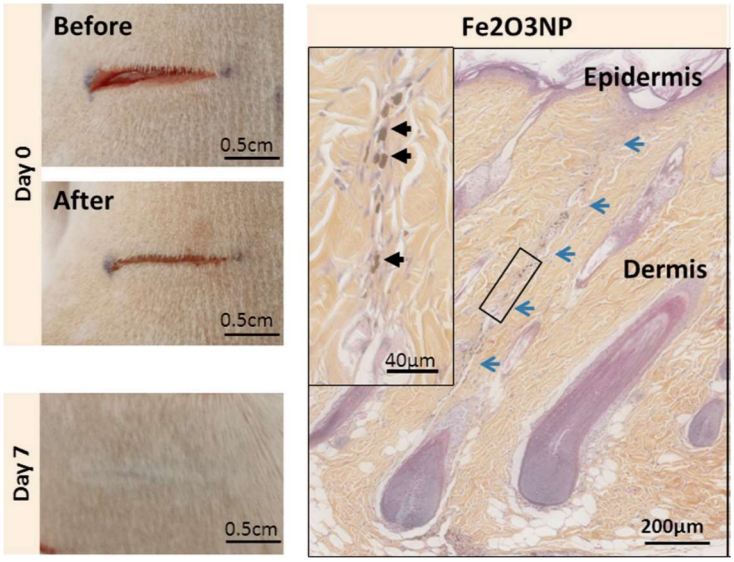

Figure 1.12. Skin wound closure with iron oxide NP solution. At day 7 post-injury, histological sections stained with hematoxylin-phloxin-saffron showed signs of injury (thin line indicated by blue arrows). (Inset) Magnification of this area revealed a normal repair process and some particle aggregates along the closing wound.[54]

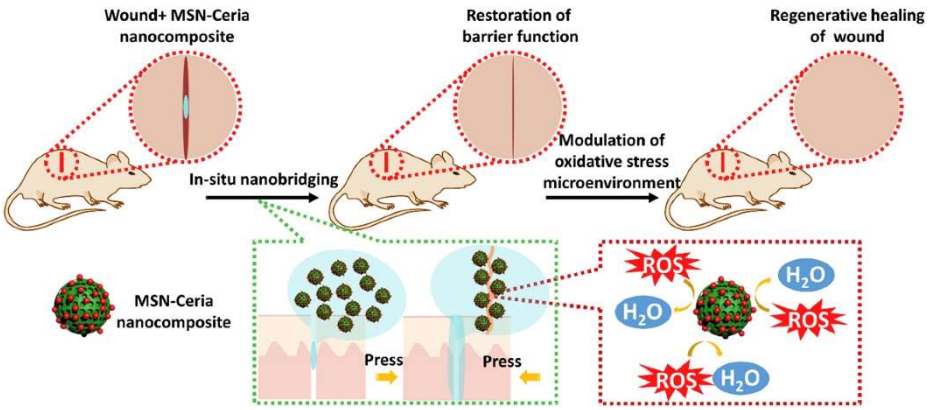

Figure 1.13. Schematic illustration of rapid cutaneous wound repair and tissue regeneration using MSN-ceria NPs as a ROS-scavenging tissue adhesive. At the initial stage, the ROS-scavenging tissue adhesive brings the edges of the wound together, restoring the tissue barrier function. Next, the adhesive alleviates oxidative stress at the injury site, providing a microenvironment suitable for tissue regeneration.[110]

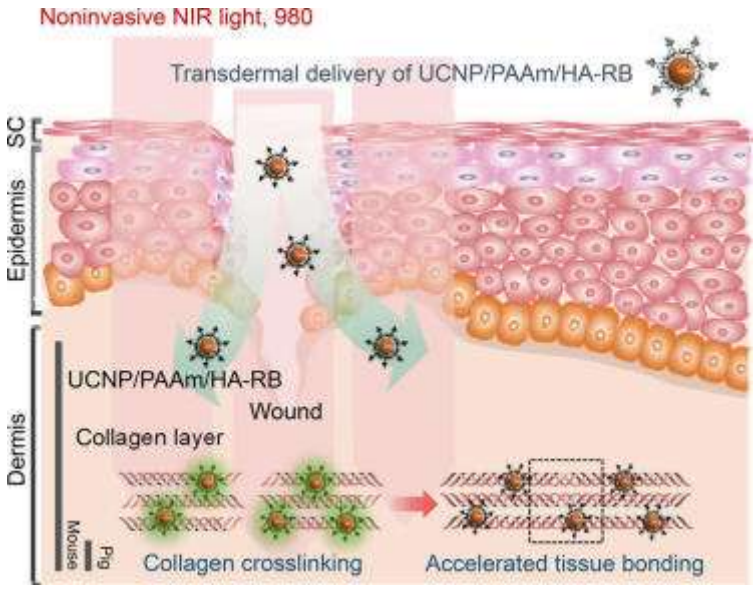

Figure 1.14. Schematic illustration of photochemical tissue bonding of incised collagen matrix by NIR light illumination. The polyallylamine (PAAm)-modified upconversion NP/hyaluronate−rose bengal (UCNP/PAAm/HA-RB) conjugate complex was delivered to the dermis by transdermal incision.[111]

1.3.6 Combination of NPs and endoscopic system

Endoscopic imaging is an invaluable diagnostic tool providing minimally invasive access to deep tissues inside the body. However, conventional white-light endoscopy provides only structural information. Various endoscopes have been developed for tumor detection and treatment. Combining the endoscope system and NPs allows early detection of lesions and enhances the efficacy of NP-based therapy. A non-contact, fiber optic-based Raman spectroscopy device has been constructed and shows unsurpassed sensitivity and multiplexing capabilities, detecting 326-fM concentrations of SERS NPs and unmixing 10 variations of colocalized SERS NPs (**Figures 1.15**).[112] A multifunctional endoscope-based system integrated with transparent bioelectronics has been combined with theranostic NPs to enable fluorescence-based mapping, radio frequency ablation, and localized photo/chemotherapy.[113]

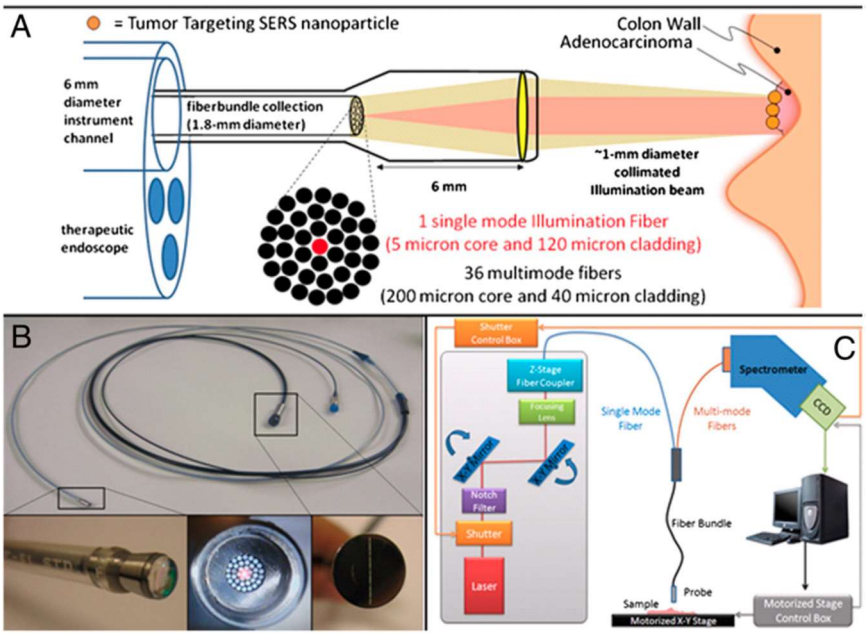

Figure 1.15. Raman endoscope design and setup with SERS NPs. (A) Schematic of Raman endoscope. (B) Photographs depicting the fabricated Raman endoscope used for clinical studies. (Lower) Enlarged digital photograph of the endoscope head (left); magnified view of the fiber bundle (center); and magnified view of the back end of the device (right). (C) Schematic illustration of the entire device setup.[112]

1.4 Dissertation overview

Minimally invasive procedures require appropriate medical imaging modalities and materials. Improvement of minimally invasive procedures is propelled by the development of NPs for imaging, tissue adhesives and therapeutic agents. The efficiency of labeling cells with NP probes is increased by the strong adhesive capacity of NPs to cells. This dissertation focuses on the development of techniques for enhancing NP adhesion to cells and tissue, which is especially useful in the context of minimally invasive procedures.

By coating thin silica layers on tantalum oxide NPs, I developed a biocompatible NP-based tissue adhesive with a high contrast effect for intraoperative imaging. An efficient and stable labeling method was developed for cell tracking by coating NPs on cells using thiol groups on the cell surface.

Next chapter of this thesis (Chapter 2) describes the synthesis of tantalum oxide/silica core/shell NPs (TSNs) that exhibit comparable tissue adhesive properties to those of clinical adhesives being used in minimally invasive procedures. Silica coating and removal of excess surfactants increased the adhesion strength of TSNs. These NPs also

provided a strong contrast effect in real-time imaging modalities including X-ray fluoroscopy, CT, ultrasonography, and fluorescence imaging. Furthermore, TSNs were less cytotoxic and caused less inflammation than the cyanoacrylate adhesives. The excellent biocompatibility, immediate hemostatic and strong contrast effects of TSNs as a tissue adhesive and an injectable fiducial marker were demonstrated in a real-time image-guided procedure.

Chapter 3 presents a general method of NP conjugation to the cell surface. Active thiol groups were introduced through mild reduction of disulfide bonds of proteins on the cell surface. MSNs were successfully attached to the cell surface via these active thiol groups. To conjugate NPs with active thiol moieties, the MSN surface was modified with a maleimide moiety. This conjugation method is more rapid than genetic labeling or cellular uptake of NPs. Being stable in a complex biological environment, the attached NPs allowed the visualization of cell morphology with fluorescence signals by intra-vital microscopic imaging. MSNs loaded with the immunosuppressant dexamethasone were attached to the cell surface and efficiently delivered the drug, enhancing cellular activities and overcoming of immune rejection in mice. Thus, the surface modification of NPs for adhesion to and labeling

of tissues can enhance the efficacy of minimally invasive procedures.

1.5 References

[1] T. L. Doane, C. Burda, *Chem. Soc. Rev.* **2012**, *41*, 2885.

[2] M. V. Kovalenko, L. Manna, A. Cabot, Z. Hens, D. V. Talapin, C. R. Kagan, V. I. Klimov, A. L. Rogach, P. Reiss, D. J. Milliron, P. Guyot-Sionnnest, G. Konstantatos, W. J. Parak, T. Hyeon, B. A. Korgel, C. B. Murray, W. Heiss, *ACS Nano* **2015**, *9*, 1012.

[3] D. Peer, J. M. Karp, S. Hong, O. C. FaroKhzad, R. Margalit, R. Langer, *Nat. Nanotechnol.* **2007**, *2*, 751.

[4] Z. X. Li, J. C. Barnes, A. Bosoy, J. F. Stoddart, J. I. Zink, *Chem. Soc. Rev.* **2012**, *41*, 2590.

[5] E. Boisselier, D. Astruc, *Chem. Soc. Rev.* **2009**, *38*, 1759.

[6] X. H. Gao, Y. Y. Cui, R. M. Levenson, L. W. K. Chung, S. M. Nie, *Nat. Biotechnol.* **2004**, *22*, 969.

[7] F. Wang, X. G. Liu, *Chem. Soc. Rev.* **2009**, *38*, 976.

[8] Y. Q. Wang, B. Yan, L. X. Chen, *Chem. Rev.* **2013**, *113*, 1391.

[9] J. Zhou, Z. Liu, F. Y. Li, *Chem. Soc. Rev.* **2012**, *41*, 1323.

[10] C. Q. Ding, A. W. Zhu, Y. Tian, *Acc. Chem. Res.* **2014**, *47*, 20.

[11] P. P. Yang, S. L. Gai, J. Lin, *Chem. Soc. Rev.* **2012**, *41*, 3679.

[12] M. Liong, J. Lu, M. Kovochich, T. Xia, S. G. Ruehm, A. E. Nel, F. Tamanoi, J. I. Zink, *ACS Nano* **2008**, *2*, 889.

[13] J. H. Gao, H. W. Gu, B. Xu, *Acc. Chem. Res.* **2009**, *42*, 1097.

[14] R. Hao, R. J. Xing, Z. C. Xu, Y. L. Hou, S. Gao, S. H. Sun, *Adv. Mater.* **2010**, *22*, 2729.

[15] X. W. Lou, L. A. Archer, Z. C. Yang, *Adv. Mater.* **2008**, *20*, 3987.

[16] C. K. Kim, T. Kim, I. Y. Choi, M. Soh, D. Kim, Y. J. Kim, H. Jang, H. S. Yang, J. Y. Kim, H. K. Park, S. P. Park, S. Park, T. Yu, B. W. Yoon, S. H. Lee, T. Hyeon, *Angew. Chem. Int. Ed.* **2012**, *51*, 11039.

[17] L. B. Zhang, L. Laug, W. Munchgesang, E. Pippel, U. Gosele, M. Brandsch, M. Knez, *Nano Lett.* **2010**, *10*, 219.

[18] F. Pagliari, C. Mandoli, G. Forte, E. Magnani, S. Pagliari, G. Nardone, S. Licoccia, M. Minieri, P. Di Nardo, E. Traversa, *ACS Nano* **2012**, *6*, 3767.

[19] J. Rauch, W. Kolch, S. Laurent, M. Mahmoudi, *Chem. Rev.* **2013**, *113*, 3391.

[20] E. Terreno, F. Uggeri, S. Aime, *J. Control. Release* **2012**, *161*, 328.

[21] E. Phillips, O. Penate-Medina, P. B. Zanzonico, R. D. Carvajal, P. Mohan, Y. P. Ye, J. Humm, M. Gonen, H. Kalaigian, H. Schoder, H. W. Strauss, S. M. Larson, U. Wiesner, M. S. Bradbury, *Sci.*

Transl. Med. **2014**, *6*.

[22] M. F. Kircher, A. de la Zerda, J. V. Jokerst, C. L. Zavaleta, P. J. Kempen, E. Mittra, K. Pitter, R. Huang, C. Campos, F. Habte, R. Sinclair, C. W. Brennan, I. K. Mellinghoff, E. C. Holland, S. S. Gambhir, *Nat. Med.* **2012**, *18*, 829.

[23] A. Verma, F. Stellacci, *Small* **2010**, *6*, 12.

[24] I. Lynch, K. A. Dawson, *Nano Today* **2008**, *3*, 40.

[25] Q. Mu, G. Jiang, L. Chen, H. Zhou, D. Fourches, A. Tropsha, B. Yan, *Chem. Rev.* **2014**, *114*, 7740.

[26] B. Pelaz, P. del Pino, P. Maffre, R. Hartmann, M. Gallego, S. Rivera-Fernandez, J. M. de la Fuente, G. U. Nienhaus, W. J. Parak, *ACS Nano* **2015**, *9*, 6996.

[27] S. Rose, A. Prevoteau, P. Elzière, D. Hourdet, A. Marcellan, L. Leibler, *Nature* **2013**, *505*, 382.

[28] A. Baldan, *Int. J. Adhes. Adhes.* **2012**, *38*, 95.

[29] K. Kendall, *Molecular adhesion and its applications: the sticky universe*, Springer Science & Business Media, **2007**.

[30] M. S. Lord, M. Foss, F. Besenbacher, *Nano Today* **2010**, *5*, 66.

[31] W. Jiang, B. Y. S. Kim, J. T. Rutka, W. C. W. Chan, *Nat. Nanotechnol.* **2008**, *3*, 145.

[32] C. Wilhelm, F. Gazeau, J. Roger, J. N. Pons, J. C. Bacri, *Langmuir* **2002**, *18*, 8148.

[33] B. Dubertret, P. Skourides, D. J. Norris, V. Noireaux, A. H. Brivanlou, A. Libchaber, *Science* **2002**, *298*, 1759.

[34] I. L. Medintz, H. T. Uyeda, E. R. Goldman, H. Mattoussi, *Nat. Mater.* **2005**, *4*, 435.

[35] J. Xie, G. Liu, H. S. Eden, H. Ai, X. Y. Chen, *Acc. Chem. Res.* **2011**, *44*, 883.

[36] R. P. Bagwe, L. R. Hilliard, W. H. Tan, *Langmuir* **2006**, *22*, 4357.

[37] G. Storm, S. O. Belliot, T. Daemen, D. D. Lasic, *Adv. Drug Deliv. Rev.* **1995**, *17*, 31.

[38] Y. Zhang, N. Kohler, M. Q. Zhang, *Biomaterials* **2002**, *23*, 1553.

[39] S. Mornet, S. Vasseur, F. Grasset, E. Duguet, *J. Mater. Chem.* **2004**, *14*, 2161.

[40] J. Perez-Juste, I. Pastoriza-Santos, L. M. Liz-Marzan, P. Mulvaney, *Coord. Chem. Rev.* **2005**, *249*, 1870.

[41] G. Su, H. Zhou, Q. Mu, Y. Zhang, L. Li, P. Jiao, G. Jiang, B. Yan, *J. Phys. Chem. C* **2012**, *116*, 4993.

[42] E. C. Cho, J. Xie, P. A. Wurm, Y. Xia, *Nano Lett.* **2009**, *9*, 1080.

[43] M. S. Ehrenberg, A. E. Friedman, J. N. Finkelstein, G.

Oberdörster, J. L. McGrath, *Biomaterials* **2009**, *30*, 603.

[44] J. K. Vasir, V. Labhasetwar, *Biomaterials* **2008**, *29*, 4244.

[45] J. Lin, H. Zhang, Z. Chen, Y. Zheng, *ACS Nano* **2010**, *4*, 5421.

[46] A. Lesniak, A. Salvati, M. J. Santos-Martinez, M. W. Radomski, K. A. Dawson, C. Åberg, *J. Am. Chem. Soc.* **2013**, *135*, 1438.

[47] S. Dante, A. Petrelli, E. M. Petrini, R. Marotta, A. Maccione, A. Alabastri, A. Quarta, F. De Donato, T. Ravasenga, A. Sathya, R. Cingolani, R. Proietti Zaccaria, L. Berdondini, A. Barberis, T. Pellegrino, *ACS Nano* **2017**, *11*, 6630.

[48] J. D. Byrne, T. Betancourt, L. Brannon-Peppas, *Adv. Drug Deliv. Rev.* **2008**, *60*, 1615.

[49] A. Salvati, A. S. Pitek, M. P. Monopoli, K. Prapainop, F. B. Bombelli, D. R. Hristov, P. M. Kelly, C. Aberg, E. Mahon, K. A. Dawson, *Nat. Nanotechnol.* **2013**, *8*, 137.

[50] M. T. Stephan, J. J. Moon, S. H. Um, A. Bershteyn, D. J. Irvine, *Nat. Med.* **2010**, *16*, 1035.

[51] D. S. Kommireddy, S. M. Sriram, Y. M. Lvov, D. K. Mills, *Biomaterials* **2006**, *27*, 4296.

[52] B. Brunel, G. Beaune, U. Nagarajan, S. Dufour, F. Brochard-Wyart, F. M. Winnik, *Soft Matter* **2016**, *12*, 7902.

[53] P. Thoniyot, M. J. Tan, A. A. Karim, D. J. Young, X. J. Loh, *Adv. Sci.* **2015**, *2*, 1400010.

[54] A. Meddahi-Pellé , A. Legrand, A. Marcellan , L. Louedec, D. Letourneur, L. Leibler, *Angew. Chem. Int. Ed.* **2014**, *53*, 6369.

[55] J.-H. Kim, H. Kim, Y. Choi, D. S. Lee, J. Kim, G.-R. Yi, *ACS Applied Materials & Interfaces* **2017**, *9*, 31469.

[56] H. Nelson, D. Sargent, H. S. Wieand, J. Fleshman, M. Anvari, S. J. Stryker, R. W. Beart, M. Hellinger, R. Flanagan, W. Peters, D. Ota, M. Hellinger, S. Clinical Outcomes Surg Therapy, *N. Engl. J. Med.* **2004**, *350*, 2050.

[57] K. Cleary, T. M. Peters, *Annu. Rev. Biomed. Eng.* **2010**, *12*, 119.

[58] T. M. Wah, *Clin. Radiol.* **2017**, *72*, 636.

[59] P. Agostinis, K. Berg, K. A. Cengel, T. H. Foster, A. W. Girotti, S. O. Gollnick, S. M. Hahn, M. R. Hamblin, A. Juzeniene, D. Kessel, M. Korbelik, J. Moan, P. Mroz, D. Nowis, J. Piette, B. C. Wilson, J. Golab, *CA Cancer J. Clin.* **2011**, *61*, 250.

[60] A. Juarranz, P. Jaen, F. Sanz-Rodriguez, J. Cuevas, S. Gonzalez, *Clin. Transl. Oncol.* **2008**, *10*, 148.

[61] C. R. Hill, G. R. terHaar, *Br. J. Radiol.* **1995**, *68*, 1296.

[62] A. Trounson, C. McDonald, *Cell Stem Cell*, *17*, 11.

[63] A. Trounson, N. D. DeWitt, *Nat. Rev. Mol. Cell Biol.* **2016**, *17*, 194.

[64] V. F. M. Segers, R. T. Lee, *Nature* **2008**, *451*, 937.

[65] R. Cancedda, B. Dozin, P. Giannoni, R. Quarto, *Matrix Biol.* **2003**, *22*, 81.

[66] R. L. Galloway, *Annu. Rev. Biomed. Eng.* **2001**, *3*, 83.

[67] A. P. Duarte, J. F. Coelho, J. C. Bordado, M. T. Cidade, M. H. Gil, *Prog. Polym. Sci.* **2012**, *37*, 1031.

[68] E. D. O'Cearbhaill, K. S. Ng, J. M. Karp, *Mayo Clin. Proc.* **2014**, *89*, 259.

[69] B. R. Smith, S. S. Gambhir, *Chem. Rev.* **2017**, *117*, 901.

[70] X. Wang, H. Chen, Y. Zheng, M. Ma, Y. Chen, K. Zhang, D. Zeng, J. Shi, *Biomaterials* **2013**, *34*, 2057.

[71] N. Lee, S. H. Choi, T. Hyeon, *Adv. Mater.* **2013**, *25*, 2641.

[72] Y. I. Park, K. T. Lee, Y. D. Suh, T. Hyeon, *Chem. Soc. Rev.* **2015**, *44*, 1302.

[73] M. H. Oh, N. Lee, H. Kim, S. P. Park, Y. Piao, J. Lee, S. W. Jun, W. K. Moon, S. H. Choi, T. Hyeon, *J. Am. Chem. Soc.* **2011**, *133*, 5508.

[74] N. Lee, D. Yoo, D. Ling, M. H. Cho, T. Hyeon, J. Cheon, *Chem.*

Rev. **2015**, *115*, 10637.

[75] A. S. Thakor, J. V. Jokerst, P. Ghanouni, J. L. Campbell, E. Mittra, S. S. Gambhir, *J. Nucl. Med.* **2016**, *57*, 1833.

[76] T. Schroeder, *Nature* **2008**, *453*, 345.

[77] M. F. Kircher, S. S. Gambhir, J. Grimm, *Nat. Rev. Clin. Oncol.* **2011**, *8*, 677.

[78] L. W. van Laake, R. Passier, J. Monshouwer-Kloots, M. G. Nederhoff, D. Ward-van Oostwaard, L. J. Field, C. J. van Echteld, P. A. Doevendans, C. L. Mummery, *Nat. Protoc.* **2007**, *2*, 2551.

[79] H. E. Daldrup-Link, C. Chan, O. Lenkov, S. Taghavigarmestani, T. Nazekati, H. Nejadnik, F. Chapelin, A. Khurana, X. Tong, F. Yang, L. Pisani, M. Longaker, S. S. Gambhir, *Radiology* **2017**, *284*, 495.

[80] T. Kim, E. Momin, J. Choi, K. Yuan, H. Zaidi, J. Kim, M. Park, N. Lee, M. T. McMahon, A. Quinones-Hinojosa, J. W. M. Bulte, T. Hyeon, A. A. Gilad, *J. Am. Chem. Soc.* **2011**, *133*, 2955.

[81] M. Mahmoudi, H. Hosseinkhani, M. Hosseinkhani, S. Boutry, A. Simchi, W. S. Journeay, K. Subramani, S. Laurent, *Chem. Rev.* **2011**, *111*, 253.

[82] M. Lewin, N. Carlesso, C.-H. Tung, X.-W. Tang, D. Cory, D. T.

Scadden, R. Weissleder, *Nat. Biotechnol.* **2000**, *18*, 410.

[83] N. Lee, H. Kim, S. H. Choi, M. Park, D. Kim, H.-C. Kim, Y. Choi, S. Lin, B. H. Kim, H. S. Jung, H. Kim, K. S. Park, W. K. Moon, T. Hyeon, *Proc. Natl. Acad. Sci. U.S.A.* **2011**, *108*, 2662.

[84] J. V. Jokerst, M. Thangaraj, P. J. Kempen, R. Sinclair, S. S. Gambhir, *ACS Nano* **2012**, *6*, 5920.

[85] T. Kim, N. Lee, D. R. Arifin, I. Shats, M. Janowski, P. Walczak, T. Hyeon, J. W. M. Bulte, *Adv. Funct. Mater.* **2017**, *27*, 1604213.

[86] T. Kim, J. E. Lemaster, F. Chen, J. Li, J. V. Jokerst, *ACS Nano* **2017**, *11*, 9022.

[87] R. L. Manthe, S. P. Foy, N. Krishnamurthy, B. Sharma, V. Labhasetwar, *Mol. Pharm.* **2010**, *7*, 1880.

[88] J. E. Kennedy, *Nat. Rev. Cancer* **2005**, *5*, 321.

[89] S. A. Curley, F. Izzo, L. M. Ellis, J. N. Vauthey, P. Vallone, *Ann. Surg.* **2000**, *232*, 381.

[90] K. Yang, G. Yang, L. Chen, L. Cheng, L. Wang, C. Ge, Z. Liu, *Biomaterials* **2015**, *38*, 1.

[91] H. Xing, X. Zheng, Q. Ren, W. Bu, W. Ge, Q. Xiao, S. Zhang, C. Wei, H. Qu, Z. Wang, Y. Hua, L. Zhou, W. Peng, K. Zhao, J. Shi, *Sci. Rep.* **2013**, *3*, 1751.

[92] L. R. Hirsch, R. J. Stafford, J. A. Bankson, S. R. Sershen, B. Rivera, R. E. Price, J. D. Hazle, N. J. Halas, J. L. West, *Proc. Natl. Acad. Sci. U.S.A.* **2003**, *100*, 13549.

[93] L. C. Kennedy, L. R. Bickford, N. A. Lewinski, A. J. Coughlin, Y. Hu, E. S. Day, J. L. West, R. A. Drezek, *Small* **2011**, *7*, 169.

[94] D. Jaque, L. Martinez Maestro, B. del Rosal, P. Haro-Gonzalez, A. Benayas, J. L. Plaza, E. Martin Rodriguez, J. Garcia Sole, *Nanoscale* **2014**, *6*, 9494.

[95] D. C. Niu, X. Wang, Y. S. Li, Y. Y. Zheng, F. Q. Li, H. R. Chen, J. L. Gu, W. R. Zhao, J. L. Shi, *Adv. Mater.* **2013**, *25*, 2686.

[96] H. T. Ke, J. R. Wang, S. Tong, Y. S. Jin, S. M. Wang, E. Z. Qu, G. Bao, Z. F. Dai, *Theranostics* **2014**, *4*, 12.

[97] X. Wang, H. R. Chen, Y. Y. Zheng, M. Ma, Y. Chen, K. Zhang, D. P. Zeng, J. L. Shi, *Biomaterials* **2013**, *34*, 2057.

[98] X. Wang, H. R. Chen, Y. Chen, M. Ma, K. Zhang, F. Q. Li, Y. Y. Zheng, D. P. Zeng, Q. Wang, J. L. Shi, *Adv. Mater.* **2012**, *24*, 785.

[99] J.-H. Lee, J.-t. Jang, J.-s. Choi, S. H. Moon, S.-h. Noh, J.-w. Kim, J.-G. Kim, I.-S. Kim, K. I. Park, J. Cheon, *Nat. Nanotechnol.* **2011**, *6*, 418.

[100] D. K. Chatterjee, L. S. Fong, Y. Zhang, *Adv. Drug Deliv. Rev.*

2008, *60*, 1627.

[101] S. S. Lucky, K. C. Soo, Y. Zhang, *Chem. Rev.* **2015**, *115*, 1990.

[102] A. Sazgarnia, A. Shanei, N. T. Meibodi, H. Eshghi, H. Nassirli, *J. Ultrasound Med.* **2011**, *30*, 1321.

[103] D. G. You, V. G. Deepagan, W. Um, S. Jeon, S. Son, H. Chang, H. I. Yoon, Y. W. Cho, M. Swierczewska, S. Lee, M. G. Pomper, I. C. Kwon, K. Kim, J. H. Park, *Sci. Rep.* **2016**, *6*.

[104] S. Yamaguchi, H. Kobayashi, T. Narita, K. Kanehira, S. Sonezaki, N. Kudo, Y. Kubota, S. Terasaka, K. Houkin, *Ultrason. Sonochem.* **2011**, *18*, 1197.

[105] S. Goel, D. Ni, W. Cai, *ACS Nano* **2017**, *11*, 5233.

[106] X. Zou, M. Yao, L. Ma, M. Hossu, X. Han, P. Juzenas, W. Chen, *Nanomedicine (Lond.)* **2014**, *9*, 2339.

[107] N. Annabi, A. Tamayol, S. R. Shin, A. M. Ghaemmaghami, N. A. Peppas, A. Khademhosseini, *Nano Today* **2014**, *9*, 574.

[108] M. T. Matter, F. Starsich, M. Galli, M. Hilber, A. A. Schlegel, S. Bertazzo, S. E. Pratsinis, I. K. Herrmann, *Nanoscale* **2017**, *9*, 8418.

[109] Y. Gao, Y. Han, M. Cui, H. L. Tey, L. Wang, C. Xu, *J. Mater. Chem. B* **2017**, *5*, 4535.

[110] H. Wu, F. Li, S. Wang, J. Lu, J. Li, Y. Du, X. Sun, X. Chen, J. Gao, D. Ling, *Biomaterials* **2018**, *151*, 66.

[111] S. Han, B. W. Hwang, E. Y. Jeon, D. Jung, G. H. Lee, D. H. Keum, K. S. Kim, S. H. Yun, H. J. Cha, S. K. Hahn, *ACS Nano* **2017**, *11*, 9979.

[112] C. L. Zavaleta, E. Garai, J. T. C. Liu, S. Sensarn, M. J. Mandella, D. Van de Sompel, S. Friedland, J. Van Dam, C. H. Contag, S. S. Gambhir, *Proc. Natl. Acad. Sci. U.S.A.* **2013**, *110*, E2288.

[113] H. Lee, Y. Lee, C. Song, H. R. Cho, R. Ghaffari, T. K. Choi, K. H. Kim, Y. B. Lee, D. Ling, H. Lee, S. J. Yu, S. H. Choi, T. Hyeon, D.-H. Kim, *Nat. Commun.* **2015**, *6*, 10059.

Chapter 2. Multifunctional nanoparticles as a tissue adhesive and an injectable marker for image-guided procedures

2.1 Introduction

Tissue adhesives have various advantages over sutures and staples, including a simpler implementation procedure, more immediate sealing, less pain to patients, lower infection rates, and less trauma on operated tissues.[1-4] Hence, their clinical demands have grown significantly, and consequently, a number of tissue adhesives based on proteins and synthetic polymers including fibrin, gelatin, polyurethanes, and polyethylene glycol have been developed to accommodate various surgical situations.[5-10] The convenience of tissue adhesives is particularly noticeable in minimally invasive procedures and image-guided surgeries because they are very effective for treating a confined region of interest that is inaccessible with other wound closure methods, which can greatly reduce postoperative complications. Since minimally invasive procedures are typically guided by real-time imaging modalities,

such as X-ray fluoroscopy, computed tomography (CT), ultrasonography, and fluorescence imaging, it is useful that the applied tissue adhesives are visible with such imaging modalities for accurate and safe applications.[11-13] Moreover, radiotherapy or minimally invasive procedures to soft organs can also be aided by the tissue adhesives with imaging contrast effects for efficient recognition and follow-up of the target areas along the physiological movement of the organ.[14,15]

Nanoparticles have been incorporated with tissue adhesives or hydrogels to enhance their mechanical properties, adhesive strength, and electrical conductivity and to provide unique functions such as antibacterial effects.[4,16-18] Recently, it was reported that the nanoparticle solution itself can act as an adhesive for hydrogels and biological tissues.[19] Owing to its large surface area and the high adsorption energy between biological tissues and the nanoparticle surface, the adhesive property of nanoparticles is sufficient for various applications, such as hemostasis, wound closure, and scaffold-attachments.[20] On the other hand, nanoparticles have also been employed as biomedical imaging probes owing to their unique physical properties and capability of conjugating functional moieties via surface modification.[21-29] They have been used with various molecular imaging modalities for the

sensitive diagnosis of lesions.[30-37] Based on these two different medical applications of nanoparticles, they may be a promising candidate for multimodal image-guided procedures.[38-40]

Herein, we design core-shell structured tantalum oxide-silica nanoparticles as tissue adhesives in image-guided surgery (**Figure 2.1a**). We employ silica (SiO_2) as the shell material to endow the nanoparticles with a tissue adhesive property, because its surface offers high adhesive strength to hydrogels or tissues.[19] Radiopaque tantalum oxide (TaO_x) is selected as the core material to provide contrast enhancement on X-ray fluoroscopy and CT. TaO_x nanoparticles combined with various organic and inorganic moieties have been applied to multimodal imaging and/or theranostics.[41-48] In the current study, the high density of the TaO_x core and the facile modification of the SiO_2 surface allow for ultrasound (US) and fluorescence imaging. As designed, the TaO_x/SiO_2 core/shell nanoparticle (TSN) glue is clearly visualized by real-time imaging modalities, which facilitates image-guided, less-invasive procedures using this material, and exhibits adhesive property similar to that of a mixture of cyanoacrylate and Lipiodol used in clinical practice. Cyanoacrylate adhesive including Histoacryl (B. Braun, Melsungen, Germany), a frequently used tissue adhesive in human, has to be mixed

with radiopaque, iodized oil (Lipiodol; Andre Guerbe, Aulnay-sous-Bios, France) – the most commonly used form is a 1:3 (v/v) mixture of cyanoacrylate and Lipiodol (CA-Lp) – to be administered under the guidance of fluoroscopy. In the present study, tissue adhesive properties of the TSN is comparable with those of CA-Lp (**Figure 2.1b**). Moreover, TSNs are highly biocompatible, as evidenced by dramatically reduced cytotoxicity and inflammation reaction compared to the clinically used CA-Lp. We also demonstrate that TSNs can work as tissue adhesives with the assistance of multimodal imaging modalities in a liver puncture model to stop internal bleeding. Because of their adhesive property and multimodal imaging capability, TSNs are used as an injectable immobilized anatomical marker to aid image-guided surgery.

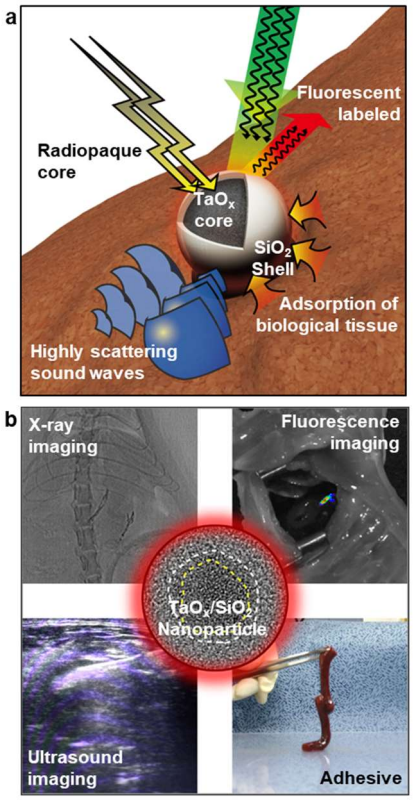

Figure 2.1. Tantalum oxide/silica core/shell nanoparticles (TSNs) as an adhesive for multimodal image-guided procedures. a, Schematic illustration of a multifunctional TSN with a radiopaque core for X-ray imaging, conjugated fluorescent dye for fluorescent imaging, a dense core material with a high sound-scattering effect for ultrasound imaging, and a silica surface for adhesive property. b, Representative images demonstrating multifunctionality of TSNs.

2.2 Experimental Section

2.2.1 Preparation of TSNs

The TSNs were synthesized by the aqueous sol-gel reaction confined in reverse-micelles based on the previous report.[41] Igepal CO-520 (46 g, Sigma-Aldrich), ethanol (5 ml, Samchun, 99.9%), aqueous NaOH solution (5 ml, 150 mM, Samchun) were mixed with cyclohexane (800 ml, Samchun, 99.5%) to form a microemulsion under vigorous stirring. To the resulting transparent solution, tantalum ethoxide (1 ml, 3.85 mmol, Strem, 99.8%) was injected at room temperature, and stirred for 30 min. Subsequently, 28% ammonium hydroxide solution (5 ml, Samchun) and tetraethyl orthosilicate (TEOS, 1 ml, 4.47 mmol, Acros, 98%) were successively added. The mixture was stirred at room temperature for 12 h. After the reaction, the solvents were removed by evaporation at 60 oC, until the solution became white and viscous. The synthesized nanoparticles were separated by centrifugation, and dispersed in ethanol. In order to remove the adsorbed surfactants, 5 ml of hydrochloric acid (Daejung, 35%) was added, and the nanoparticles were centrifuged and subsequently washed with ethanol twice. The solution was neutralized

by washing twice each with 20 ml of phosphate buffer (pH = 8.0, 0.1 M) and distilled water. Finally, the solution was concentrated up to 40 wt% and loaded into a 1-ml syringe.

2.2.2 Rhodamine conjugation and surface modification of the TSNs

The conjugation of TSNs was performed by mixing acid-treated nanoparticles with dye-conjugated silane. Tetramethylrhodamine isothiocyanate (0.44 mg, Sigma-Aldrich, mixed isomers) and (3-aminopropyl)trimethoxysilane (0.18 mg, Sigma-Aldrich, 97%) were dissolved in 0.5 ml of dimethylformamide (Samchun, 99.5%), and the solution was shaken gently for 30 min. The resulting dye solution was added to the nanoparticle solution dispersed in the phosphate buffer (pH = 8.0), and kept being shaken over 8 hours. The unreacted dye molecules were removed by several centrifugations, and the resulting nanoparticles were dispersed in distilled water.

2.2.3 Preparation of CA-Lp and SiO_2 NPs

CA-Lp was prepared by mixing Histoacryl® (B.Braun Surgical, Germany) and Lipiodol Ultra-Fluid® (Guerbet, France) with a volumetric ratio of 1:3, to have a comparable fluoroscope contrast effect, with the iodine concentration of 360 mgI ml-1. CA-Lp was prepared right before the experiments to avoid the loss of the adhesive properties. To make a comparison with the reported nano-bridging SiO2 NPs, Ludox® TM-50 (50 wt% of silica) was purchased from Sigma-Aldrich and used without any treatment.[19,20]

2.2.4 Characterization of TSNs and SiO_2 NPs

TSNs and SiO_2 NPs were analyzed using a transmission electron microscope (TEM, 200 kV, JEOL-2100, JEOL Ltd., Japan). Fourier transform infrared (FT-IR) spectra were obtained with a JASCO FT/IR-200 (Jasco Inc., Japan). Hydrodynamic diameters and ζ-potentials of the nanoparticles dispersed in water were analyzed with a size analyzer (Nanozs, Malvern, Germany). The absorption and emission spectra of the rhodamine-conjugated nanoparticles and free dye were measured with a SpectroV-550 (Jasco inc., Japan) and a FP-5500 (Jasco Inc.,

Japan). Nitrogen adsorption/desorption isotherm was measured by a 3FLEX surface characterization analyzer (Micromeritics, USA).

2.2.5 Evaluation of contrast effect

Each type of the adhesive (TSNs, SiO_2 NPs and CA-Lp) was loaded into a 2-ml tube. The contrast effect on fluoroscopy was measured with images acquired by an Allura Xper FD20 (Philips, Netherlands, at 80 kV of tube voltage). The SNR was calculated as SNR = S / N, where S is the mean attenuation of each material and N is the standard deviation of background attenuation. Dose-dependent contrast enhancement was examined by comparing the TSNs with SiO_2 NPs (Ludox® TM-50) and a contrast agent (iopamidol, Pamiray®, Dongkook pharmaceutical Co., Korea) which were prepared with the same mass concentration. The solutions containing the nanoparticles or the contrast agent was diluted sequentially and dispersed in 1 wt% agarose gel and loaded to 200 μl microtubes. Both fluoroscopy and CT were used to analyze these series of tubes, and the obtained images were evaluated with the OsiriX software (version 4.0; 32 bit; OsiriX foundation Geneva). The clinical CT scanner (Brilliance 64, Philips Medical System, USA) was operated

at 140 kVp and 150 mA. To compare the US contrast effect of the TSNs with other glues, 50 μl of each glue was injected to fresh calf liver using an 18-gauge needle while withdrawing a syringe. Afterwards, B-mode US images were obtained with an Accuvix V10 (Samsung Medison co., Ltd, Korea). The mean intensity and standard deviation of each region-of-interest were calculated with the ImageJ software (version 1.48v, NIH). To evaluate the contrast effect in serial dilution, the SiO2 NPs and TSNs were diluted using 1 wt% agarose, and 200 μl of each solution were cured in a 96-well plate. The plate was immersed in a water bath and the backscattered amplitudes were measured with the same method used in the calf specimens.

2.2.6 Adhesion strength test

Fresh calf livers were cut into several pieces of ribbon shape (45 mm × 10 mm × 4 mm each) with a scalpel and an autopsy blade. Two pieces of the calf liver ribbons were adhered by applying ~15 μl of each glue. The ribbon pieces were overlapped by 10 mm, and the overlapped portion was gently pressed by a finger for 10 seconds. To quantify the adhesive strength of the lap joints attached by the glues, lap-shear tests were

performed by using an Instron-5543 electromechanical system (Instron, USA) controlled by the Bluehill software (Ver. 3). The lab joints were placed in a 50 N load cell and the test was performed at a speed of 30 mm min-1. Each displacement-force curves were calibrated to the points after slipping, not to be influenced by weights of the lower ribbon of liver.

2.2.7 Electron microscopic imaging of liver tissue

Electron microscope samples were prepared by fixation and dehydration of the calf liver tissues attached with TSNs. The adhered tissues were fixed with 2.5% of glutaraldehyde and 2% of paraformaldehyde in 0.1 M of sodium cacodylate buffer (pH 7.4), which was then rinsed with cacodylate buffer. Additional fixation was proceeded with 1% osmium tetraoxide solution in cacodylate buffer. After washing the residual fixation reagent with distilled water three times, they were stained overnight with 2% uranyl acetate solution. The dehydration was proceeded gradually with ethanol, by incubating them for 10 min in 30%, 50%, 70%, 80%, 90% ethanol, and finally absolute ethanol three times to eliminate water in the tissues. For scanning electron microscope (SEM) sample, the tissues were dried with critical point drier (EM CPD 300,

Lieca, Austria) and coated with Pt by sputter coater (EM ACE200, Leica, Austria). For TEM samples, Spurr's resin was used in order to ultramicrotome sectioning. Further solvent exchange and infiltration of the resin were proceeded by incubating the dehydrated tissues in propylene oxide twice for 10 min, in 50% Spurr's resin with propylene oxide for 2 h, and finally in Spurr's resin overnight. The tissues were embedded in fresh Spurr's resin at 60 oC for 24 h. The embedded samples were cut with ultramicrotome (EM UC7, Leica, Germany). SEM images were obtained with JSM-6701F (JEOL Ltd., Japan) and energy dispersive X-ray spectrometer (EDS) spectra and element mapping were performed using the attached INCA Energy (Oxford Instruments Analytical Ltd., UK). TEM images were obtained with JEM1010 (JEOL Ltd. Japan).

2.2.8 Cell culture

Hela cells from Korean Cell Line Bank (KCLB) were maintained in Dulbecco's Modified Eagle's Medium (DMEM, Gibco). The medium was supplemented with 10% fetal bovine serum (FBS, Gibco BRL), 100 μg mL^{-1} streptomycin, and 100 IU penicillin (Gibco BRL). Cells were

grown as monolayer cultures in a T75-flask and sub-cultured three times in one week at 37 °C in atmosphere containing 5% CO2 and 100% relative humidity.

2.2.9 Morphological analysis

A 20-µl drop of TSNs or CA-Lp was placed on the middle of coverglass-bottom dish. A Cell suspension in a logarithmic growth phase was added to the dish. Following 24 h of cell seeding onto the dish, bright field images were taken by an inverted confocal microscope (LSM 780, Carl-Zeiss, Germany).

2.2.10 Viability assay

For the in vitro cytotoxicity assay, cells in a logarithmic growth phase were detached and plated (400 µL per well) in 24-well flat-bottom microplates at a density of 40,000 cells per well, which were then left for 24 h at 37 °C to resume exponential growth. After 24 h of recovery, the cellular media were exchanged with the media containing TSNs with various concentrations. As CA polymerizes and hardens with water

contact, it is hard to be diluted in PBS or cellular media. Alternatively, we put a drop of CA-Lp gel in the well, letting some molecules or materials be dissolved naturally and affect the cells. After the removal of the media in wells, different volume of the CA-Lp (100, 200, 400, and 800 μl) and different concentrations of TSNs were introduced to each culture well, and incubated with 1 ml of cellular media. Following 24 h exposure of the glues to the cells under the same culturing condition, cell viability was assessed by MTT (3-[4,5-dimethylthialzol-2-yl]-2,5-diphenyltetrazolium bromide, Sigma) assay. The assay was performed in quadruplicate in the following manner. The cells were incubated in media with 1 mg ml-1 of MTT solution for 2 h. Then the MTT solution was removed and the precipitated violet crystals were dissolved in 1 ml dimethylsulfoxide (DMSO). The absorbance of the solution was measured at 490 nm with microplate reader (Victor X4, Perkin-Elmer, USA).

2.2.11 Preparation of SiO_2 NPs and TaO_x NPs for hemolysis test

The 105 nm-sized SiO2 NPs were synthesized with Stober process, and 22 nm-sized SiO2 NPs were prepared with the same microemulsion

method used in preparation of TSN, except that the precursor was changed to tetramethyl orthosilicate. The 120 nm-sized TaOx NPs were synthesized by aqueous sol-gel reaction of $Ta(OEt)_5$ in 90% ethanol aqueous solution.

2.2.12 Hemolysis assay

Rabbit blood was collected freshly and stabilized with sodium-heparin. To remove plasma from the whole blood, 4 ml of whole blood was diluted with 12 ml of PBS and centrifuged at 10000 rpm for 5 min. The supernatant including plasma was removed carefully, and the cells were suspended with additional 12 ml of PBS. Red blood cells (RBC) were isolated by several washing process with 12 ml of PBS and the final solution was diluted with 40 ml of PBS. The nanoparticle solution was diluted with PBS to the various concentrations, and prepared in triplicate. To assess the hemolysis effect, 0.8 ml of the nanoparticle solution and 0.2 ml of the diluted RBC suspension were mixed to reach the final particle concentrations of 100, 200, 500, 1000 μg ml^{-1}. For negative and positive controls, PBS and distilled water were mixed with the same amount of RBC, respectively. The mixtures were incubated at room

temperature for 24 h, followed by a centrifugation at 10000 rpm for 5 min. Each 200 μl of the supernatant of the mixture were conveyed to a 96-well plate and its absorbance was measured at 490 nm with a microplate reader. The percentage of the hemolysis of RBCs was calculated by following formula: percent of hemolysis = ((sample absorbance - negative control absorbance)/(positive control absorbance - negative control absorbance))×100.

2.2.13 Degradation experiments of TSN in simulated body fluid

The simulated body fluid (SBF) was prepared as previous report.[49] Each 500 ml of SBF was prepared in polyethylene bottle TSN was immersed with concentration of 200 mg L^{-1}, and 400 mg L^{-1}. About 10 ml of the sample solutions were extracted each time with centrifugal filter unit (Amicon®, 3kDa). The concentration of free tantalum were determined using inductively coupled plasma mass spectrometry (Elan 6100, PerkinElmer) of National center for inter-university research facilities, Seoul National University.

2.2.14 Migration experiments for various fiducial markers

Five different markers such as a contrast agent (Lipiodol), adhesive mixture (CA-Lp), coil, gold rod, and TSNs were implanted or injected into calf liver and lung specimen. The calf liver and lung were prepared freshly by cutting into proper sized cuboid and put into airtight containers. Fifteen needles were attached uprightly in order to hold the specimens in the containers. Those were imaged with a CT scanner after 1, 3, 5 and 10 hours of shaking. The migration distances were measured according to the method of a previous report.[50]

2.2.15 Animal study

All procedures were approved by the Institutional Animal Care and Use Committee (IACUC) of the Clinical Research Institute of Seoul National University Hospital, and all experimental procedures were performed according to the IACUC guidelines.

2.2.16 Liver puncture model in SD rat

Ten male Sprague-Dawley (SD) rats, at the age of 12 weeks, initially weighing about 400 g, were randomly divided by two groups (i.e. five rats per group) and each group was treated by TSNs and CA-Lp. The rats were anesthetized by intramuscular injection of a mixture of zolazepam (5 mg kg-1, Zoletil®, Virbac, Carros, France) and xylazine (10 mg kg-1, Rompun®, Bayer-Schering Pharma, Berlin, Germany). To apply the glues to the rat liver and to evaluate their hemostatic effect, the left lobe of the liver of was exposed by a median abdominal incision. After creating a liver stab wound, 18-gauge in diameter (1.27 mm) and 1.5 cm in length, the needle track was closed with the TSNs or CA-Lp mixture preloaded within a syringe. 0.03 mL of the adhesives was slowly injected during the withdrawal of the needle. In order to measure the amount of bleeding, hydrophobic films (Parafilm) were put on each lower and upper side of the liver and filter paper was put right onto the wound area. After bleeding stopped, the amount of the absorbed blood was calculated by measuring the change of the weight of the filter papers.

CT and fluoroscopy images were acquired after the abdominal closure. Fluoroscopic images were obtained with exposure of X-ray at 80 kV for 3 ms. CT imaging parameters of the SD rats were as followed:

thickness, 0.6 mm; pitch, 0.648; 120 kVp, 300 mA; field of view, 127×127; gantry rotation time, 0.75 s; table speed, 16.7 mm s-1.

2.2.17 Image-guided procedure in a rabbit liver puncture model

Demonstration of image-guided procedures was conducted with a male New Zealand White rabbit weighing 3.5 kg, with the same method in SD rats, except the abdominal incision and exposure of the liver. An 18-gauge stainless steel needle was used to make an intrahepatic track under the guidance of US and fluoroscopy, and 0.05 mL of the adhesives was slowly injected during the withdrawal of the needle. During the image-guided procedure, the operation video and fluoroscopy video were recorded simultaneously. The fluoroscopic images were acquired with exposure of X-ray at 60 kV for 1 ms.

2.2.18 Percutaneous anatomical marking in rats

The rats were euthanized by the same method used in the liver puncture model. Regarding the clinical contexts where fiducial marking for subsequent image-guided surgery or radiotherapy is frequently used (i.e.

musculoskeletal tumors and lung tumors), experiments were conducted for the leg muscles and syngeneic lung tumor. The muscle and lung marking studies were conducted with two male SD rats (12-week-old, 400g) and two male F344 rats (12-week-old, 300g), respectively. Regarding the muscular injection study, 0.02 mL of TSNs was gently implanted into the thigh and calf muscles of male SD rats though a 22-gauge needle. The fiducial markers were observed on micro-CT, real-time fluoroscopy, and fluorescent imaging (IVIS 100, Perkin Elmer). During the fluoroscopic study, the TSN-implanted leg was manually flexed and extended to address whether the fiducial marker was changed in its shape and/or position. To obtain fluorescent signals from the deep muscles, the legs were skinned before fluorescent imaging. For creating a syngeneic lung cancer model, a 0.5×0.5×0.5 cm sized tumor chip (13762-MAT-B-III cell-line [CRL-1666, ATCC, Manassas, VA, USA]) was injected into the tail vein of male F344 rats. After 10 days, the rats underwent a CT study to identify lung embolization and growth of the tumor chip. A 25-gauge needle was precisely advanced to the lung tumor under CT imaging guidance, and then 0.02 mL of pre-loaded TSNs was slowly injected into the target. The markers were also observed on CT,

real-time fluoroscopy, and fluorescent imaging that obtained after thoracostomy.

2.2.19 Histological analysis

The rats were euthanized in a CO2 chamber, and then the liver was excised and fixed in 10% neutral buffered formalin (10% NBF) for one week. For hematoxylin and eosin (H&E) staining, formalin fixed tissues from each specimen were embedded into paraffin and sectioned into 4 μm thickness. Standard H&E staining was performed to evaluate morphological features of each specimen regarding inflammatory reactions and fibrosis as time passes. The pathologic slides were also analyzed with CD68 immunohistochemistry (CD68 antibody, sc-59103, Santa Cruz Biotechnology) to address macrophage recruitment after liver puncture. Afterwards, all samples were digitalized with optical magnification (×200) to conduct further analyses. The slides were carefully reviewed by an experienced pathologist who was blinded to the kinds of adhesives.

2.2.20 In vivo toxicity evaluation of TSN

To assess the in vivo toxicity of the TSNs, serum chemistry and biodistribution of the NPs were evaluated. 30 μL of the TSNs solution and CA-Lp mixture was applied to SD rats. Since we are interested in two different regions of application, rats were divided into two groups; one is for the liver and the other is for muscle. Rats were sacrificed after 3, 7, 28 and 42 days from the nanoparticle application, and the reticuloendothelial system (liver, spleen and kidney), blood, heart, muscle and lung were harvested. In the target organ (liver and muscle), two different regions within the same organ were collected. The tissues were firstly digested with nitric acid, and hydrofluoric acid was added to dissolve TSNs. Ta concentration was determined from inductively coupled plasma mass spectrometer (ICP-MS, NexION300, Perkin Elmer, USA). By collecting 2-ml blood samples from the tail vein of the SD rats, serum biochemistry was examined from the analysis for inflammation (CRP), liver function (ALP, AST, ALT), and kidney function (BUN, CREA), at 3, 7, 21, and 42 days after application of TSN to liver and muscle.

2.2.21 Statistical analysis

Data are shown as mean ± s.d, except Supplementary Figure 5b and 7b. Statistical analyses of intergroup comparisons were performed using a two-sided unpaired Student's t-test and one-way ANOVA tests were used to results having multiple groups. $P < 0.05$ was considered significant. The investigators were not blinded to group allocations during the experiments and analyses except for the histological analysis, and no randomization method was used. Sizes of sample were determined to empirically for sufficient statistical power.

2.3 Result and Discussion

2.3.1 Synthesis and characterization of TaO_x/SiO_2 core/shell NPs

TSNs were synthesized by the sol-gel reaction of tantalum(V) ethoxide in nanometer-sized microemulsion.[41] After TaOx nanoparticles were generated, the SiO2 shell was grown on the TaO_x core by sol-gel reaction of tetraethoxysilane (TEOS). Transmission electron microscopy (TEM) images show uniform nanoparticles of an overall size of 8.5 ± 0.8 nm with a SiO_2 shell thickness of 1.3 ± 0.2 nm (**Figure 2.2d**). After the nanoparticles were purified by centrifugation, they were treated with acid to remove any residual adsorbed surfactants that may interfere with the interactions between the nanoparticle surface and biological tissues, leading to the loss of the adhesive property. Removal of the surfactants was confirmed with Fourier transform infrared spectroscopy by the disappearance of peaks related to Igepal CO-520 (**Figure 2.3**). Without the SiO_2 shell, the reactive TaO_x surface causes a severe aggregation of tantalum oxide nanoparticles after the removal of surfactants (**Figure 2.2a**), generating micrometer-sized agglomerates (**Figure 2.4a**). However, the SiO_2 shell successfully protects TSNs from irreversible

agglomeration, resulting in the number-average hydrodynamic diameter of 20.4 nm (**Figure 2.4b**). It is crucial that the TSNs should be well dispersed as nanoparticle form because the adhesive property of the nanoparticles is affected by surface adsorption with biological tissue, which will be discussed below. In order to utilize TSNs for optical image-guided surgery, fluorescent TSNs were prepared by covalent attachment of tetramethylrhodamine isothiocyanate (TRITC) onto the TSN surface. Photoluminescence of the TRITC-conjugated TSNs reveals a typical peak of TRITC at 576 nm (**Figure 2.4d**).

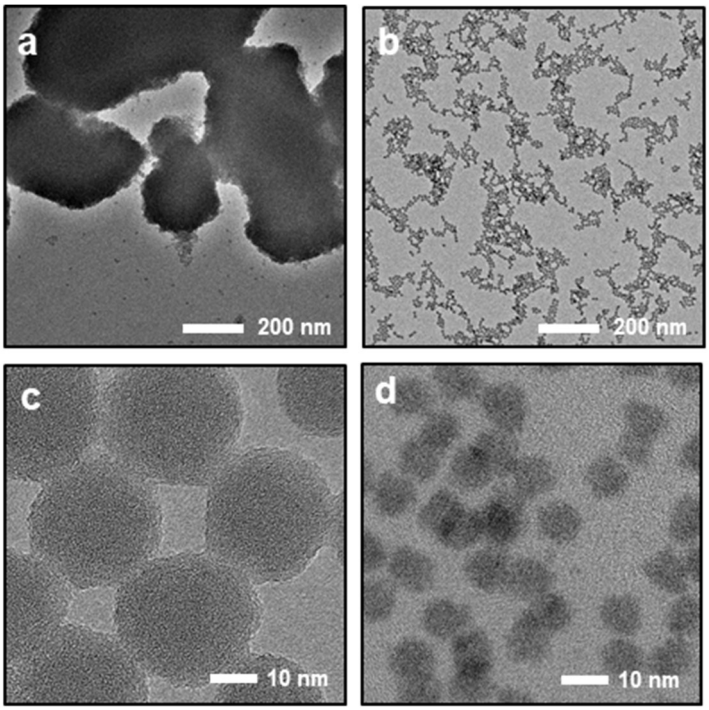

Figure 2.2. (a) TEM image of TaO_x nanoparticles without SiO_2 shell, which is agglomerated to micron-size. (b) TEM image of TSNs after the acid treatment, which are dispersed well. (c) high magnified TEM images of SiO_2 NPs. (d) high magnified TEM images of TSNs.

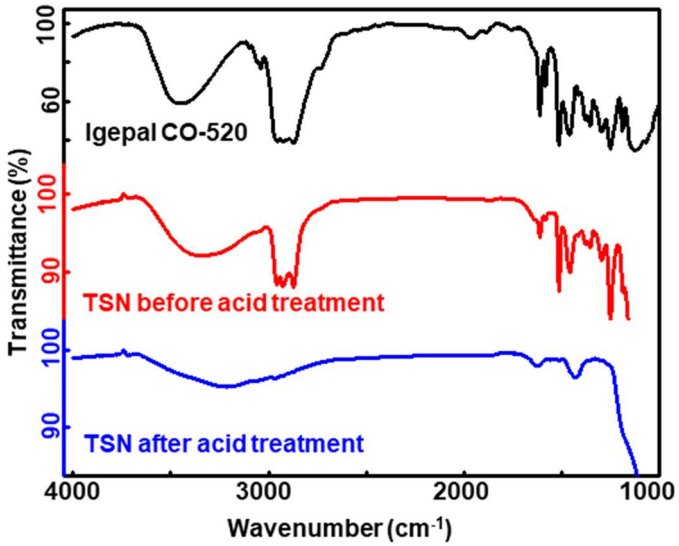

Figure 2.3. FT-IR spectra of surfactant, Igepal® CO-520 (black line), TSNs before the acid treatment which the surfactants are adsorbed (red line), and TSNs after the acid treatment (blue line).

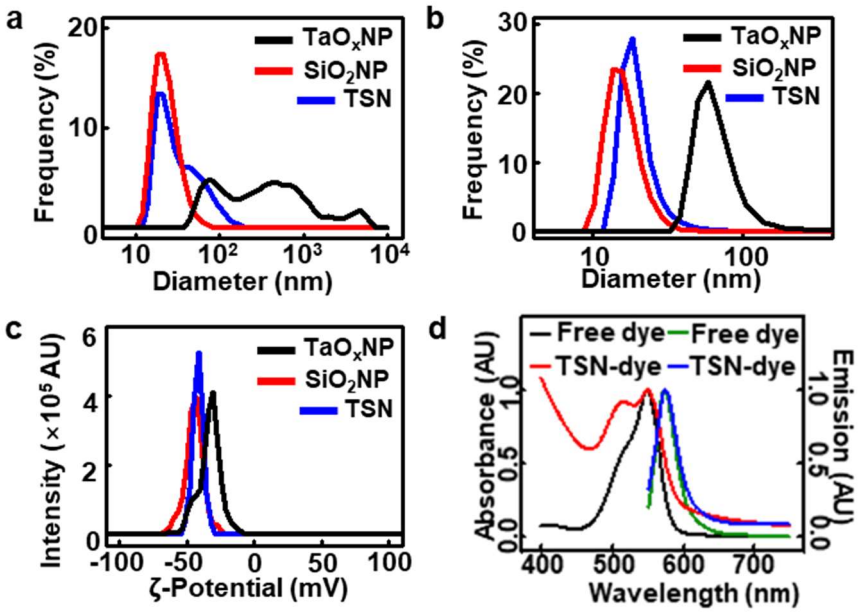

Figure 2.4. (a) Volume distributions of hydrodynamic diameter of SiO_2 NPs, and TSNs. (b) Number distribution. (c) ζ-potential intensity distributions. (d) Absorption and emission spectra of the tetramethylrhodamine isothiocyanate (TRITC) molecule and the TRITC-conjugated TSNs.

2.3.2 Tissue adhesive property and hemostatic capability

In order to evaluate the suitability of the TSNs for image-guided procedures, their adhesive property was examined with internal tissues containing biological fluids. Liver is an appropriate substrate because it contains abundant biological fluid and blood vessels which have to be sealed inside and it has rather uniform structures among the internal organs. The tissue adhesive property of TSNs was evaluated using a lap joint shear test of liver ribbons. Two liver ribbons were adhered together by gently pressing with a fingertip after spreading 15 μl of the glue solutions (TSNs, SiO_2 nanoparticles (SiO_2 NPs), TaO_x NPs, cyanoacrylate-Lipiodol mixture (CA-Lp), and TSNs coated with Igepal CO-520). Here, CA-Lp was used as a positive control group because it is a U.S. Food and Drug Administration-approved tissue adhesive form with a contrast effect and one of the most commonly used glue in image-guided procedures for human. When the upper ribbon was lifted with forceps, it held the lower ribbon without slipping (**Figure 2.5a**). Force-displacement curves were obtained using a universal test machine (UTM) as shown in **Figure 2.6**. In order to account for the large deviation of failure forces due to tissue heterogeneity, nine samples were measured for each type of glue (**Figure 2.6 and Figure 2.7**). The adhesive

strengths of all applied adhesives exceeded the intrinsic adhesion strength of biological tissues.

TSNs exhibit an adhesion strength comparable to that of CA-Lp (1:3) mixture that has enough contrast effect to be visualized in X-ray fluoroscopy (**Figure 2.16c and Figure 2.16d**). SiO_2 NP solution also shows similar strength with that of CA-Lp and TSNs. Although the TSNs show much lower adhesion strength than that of commercial CA, the CA is not detectable in X-ray imaging modalities, and unable to be used by itself in image-guided procedures. To determine the optimal concentration of TSN for adhesive properties, the adhesive strengths were measured with various TSN concentrations. Because the adhesive force increases with increasing nanoparticle concentration (**Figure 2.8**), the highest 40 wt% TSN solution was used for hemostasis or markers. The force-displacement curves of TSNs (Supplementary Fig. 5a) show a similar pattern to that of SiO_2 NPs, indicating that the adhesion characteristics of TSNs originate from nanoparticle adsorption onto the biological tissue surface and corresponding energy dissipation from the hydrogel-like soft tissues, as previously proposed.[19]

Gluing biological tissues with nanoparticles mainly depends on the ability of nanoparticles to adsorb onto tissues, which involves the interaction between the nanoparticle surface and biological molecules on tissues.[19,51] To investigate the adhesive mechanism of TSNs, we prepared various types of TSNs that are surface-functionalized with primary amine, carboxylate, and polyethylene oxide group (**Table 2.1, Figure 2.9**). All of these surface grafted TSNs exhibit no adhesive property (**Figure 2.10** and **Figure 2.11**). On the other hand, TSNs covered with Igepal CO-520 show fourfold reduced adhesive property than that of bare TSNs that are obtained by the complete removal of Igepal CO-520 by the acid treatment (**Figure 2.11**). Meanwhile, agglomeration of TaO_x NPs leads to the decrease of adhesion strength by half compared with TSNs (**Figure 2.4**). These results clearly demonstrate that the silica surface is mainly responsible for the adhesive property of TSNs. Furthermore, silica coating imparts colloidal stability of TSNs.

Adsorption of TSNs was investigated using scanning electron microscopy (SEM) and TEM. SEM and TEM images of the liver samples show localization of TSNs near hepatocytes and leaked subcellular vesicles from the damaged cells by the adsorption of TSNs near lipid layer (**Figure 2.12** and **Figure 2.13**). Moreover, entangling and

adsorption interactions between fibrin fibers and TSNs confirm that the adsorption and spontaneous network formation of TSNs on biological tissues enables the adhesion of cut liver tissues (**Figure 2.12h**).

After confirming their adhesive property, TSNs were applied to hemostasis in a liver puncture model. Since it is difficult to suture a highly vascularized liver wound, either tissue adhesives or sealants are necessary for the warranted closure of hepatic wounds. Puncture injuries were prepared by making a track with a sterile 18-guage needle in the livers of Sprague-Dawley (SD) rats. Subsequently, TSNs, SiO_2 NPs, or CA-Lp mixture was applied to each track as a hemostatic agent, or direct pressure was put onto the stab wound as a control. Because it is almost impossible to impose pressure in a minimally invasive procedure, no pressure was applied at the sites where the adhesives were treated. As shown in **Figure 2.15a**, both TSNs and CA-Lp successfully stopped bleeding immediately after their application. However, severe blood loss occurred in the control without any adhesives, even though direct pressure was exerted. The amount of bleeding was measured by the weight difference of a filter paper before and after absorbing the blood (**Figure 2.14**). A significant decrease in the amount of blood was

observed when TSNs, SiO_2 NPs, or CA-Lp was applied, and their hemostatic effects were similar (**Figure 2.15b**).

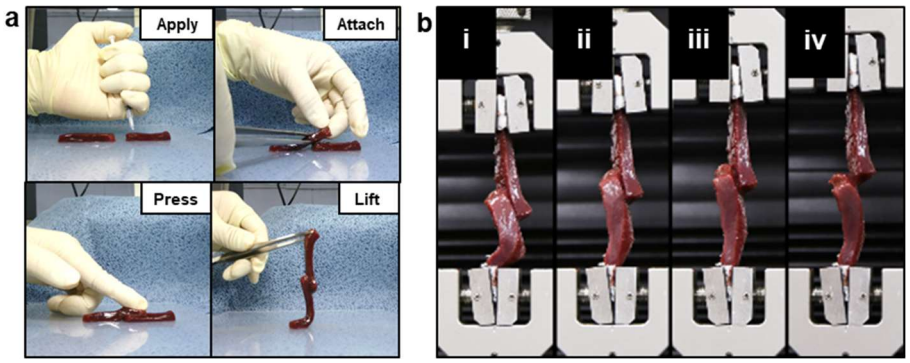

Figure 2.5. (a) Photographs showing the lap joint preparation procedure for analyzing adhesive strength of various glues on biological tissues of two calf liver ribbons: applying the adhesive, attaching by overlapping the ribbons at the region where the adhesive was applied, gently pressing the ribbon for 30 sec, and lifting up and moving the joint to be analyzed. (b) Photographs showing the lap joint shear test (i) lifting the lower ribbon, (ii) loading the stress, (iii) ultimate stress point and failure, and (iv) sliding.

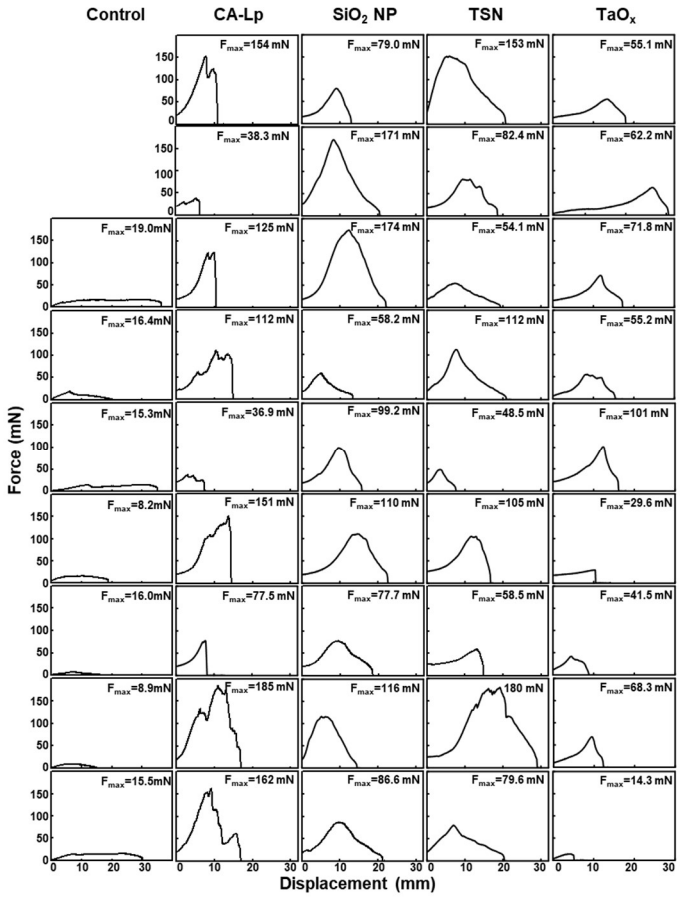

Figure 2.6. Normalized force-displacements curves of the lab joints made of ribbons cut from the calf liver and glued with intrinsic adhesive property of biological tissues (Control), CA-Lp, SiO_2 NPs, surfactant-free TaO_x/SiO_2 core/shell nanoparticles (TSN), and TaO_x NPs without SiO_2 shell. The failure force is shown upper left side of each curve.

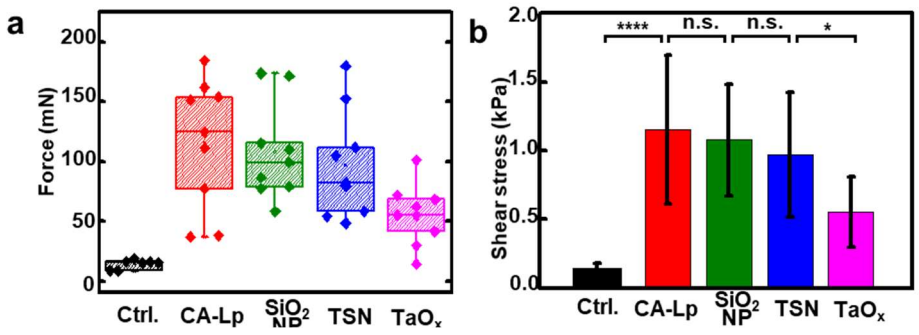

Figure 2.7. (a) Box plot for the failure forces of each adhesive. Each failure force is denoted with diamond, bars represent maximum and minimum values, and boxes with line are represented the interquartile range with median. (b) Bar plot of mean shear stress. Error bars show the standard deviation. *p* value were calculated by student's t-test. ****$p<0.0005$, *$p<0.05$, n.s., not significant $p>0.05$.

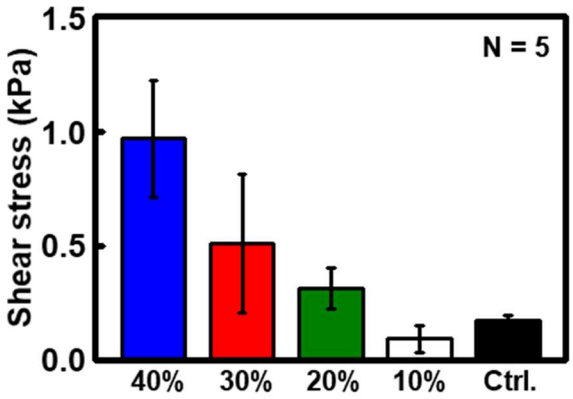

Figure 2.8. Concentration dependency of the adhesive strength of TSNs.

Table 2.1. Zeta-potentials and hydrodynamic diameters of TSNs with various surface moieties.

Sample	Silane for surface modification	Zeta-potential (mV)	Hydrodynamic diameter (nm)
Bare-TSN	None	-41.9 ± 4.1	20.4±7.2
PEG-TSN	2-[methoxy (polyethyleneoxy) 21-24propyl] trimethoxysilane	-32.3± 9.0	17.0±5.2
Carboxyl-TSN	N-(trimethoxysilyl propyl) ethylenediamine triacetate	-36.6± 10.6	18.4±5.3
Amino-TSN	3-aminopropyltriethoxysilane	38.0± 5.7	64.1±21.8

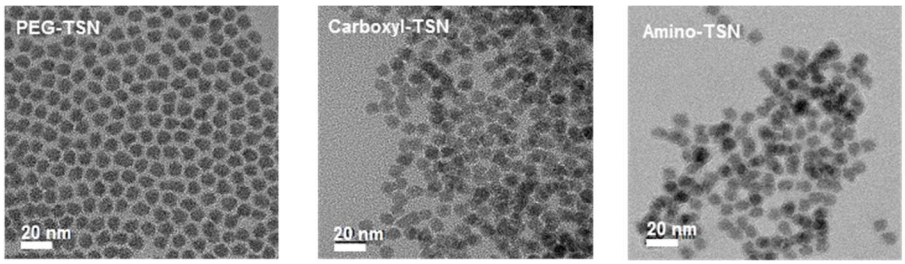

Figure 2.9. TEM images of surface modified TSNs.

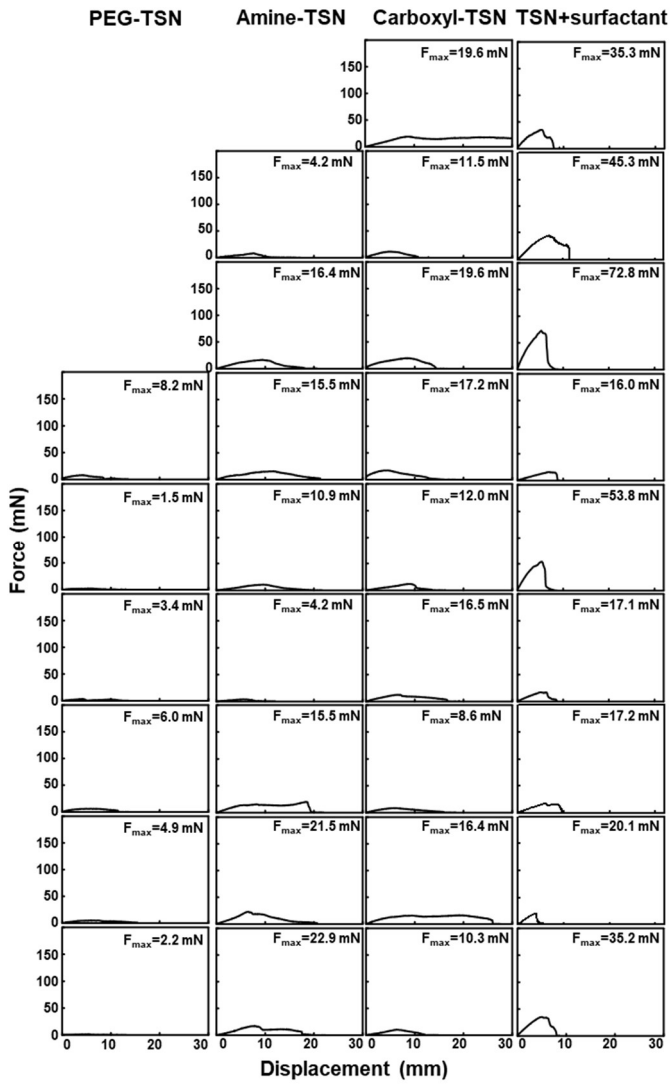

Figure 2.10. Normalized force-displacements curves of PEG-TSNs, Amine-TSNs, Carboxyl-TSNs, surfactant-adsorbed TSNs (TSN+Surfactant; without acid treatment). The failure force value is shown upper left side of each curve.

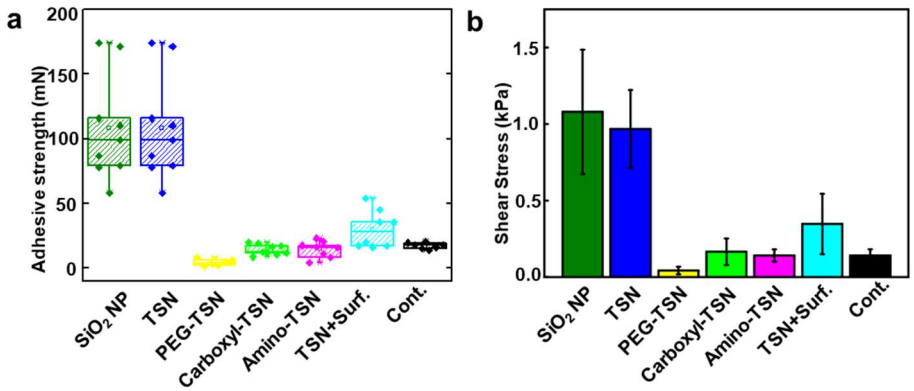

Figure 2.11. (a) Box plot for the failure force of each adhesive. Each failure force is denoted with diamond. Bars represent maximum and minimum values. Boxes with line represent the interquartile range with median. (b) Bar plot of mean shear stress. Error bars show the standard deviation.

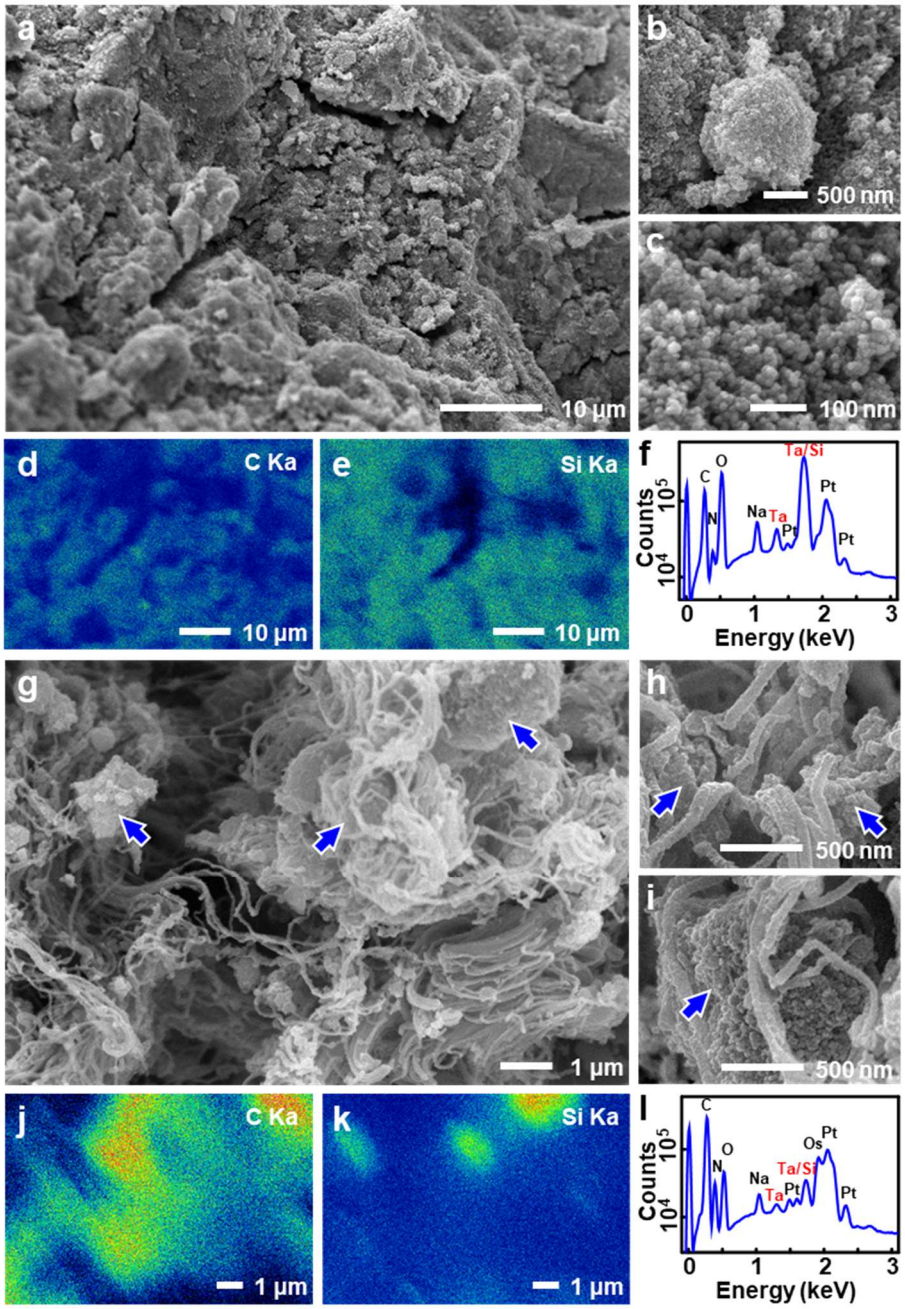
a
10 μm
b
500 nm
c
100 nm
d
C Ka
10 μm
e
Si Ka
10 μm
f
Ta/Si
C
O
N
Na
Ta
Pt
Pt
Pt
Counts
10^5
10^4
0
1
2
3
Energy (keV)
g
1 μm
h
500 nm
i
500 nm
j
C Ka
1 μm
k
Si Ka
1 μm
l
C
O
N
Na
Ta
Ta/Si
Pt
Os
Pt
Pt
Counts
10^5
10^4
0
1
2
3
Energy (keV)

Figure 2.12. (a) Scanning electron microscope(SEM) image of the side of liver where TSNs applied. (b) SEM image showing nanoparticles coating the leaked vesicle by adsorption. (c) Highly magnified image showing the adsorbed nanoparticles. (d) Carbon and (e) silicon elemental mapping of the image (a) by energy-dispersive X-ray spectroscopy (EDS) showing wide adsorption of TSN onto the liver section. (f), EDS spectra of image (a) showing the tantalum and silicon peaks. (g), SEM image where fibrin fibers are networked with TSN. The blue arrows point the locations of TSN agglomerates. (h,i) Highly magnified images in figure (g) showing the adsorption of TSN near fibrin fiber (h) and entanglement of TSN agglomerates within the fibrin fiber. (j) Carbon and (k) silicon elemental mapping of the image (g) by EDS. (l) EDS spectra of image (g).

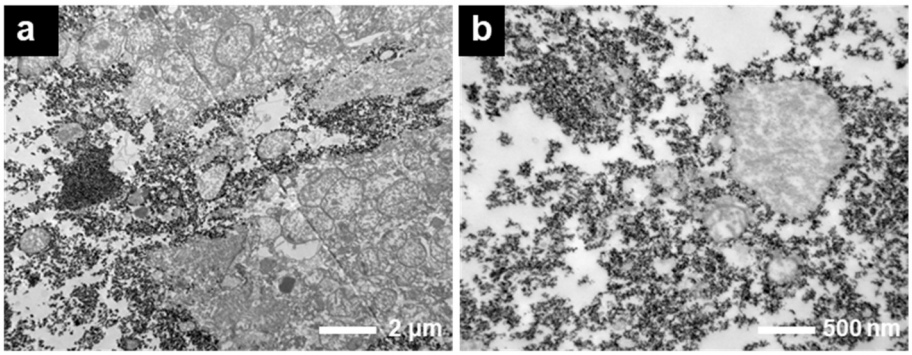

Figure 2.13. TEM images showing the adsorption of the TSN near and between hepatocytes (a) and leaked vesicles (b)

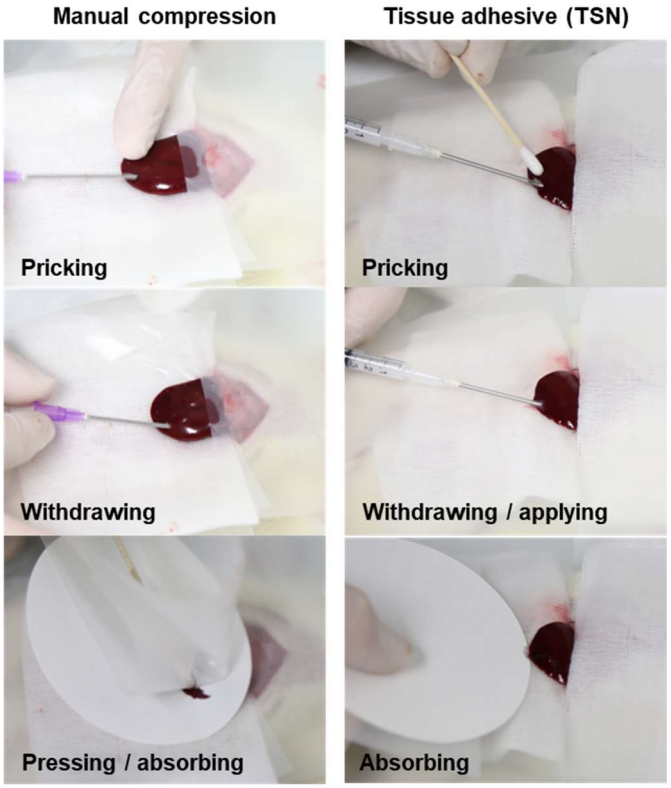

Figure 2.14. Procedures of evaluating hemostatic effects. After abdominal incision, the left lobe of the liver was placed on a hydrophobic film (Parafilm). An 18-gauge needle was advanced into the liver. Immediately after withdrawing the needle, prepared cotton swabs covered with a Parafilm and a filter paper were put onto the wound and manual compression was applied. On the other hand, prepared TSN or CA-Lp was injected during the withdrawal of the needle, and bleeding or residual adhesives were absorbed with a filter paper.

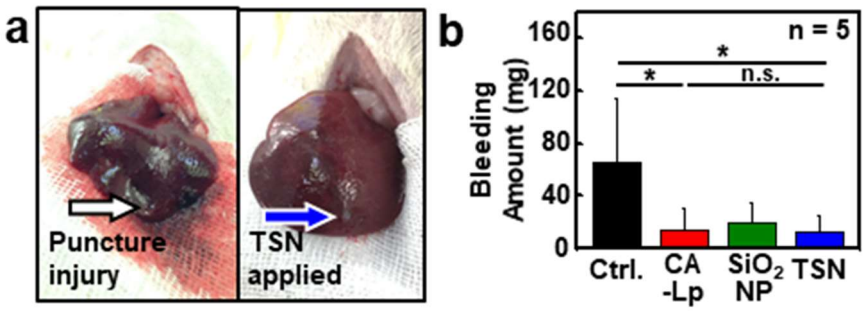

Figure 2.15. (a) Photographs of a stab wound after conducting each hemostasis procedure: direct pressure (left), applying TSNs (right). (b) Amount of bleeding during each hemostasis procedure. (*$p < 0.05$, and n.s., not significant $p > 0.05$, Student's *t*-test.)

2.3.3 Contrast enhancement in various medical modalities

The contrast effects of TSNs on fluoroscopy, CT, and ultrasonography were compared to those of SiO_2 NPs, CA-Lp, and a commercially available iodine contrast agent (Iopamidol). Since X-ray absorption of the contrast agents results in signal attenuation on fluoroscopy, their contrast effects were assessed by signal-to-noise ratios (SNR) (**Figure 2.16**). The X-ray fluoroscopic image reveals that TSNs significantly attenuate incident X-ray beam, showing a contrast efficiency comparable to that of iodine-containing CA-Lp. The SNR of TSNs is 15 times higher than that of SiO_2 NPs, demonstrating that the TaO_x core is responsible for the high X-ray attenuation. To evaluate the detection limit of TSNs on CT, we compared the CT numbers (Hounsfield unit, HU) of serially diluted solutions with different TSN concentrations (**Figure 2.17a, d**). The contrast effect increases linearly as the concentration increases, and both TSNs and iopamidol are distinguishable from water down to a concentration of 12.5 mg ml^{-1}. The contrast efficiencies of TSNs and iopamidol, calculated from the slopes of X-ray fluoroscopy SNR versus concentration, are 0.18 mg^{-1} ml and 0.17 mg^{-1} ml, respectively, while SiO_2 NPs exhibit a negligible contrast enhancement effect (1.8 × 10-4 mg^{-1} ml). The CT contrast enhancement effect of TSNs was also

evaluated by the slope of CT number versus concentration and compared with those of iopamidol and SiO2 NPs. The contrast enhancement of TSNs is 18.6 HU mg^{-1} ml, which is 1.5 and 150 times higher than those of CA-Lp (12.9 HU mg^{-1} ml) and SiO_2 NPs (0.12 HU mg-1 ml), respectively (**Figure 2.17b, e**). The stronger contrast effect of TSNs in CT can be attributed to the higher X-ray photon energy used in CT (applied voltage is 140 kV) compared to that used in fluoroscopy (60 kV), and the well-matched K-edge value of tantalum (67.4 keV) compared with that of iodine (33.2 keV).[31]

The high mass density of TSNs compared with that of water and flesh offers an effective scattering of US-waves, allowing for the use of TSNs in ultrasonography-guided procedures. The contrast enhancements of TSNs and SiO_2 NPs were investigated using an agarose phantom loaded with different concentrations of the nanoparticles (**Figure 2.17c, f**). The US signal of TSNs is distinguishable from the background starting from a nanoparticle concentration of 8 mg ml^{-1}, and the signal enhancement of TSNs is three times higher than that of SiO_2 NPs. It is well known that the back-scattered US generated from Rayleigh scattering is affected by the material size, compressibility and density difference from environment.[52] Therefore, not only a larger

hydrodynamic size of TSNs (20.4 nm) than that of SiO2 NPs (16.4 nm) but also a high density of the TaO_x core (~8.18 g cm^{-3}) contributed to the more intense US signals in comparison to those of SiO_2 NPs, enabling a much lower detection limit.

The in vivo contrast enhancement of TSNs in different imaging modalities was assessed using the aforementioned liver puncture model. As the contrast effects of TSNs and CA-Lp on fluoroscopy are similar, the liver columns filled with each glue exhibit almost identical contrast in the fluoroscope images (**Figure 2.18a**). Notably, the glues are clearly distinguished from the ribs with a similar thickness, which can be advantageous in clinical situations. Similarly, CT imaging reveals that the mean HU value of TSNs is 1.8 times greater than that of the vertebrae and slightly higher than that of CA-Lp (**Figure 2.18b**). Since it is hard to compare directly the contrast enhancements on ultrasonography in a rat due to the small size of its liver, the contrast enhancement of TSNs, CA-Lp, and SiO_2 NPs was investigated using the calf liver injected with each glue at a depth of 4 cm. The bright mode (B-mode) ultrasonography imaging shows that the signals from SiO_2 NPs and TSNs are bright enough to be distinguished from the background liver tissue. Although

the reflection of US waves from the CA-Lp applied tissue could be detected, its difference from background is insignificant (**Figure 2.18c**).

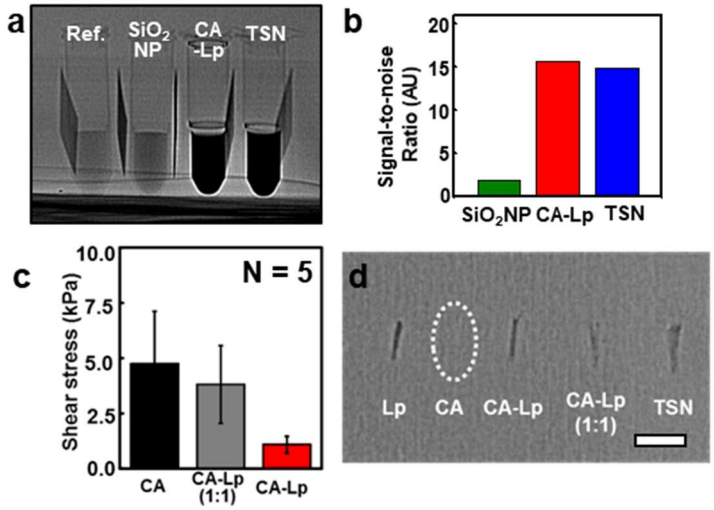

Figure 2.16. Contrast enhancement on X-ray fluoroscopy (a) an image of the tubes containing water (Ref.), commercial silica nanoparticle solution (SiO_2 NPs, 50 wt%), mixture of cyanoacrylate adhesive and iodized oil (CA-Lp, 75% of Lipiodol, 360 mgI ml^{-1}), and TSNs (40 wt%); (b) plots of the calculated signal to noise ratio). (c) Mean shear stress of cyanoacrylate (CA; Histoacryl) and cyanoacrylate-Lipiodol mixture (CA-Lp) with a volume ratio of 1:1 and 1:3. (d**)** Fluoroscopy image of applied adhesives in agarose gel. White dashed circle indicates the position where CA was applied.

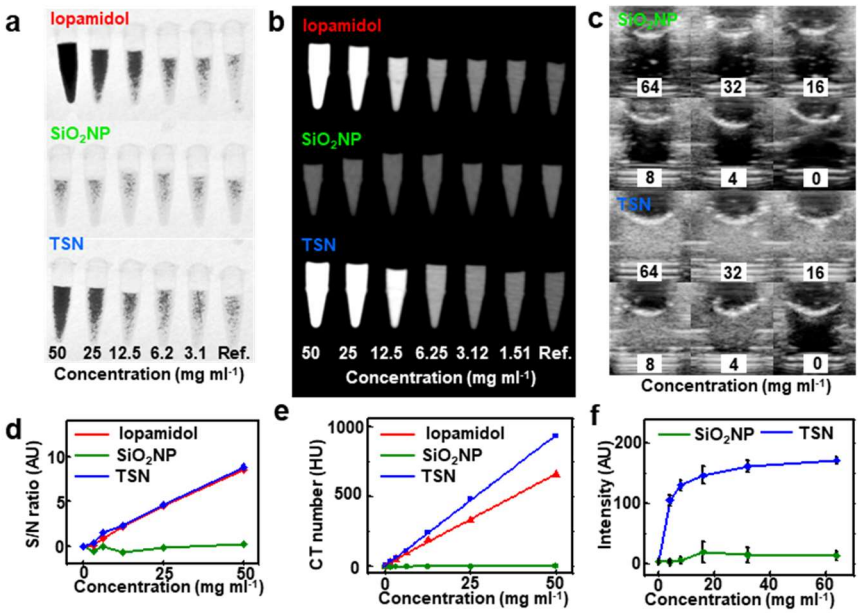

Figure 2.17. Comparison of the contrast effects on fluoroscopy, CT, and ultrasound imaging. (a) Fluoroscopic images of the microtubes containing Iopamidol, SiO_2 NPs, TSNs with various concentrations. (b) CT images of the microtubes containing the Iopamidol, SiO_2 NPs, and TSNs. (c) Ultrasound images of the agarose phantom containing NPs with various concentration. (d) Plots of the signal-to-noise ratio increase depending on the concentration. (e) Plots of the CT values of the Iopamidol (red), SiO_2 NP (green), TSN (blue) calculated from CT images (b). (f) Plots of the signal intensity increase of the SiO_2 NPs (green), TSNs (blue) from ultrasonography (c).

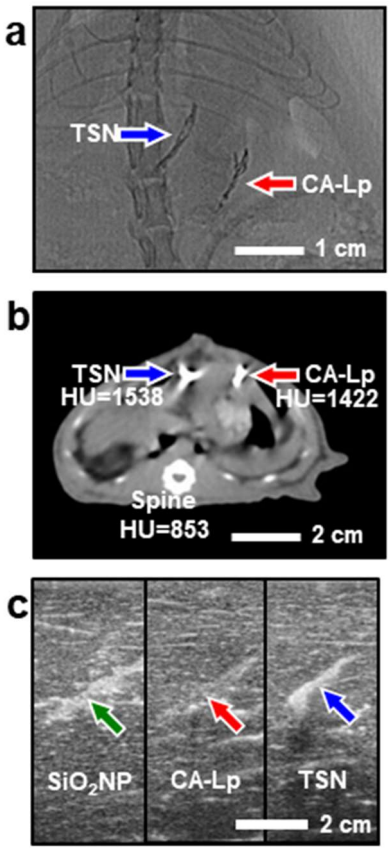

Figure 2.18. *in vivo* images of a Sprague Dawley (SD) rat after application of TSNs and CA-Lp on fluoroscopy (a) and CT (b). On the CT image (b), the mean CT values (Hounsfield unit, HU) of each region of interest (TSN, CA-Lp, and bone) were measured. (c) Ultrasonography images of the calf liver where SiO_2 NPs, CA-Lp and TSNs were injected.

2.3.4 Biocompatibility

One of the major hurdles for intracorporeal use of CA-Lp is its severe toxicity and the inflammatory reactions caused by the by-products of CA-Lp such as formaldehyde.[5,53,54] Recent reports, however, have shown that both SiO2 and TaO_x nanoparticles are highly biocompatible. Moreover, tantalum-based stents and implants, and tantalum powder-containing embolic materials (Onyx; Covidien, Irvine, CA) are frequently used in clinics thanks to their biocompatibility.[23,27,41,55,56] To ensure the biocompatibility of TSNs, their cytotoxicity was evaluated using cell morphology analysis and viability assays. To mimic in vivo glue application conditions, a small drop of glue-gel was placed at the bottom center of a culture dish, upon which a cell suspension was added. After 24 h, most of the cells incubated with the TSNs were attached to the plate surface regardless of their distance from the gel, while the cells near CA-Lp failed to attach to the plate surface and exhibited a round shape (**Figure 2.19a**). Methylthiazole tetrazolium (MTT) assay shows that the viability of the cells incubated with CA-Lp decreases in a dose-dependent manner while those cells incubated with TSNs exhibit little cytotoxicity up to a concentration of 800 μg ml^{-1}, demonstrating excellent biocompatibility of TSNs (**Figure 2.19b**). SiO_2 NPs have a

lower cytotoxicity than CA-Lp, but they still show a significant cytotoxicity at a high concentration of 800 μg ml^{-1}. Since SiO_2 NPs are known to induce hemolysis, the hemolysis effects of TSNs were investigated. As shown in **Figure 2.19c**, most of the red blood cells were lysed at a SiO_2 NP concentration of 100 μg ml^{-1}, but the hemolysis rate by TSNs was much lower.

Because both TSNs and SiO2 NPs have similar silica structure, the observed difference in their hemolytic effect is unexpected. To understand the difference of their hemolysis effect, we evaluated the influence of the nanoparticle size, the amount of fluorescent dye, and the thickness of silica shell on hemolysis rate. Hemolysis rate of silica nanoparticles with sizes of 22 nm, 30 nm, and 105 nm reveals that the largest 105 nm-sized NPs exhibit lower hemolysis rate than that of the 22 nm- and 30 nm-sized silica nanoparticles (**Figure 2.20**), which is consistent with the previous report.[57,58] The amount of incorporated dye does not affect the hemolysis rate of TSNs and SiO2 NPs (Supplementary Fig. 13d, e, and f). Most strikingly, TSN-5 with 5 nm-thick silica shell show much higher hemolysis rate than TSNs with 1 nm-thick silica shell and TaO_x NPs without silica shell (**Figure 2.20h**).

In the previous reports, hemolysis by silica nanoparticles was attributed to the direct interaction between the cell membrane and silanol groups on the nanoparticle surface[57,58], and the mesoporous silica nanoparticles are known to exhibit lower hemolytic effect than dense silica nanoparticles. The microporous structure of TSNs seems to be responsible for their lower hemolysis rate compared to that of the dense silica nanoparticles (see the gas adsorption data in **Figure 2.21**).

In vivo biocompatibility of TSNs was assessed by histologically analyzing the tissues after applying TSNs or CA-Lp in a liver puncture model (**Figure 2.22** and **Figure 2.23**). A significant difference in the level of tissue inflammation was observed between the biological tissues treated with TSNs and those with CA-Lp. Consistent with the previous reports, an immediate immune reaction was identified around the CA-Lp applied regions within 3 days, and this response developed to a severe inflammation in and around the adhesives at 14 days, and persisted over 56 days.[54] In contrast, the TSN was observed to be innocuous, which is consistent with the previous report on the inertness of tantalum. As the tantalum oxide is a chemically stable material, the degradation of TSNs is slow compared to that of polymer adhesives as shown in histological analysis.

The inertness of the tantalum oxide in TSNs was also supported by the extremely slow dissolution of tantalum in body fluid (**Figure 2.24**). Only little portion spreads to other organs including liver, spleen, and lung, and most of the nanoparticles (>99.5%) remains in the applied position (**Figure 2.25**). Over six weeks, there was no adverse effect in our blood test, proving their long-term biocompatibility in vivo (**Figure 2.26**). Considering the intracorporeal use of adhesives for image-guided procedures, their low cellular toxicity, low inflammatory reaction derived from the chemical stability of oxides, and proved long-term biocompatibility can be crucial advantages over CA-Lp.

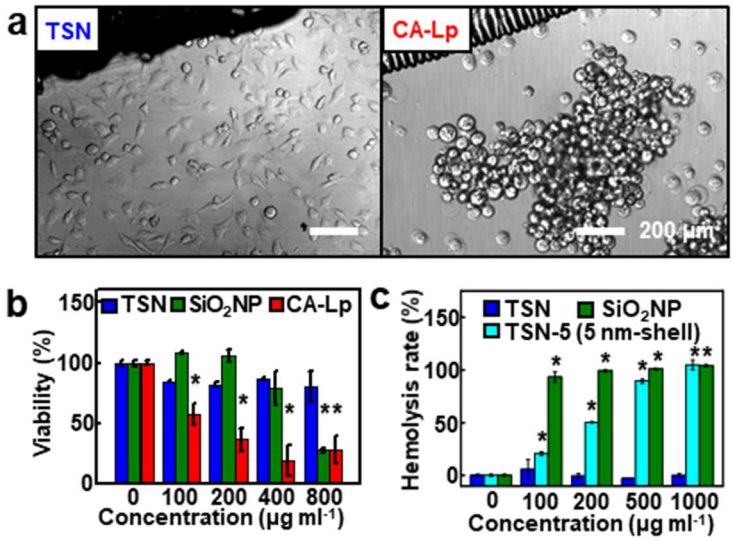

Figure 2.19. (a) Cellular morphology of mammalian cells (HeLa cell line) incubated where the TSN (left) or CA-Lp (right) glue was applied. (b) Viability of cells treated with TSNs, SiO_2 NPs, and CA-Lp. (c) Concentration-dependent hemolysis rate of TSNs, SiO_2 NPs, and TSN-5 with 5 nm-thick silica. Error bars indicate standard deviations (n = 3, *p < 0.05, Student's t-test, compared with the control group).

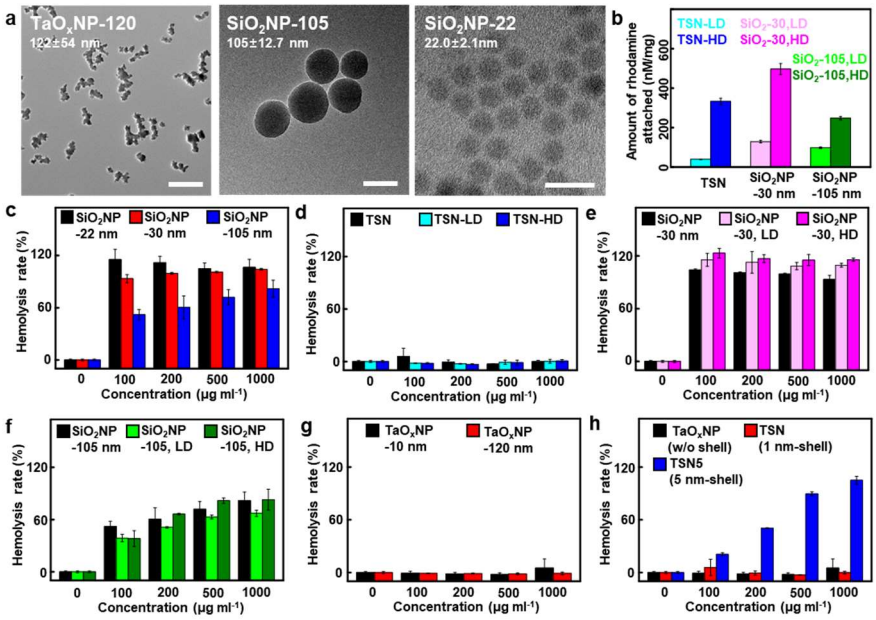

Figure 2.20. Comparative study of hemolysis effects of TSNs, SiO_2 NPs, TaO_x NPs. (**a**) TEM images of TaO_x NPs-120 nm, SiO_2 NPs-105 nm, and SiO_2 NPs-22 (**b**) Quantification of rhodamine attached onto the TSN, SiO_2 NP-30 (Ludox TM-50; TEM image in Supplementary Figure 4d), and SiO_2 NP-105, prepared with low (LD) and high (HD) dye concentration. (**c**) Hemolysis rate of silica nanoparticles with sizes of 22 nm, 30 nm, and 105 nm reveals that the largest 105 nm-sized NPs exhibit lower hemolysis rate. (**d-f**) Hemolysis rates of TSNs, SiO_2 NP-105, and SiO_2 NP-30 with different amount of rhodamine dye incorporation reveal that the amount of incorporated dye does not affect the hemolysis rate. (**g**) Hemolysis rate of TaO_x NPs with sizes of 11 nm and 120 nm reveals that both TaO_x NPs exhibit negligible hemolysis effect. (**h**) TSNs with thicker silica shell exhibits higher hemolysis rate than TSNs with thinner silica shell and TaO_x NPs.

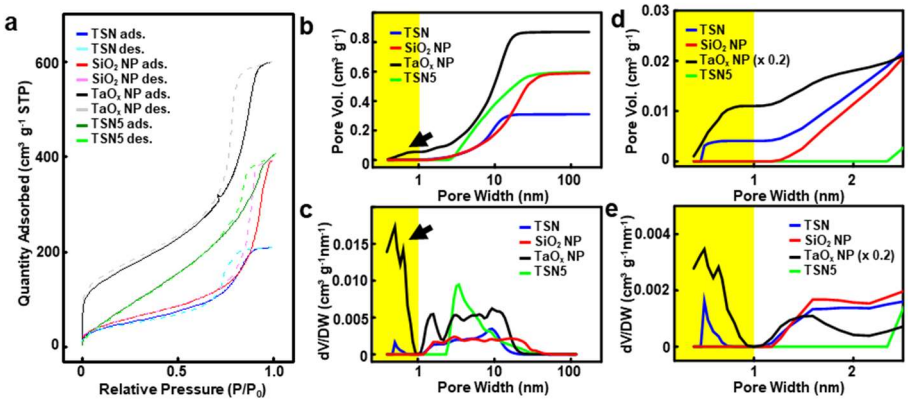

Figure 2.21. Gas adsorption analysis of TaO_x/SiO_2 NPs with 1 nm-thick silica shell (denoted as TSN), SiO_2 NP, TaO_x NP, TaO_x/SiO_2 NPs with 5 nm-thick silica shell (denoted as TSN5) (a) N_2 adsorption-desorption isotherm of TSN, SiO_2 NP, TaO_x NP, and TSN12. (b-c) Cumulative pore volume and pore size distributions. The black arrows indicate the microporous structure of TaO_x NPs. (d-e) enlarged plots showing the micro-pore region. The mirco-pore region is shaded with yellow box. Pore size distributions were calculated with density functional theory method.

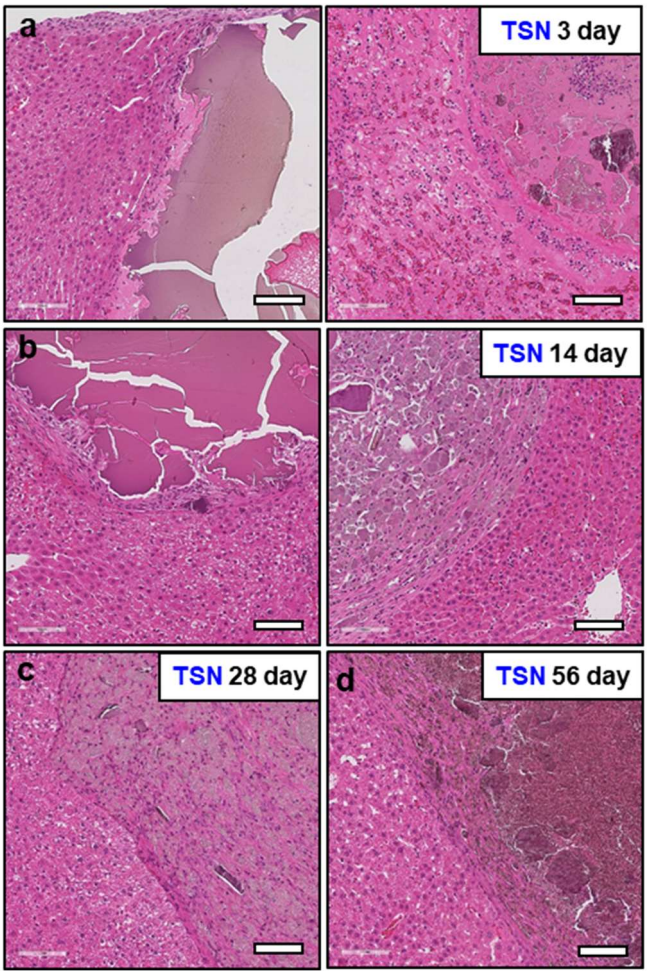

Figure 2.22. Histological analyses for biocompatibility of TSN. Tissue specimens stained with hematoxylin and eosin (H&E) (a) 3, (b) 14, (c) 28, (d) 56 days after implantation of TSN.

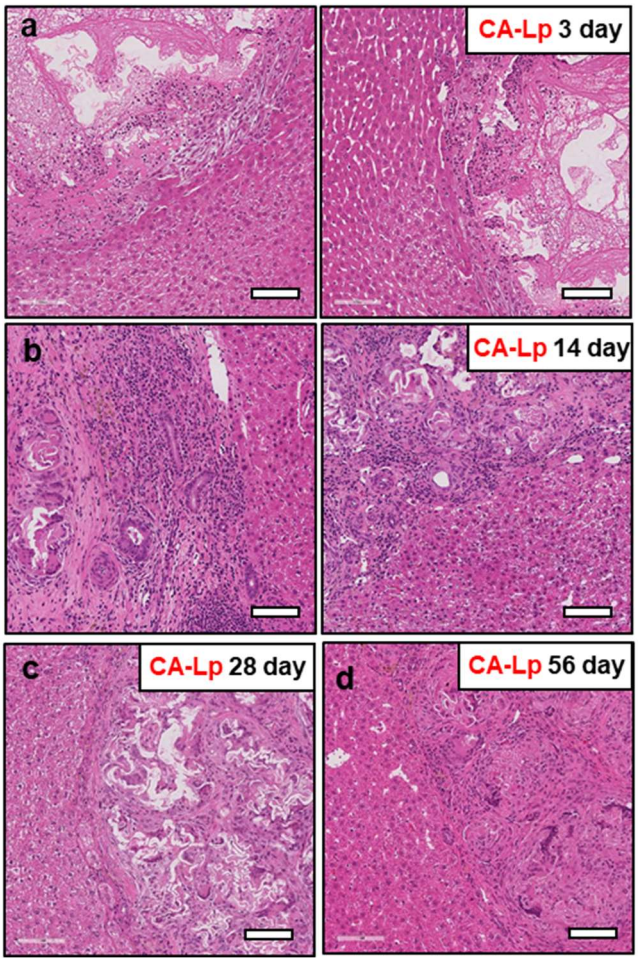

Figure 2.23. Histological analyses for biocompatibility of CA-Lp. Tissue specimens stained with hematoxylin and eosin (H&E) (a) 3, (b) 14, (c) 28, (d) 56 days after implantation of TSN.

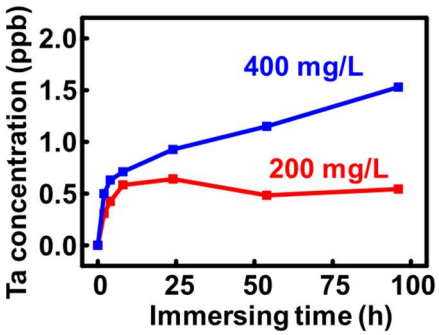

Figure 2.24. The concentration of dissolved Ta from TSNs in simulated body fluid, depending on immersing time and immersed amount of the TSNs.

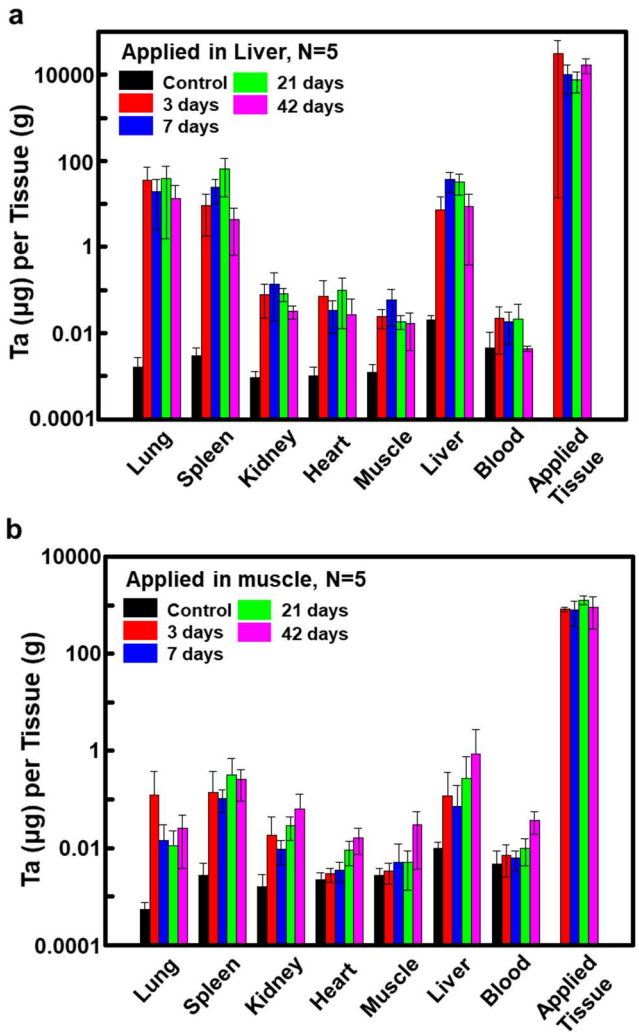

Figure 2.25. Average concentration of tantalum element in tissues obtained at 3, 7, 21, and 42 days after the application of TSNs as hemostatic agent for liver puncture models (a), and as fiducial marker for the muscles (b).

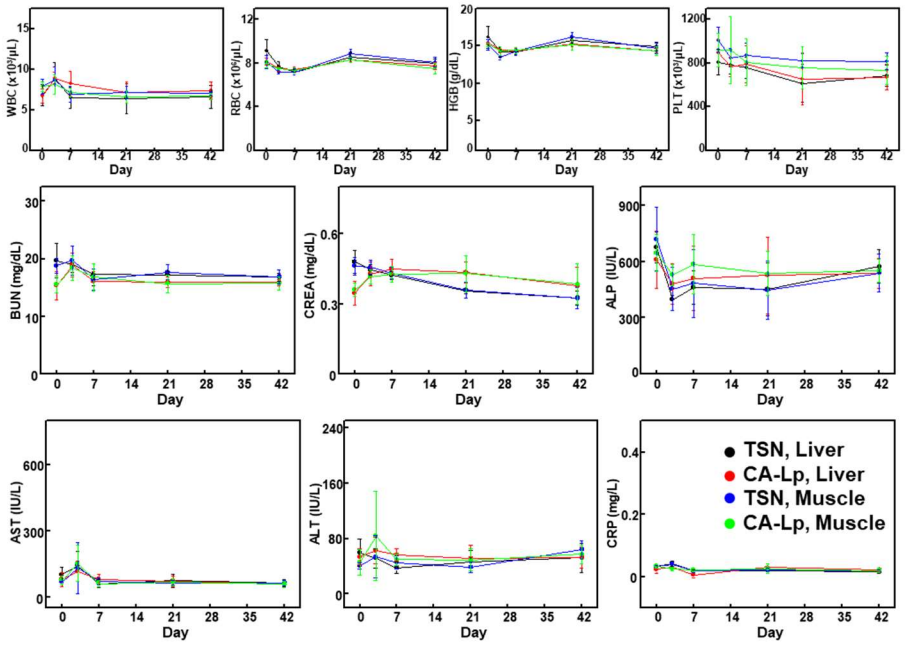

Figure 2.26. Long-term complete blood count (CBC) results for WBC, RBC, HGB, and PLT. Long-term serum biochemistry results for BUN, CREA, ALP, AST, ALT, and CRP from the Sprague Dawley rats (n=5). The analyses were proceeded after applying glues (TSNs, CA-Lp) to the liver and muscle.

2.3.5 Real-time image-guided procedures

To investigate the potential of TSNs for image-guided surgery, we conducted two surgical demonstrations to show their utility not only as an adhesive for medical intervention with real-time imaging modalities but also as an anatomical marker to guide resection and/or radiotherapy. The liver puncture model was performed in a rabbit without abdominal incision under the guidance of fluoroscopy and ultrasonography (**Figure 2.27**). Using dynamic X-ray fluoroscopic imaging, we could distinguish TSNs from other organs including vertebrae, in spite of low X-ray energy and short exposure time (60 kV and 1 ms, respectively). In ultrasonography, the TSNs that filled the liver track appeared as a bright area. Moreover, there was no bleeding through and on the skin, indicating successful hemostasis of connective tissues and dermal wounds. Thus, TSNs can support minimally invasive real-time procedures with their greatly enhanced contrast effect, enabling both multimodal imaging capability and adhesive property.

In addition to the potential of TSNs as a tissue adhesive, TSNs were also applied as a surgical marker (also called as a fiducial marker) in image-guided procedures. In image-guided procedures or radiotherapy,

the movement of soft tissues often hinders localizing and registering an operative region. Some metal-based solid implants, such as a small gold rod or coil, have been used as markers of soft tissues.[11] However, their large physical dimensions usually require complicated insertion procedures that increase the risk of adverse events,[59] and those solid implant markers usually cause streaking artifacts in CT imaging.[60] Although injectable liquid fiducial markers have been proposed, their unwanted migration can lead to serious localization errors as well as complications in distant tissues. To compare mobility, five different fiducial markers including TSNs, gold rod, metal coil, Lipiodol, and CA-Lp were implanted in calf lung and liver samples ex vivo and these samples were subsequently shaken and CT images are compared. Unlike other materials which incited strong artifacts (gold rod, metal coil) or which moved substantially (Lipiodol), TSNs were immobile during the experiment and caused only negligible artifacts on CT imaging (**Figure 2.28** and **Figure 2.29**). TSNs are ideal fiducial markers due to their detectability by various imaging modalities and their strong adhesion to soft tissues. Moreover, for optical imaging, the fluorescent dye molecules conjugated on TSNs can prevent the rapid dye diffusion that usually results in the blurring of injection sites.

To check the reliability of the TSNs as a fiducial marker within actively moving tissues, TSNs were injected into the thigh and calf muscles of rats. The injected TSNs could be clearly visualized by CT and fluoroscopy, and their positions and shapes were retained during the flexion and extension of the leg (**Figure 2.30**). Micro-CT images showed that the locations of the TSN markers did not change over two weeks (**Figure 2.31**). In addition, TSNs in the muscle were readily detected by fluorescence imaging (**Figure 2.30c**), which can help surgeons recognize a surgical target and perform a safe and accurate operation.[61]

Lastly, the feasibility of the TSN marker was evaluated with a rat model of syngeneic lung cancer. Indeed, fiducial markers are usually required for successful resection and radiotherapy of lung cancer, but its placement in the lung is challenging because of risks such as migration and distant embolism via the pulmonary veins.[62,63] Localizing and marking of target lesions with rhodamine-attached TSNs were conducted with the aid of CT (**Figure 2.31b**). Neither abnormal breathing nor behavior was observed during and after the procedures. TSNs were clearly identified in the index tumors on both fluoroscopy and CT (**Figure 2.30**). The opacity of TSNs was high enough to be clearly distinguished from the nearby ribs and vertebrae of the rat. After thoracic

incision, fluorescence signals of the rhodamine-attached TSNs were clearly observed from the lesion (**Figure 2.30g**). Both the radiopacity of the TSNs and the high fluorescent signal from rhodamine would help in guiding the resection of the lesion. Considering that the leg and lung move vigorously by the physiological motion of rats, the retention of TSNs represents their great potential as a fiducial marker.

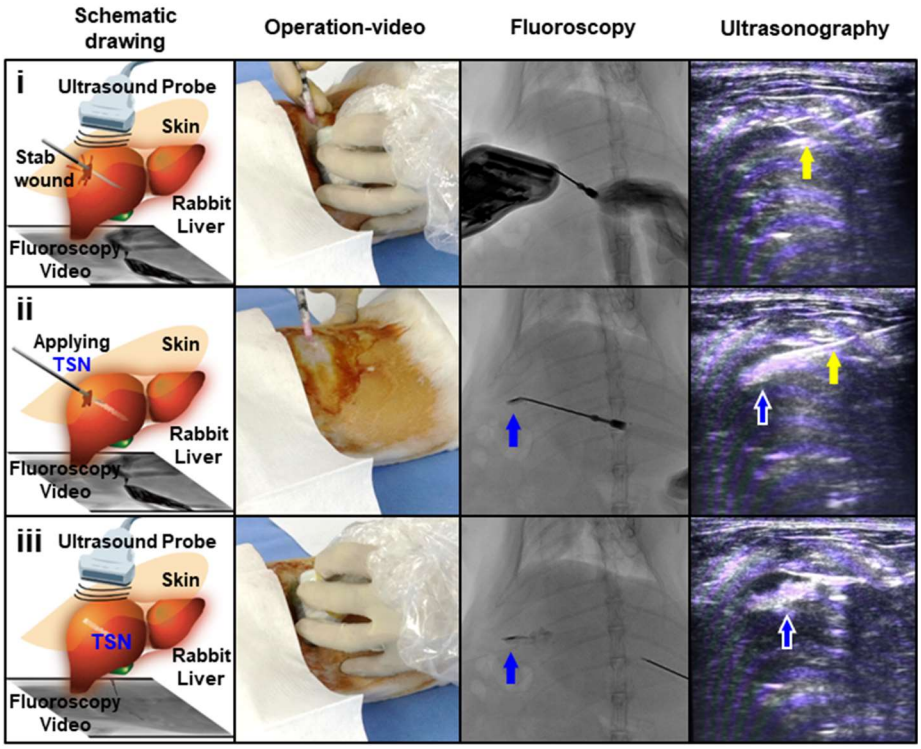

Figure 2.27. Series of schematic drawings, still images of operation-video, real-time fluoroscopic video, and ultrasonography. Each step represents; (i) making a stab wound with a needle, (ii) applying TSNs for hemostasis during withdrawal of the needle, and (iii) imaging for the post-procedural validation. On the images, blue and yellow arrows indicate TSNs and a needle, respectively.

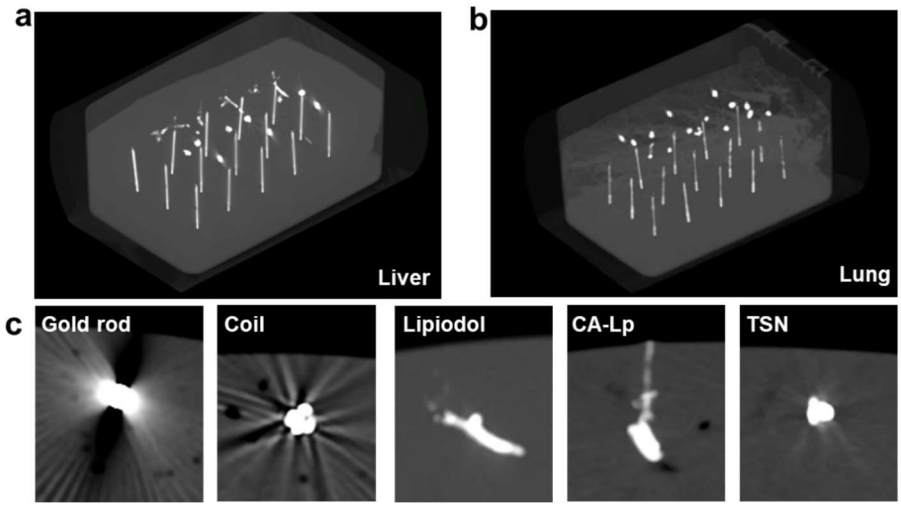

Figure 2.28. Mobility evaluation of fiducial markers including TSNs, gold rod, metal coil, Lipiodol, and CA-Lp. Three-dimension rendered X-ray CT images of the liver (a) and lung (b) which contains various fiducial markers. (c) CT images of each marker. The streak artifacts around the gold rod and coil hinder accurate imaging of the nearby tissue.

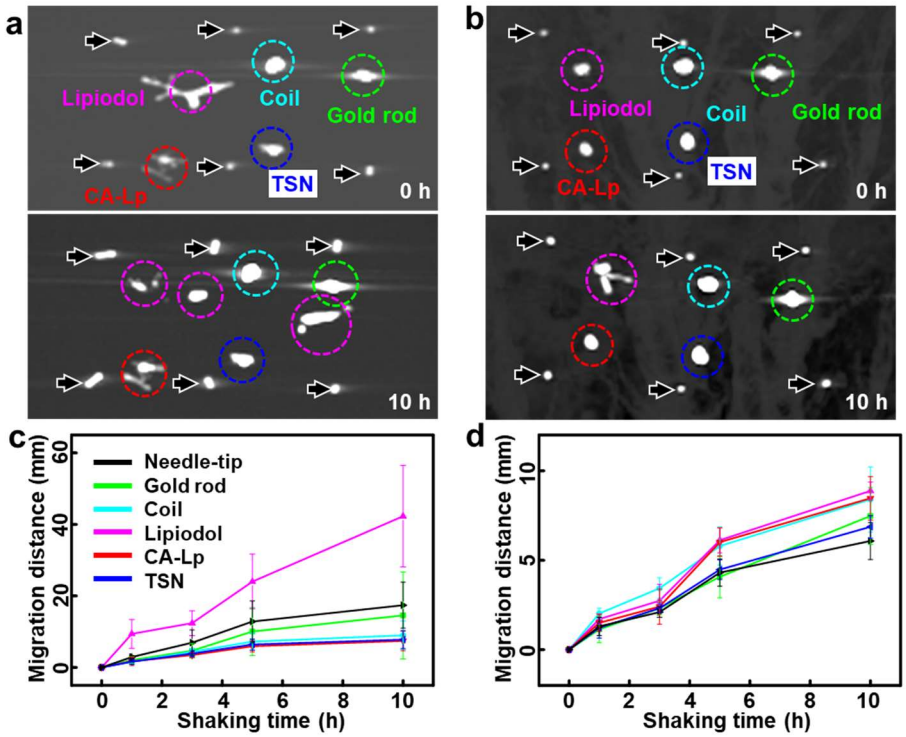

Figure 2.29. Top views of the (a) liver and (b) lung showing the positions of the fiducial markers and needles, before shaking (top) and after shaking (bottom). Black arrows indicate needle tips, and dashed circles indicate the markers. Average migration distances of markers in the (c) liver and (d) lung.

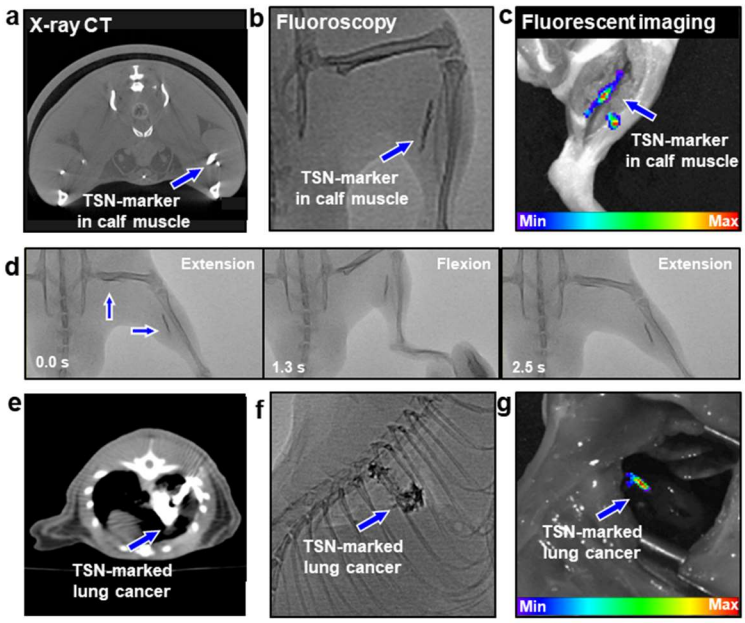

Figure 2.30. Multimodal imaging of the TSNs as an injectable fiducial marker implanted to the calf muscles of a SD rat. (a) Transversal micro-CT image showing the location of TSNs near the fibula (calf bone). (b) Fluoroscopic image of the implanted TSNs along with the fibula. (c) Fluorescent weighted image of the same region. (d) A series of still cuts of fluoroscopic video. (Blue arrows indicate the TSN markers, and the numbers in the picture represent the time of each frame.) Multimodal imaging of the percutaneously injectable TSN marker in rat lung cancer. (e) Axial image of CT. (f) Lateral view on fluoroscopy. (g) Fluorescence imaging after thoracostomy.

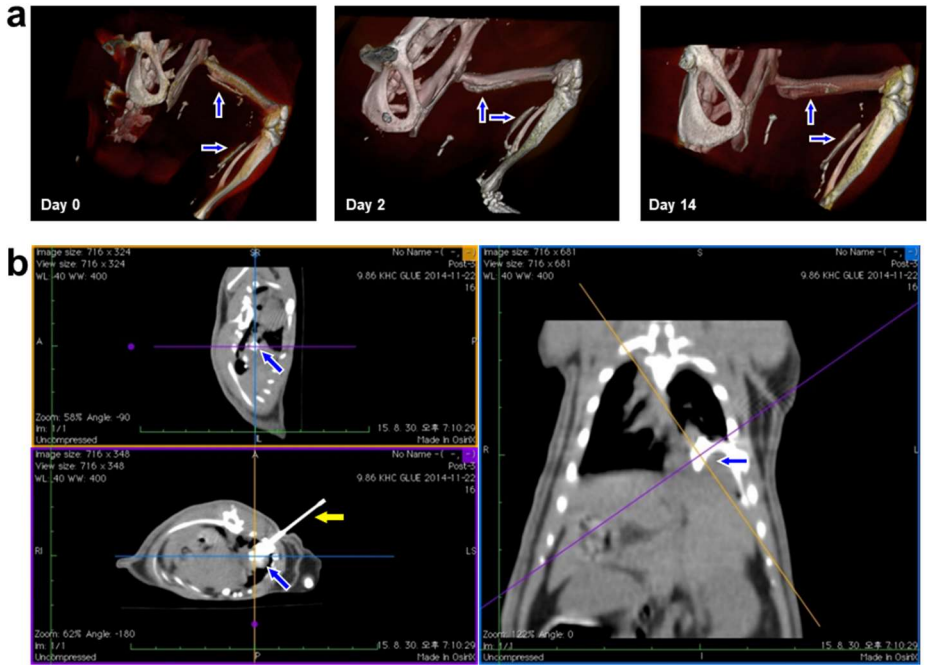

Figure 2.31. (a) 3D-rendered micro-CT images of the TSN-marked leg muscles of a rat; imaged right after the implementation, after 2 days passed, and after 2 weeks passed. The two blue arrows indicate the TSNs markings in the thigh and calf muscles along with the fibula and femur. (b) Multiplanar-reformatted CT images during percutaneous lung tumor marking procedure with fluorescent TSNs. The needle and injected TSNs are visualized on an axial cross-section image (lower-left).

2.3.6 Discussion

Due to the recent development of medical imaging techniques and interventional devices, many surgeries have been aided by image-guided and minimally-invasive procedures. For example, conventional surgeries for vessel occlusion, bleeding control, internal organ biopsy, spondylosis, and some early-stage tumors (e.g., hepatocellular carcinoma) are being replaced by percutaneous angioplasty, catheter-directed embolotherapy, needle biopsy, vertebroplasty, and radiofrequency/microwave ablation, respectively, all of which are conducted under the guidance of medical imaging.

However, nanomaterials relevant to the image-guided procedures are rarely suggested for use in medical practice. Ideally, they should be identifiable on clinical imaging (e.g., X-ray fluoroscopy, CT, US, and magnetic resonance imaging), convenient to apply percutaneously with a catheter or needle, biocompatible to minimize adverse reactions in body, and able to achieve surgical goals (e.g., hemostasis, tissue adhesion, and tissue marking). Given the unique possibilities of nanomaterials, including high image contrasting effects, adhesive properties, and dispersibility in various fluids, biocompatible NPs have enough potential

to replace the conventional materials used in image-guided procedures. In this context, TSNs can be a representative material that satisfies various requirements for medical applications by providing imaging capability, convenient administration, biocompatibility, and effectiveness.

The inertness of tantalum oxide not only provides good biocompatibility, but also hinders its biodegradation in body. Unlike typical imaging studies by systemic intravenous administration of contrast agents, image-guided procedures usually require a very small quantity of NPs. Compared with the required amount of Tantalum used as an intravenous CT contrast agent (840 mg kg^{-1})[41], our study utilized less than one fiftieth of Tantalum (15 mg kg^{-1}), which accounted for only 0.02 ~ 0.05 ml. Moreover, almost all TSNs are remained in the target areas without severe adverse reactions, suggesting that the systemic effects of TSNs can be minor, when administered locally with image guidance.

As a fiducial marker prior to a surgery, poor biodegradability hardly causes a problem because both the index tumor and the marker will be removed together (en bloc). In radiotherapy, persistent marking

of an index tumor facilitates the consistent targeting and follow-up during serial treatments. As a non-degradable tissue adhesive and a fiducial marker, TSNs exhibit substantially ameliorated inflammatory reactions compared with the clinical adhesive mixture, CA-Lp.

2.4 Conclusion

In conclusion, we designed and synthesized multifunctional and biocompatible tantalum oxide/silica core/shell nanoparticles (TSNs) composed of radiopaque tantalum oxide core with multimodal imaging capability and silica shell with a strong tissue adhesive property. As designed, the TSN glue is clearly visualized by clinical imaging modalities including X-ray fluoroscopy, CT, and ultrasonography, and exhibits adhesive property similar to that of the CA-Lp. Furthermore, the TSNs cause much less cellular toxicity and less inflammation than the clinically-used CA-Lp, which is very important for intracorporeal use of adhesives for image-guided procedures.

The current studies demonstrate the applications of TSNs to hemostatic adhesive for minimally invasive procedures and as immobilized marker for image-guided procedures by combining their multifunctional characteristics and tissue adhesive property. Given the needs of various tissue adhesives in medicine, our results give additional insights on biomedical applications of designed multifunctional nanoparticles, which can be expanded to image-guided procedure and regenerative medicine as well as drug delivery and cancer diagnosis.

Most of the contents of this chapter were published in the article, "Multifunctional nanoparticles as a tissue adhesive and an injectable marker for image-guided procedures." (*Nature communications* **2017, *8*, 15807)

2.5 References

[1] A. P. Duarte, J. F. Coelho, J. C. Bordado, M. T. Cidade, M. H. Gil, *Prog. Polym. Sci.* **2012**, *37*, 1031.

[2] W. D. Spotnitz, *Am. Surg.* **2012**, *78*, 1305.

[3] E. Dolgin, *Nat. Med.* **2013**, *19*, 124.

[4] N. Annabi, A. Tamayol, S. R. Shin, A. M. Ghaemmaghami, N. A. Peppas, A. Khademhosseini, *Nano Today* **2014**, *9*, 574.

[5] D. Garcia Cerda, A. M. Ballester, A. Aliena-Valero, A. Caraben-Redano, J. M. Lloris, *Surg. Today* **2015**, *45*, 939.

[6] H. Lee, B. P. Lee, P. B. Messersmith, *Nature* **2007**, *448*, 338.

[7] C. M. Elvin, T. Vuocolo, A. G. Brownlee, L. Sando, M. G. Huson, N. E. Liyou, P. R. Stockwell, R. E. Lyons, M. Kim, G. A. Edwards, G. Johnson, G. A. McFarland, J. A. M. Ramshaw, J. A. Werkmeister, *Biomaterials* **2010**, *31*, 8323.

[8] M. R. Jackson, *Am. J. Surg.* **2001**, *182*, 1S.

[9] N. Lang, M. J. Pereira, Y. Lee, I. Friehs, N. V. Vasilyev, E. N. Feins, K. Ablasser, E. D. O'Cearbhaill, C. Xu, A. Fabozzo, R. Padera, S. Wasserman, F. Freudenthal, L. S. Ferreira, R. Langer, J. M. Karp, P. J. del Nido, *Sci. Transl. Med.* **2014**, *6*, 218ra6.

[10] D.-A. Wang, S. Varghese, B. Sharma, I. Strehin, S. Fermanian, J. Gorham, D. H. Fairbrother, B. Cascio, J. H. Elisseeff, *Nature Mater.* **2007**, *6*, 385.

[11] R. L. Galloway, *Annu. Rev. Biomed. Eng.* **2001**, *3*, 83.

[12] M. R. Patel, W. Louie, J. Rachlin, *Am. J. Neuroradiol.* **1996**, *17*, 495.

[13] H. Iwase, O. Maeda, M. Shimada, T. Tsuzuki, R. M. Peek, Y. Nishio, T. Ando, K. Ina, K. Kusugami, *Gastrointest. Endosc.* **2001**, *53*, 585.

[14] M. R. Button, J. N. Staffurth, *Clin. Oncol.* **2010**, *22*, 698.

[15] J. S. Rydhog, S. R. Mortensen, K. R. Larsen, P. Clementsen, R. I. Jolck, M. Josipovic, M. C. Aznar, L. Specht, T. L. Andresen, P. M. af Rosenschold, G. F. Persson, *Radiother. Oncol.* **2016**, *121*, 64.

[16] N. Annabi, S. R. Shin, A. Tamayol, M. Miscuglio, M. A. Bakooshli, A. Assmann, P. Mostafalu, J.-Y. Sun, S. Mithieux, L. Cheung, X. S. Tang, A. S. Weiss, A. Khademhosseini, *Adv. Mater.* **2016**, *28*, 40.

[17] D. E. Fullenkamp, J. G. Rivera, Y.-K. Gong, K. H. A. Lau, L. He, R. Varshney, P. B. Messersmith, *Biomaterials* **2012**, *33*, 3783.

[18] T. Dvir, B. P. Timko, M. D. Brigham, S. R. Naik, S. S. Karajanagi, O. Levy, H. Jin, K. K. Parker, R. Langer, D. S. Kohane, *Nature Nanotech.* **2011**, *6*, 720.

[19] S. Rose, A. Prevoteau, P. Elziere, D. Hourdet, A. Marcellan, L. Leibler,

Nature **2014**, *505*, 382.

[20] A. Meddahi-Pelle, A. Legrand, A. Marcellan, L. Louedec, D. Letourneur, L. Leibler, *Angew. Chem. Int. Ed.* **2014**, *53*, 6369.

[21] J. Kim, Y. Piao, T. Hyeon, *Chem. Soc. Rev.* **2009**, *38*, 372.

[22] J. Gao, H. Gu, B. Xu, *Acc. Chem. Res.* **2009**, *42*, 1097.

[23] J. L. Vivero-Escoto, R. C. Huxford-Phillips, W. Lin, *Chem. Soc. Rev.* **2012**, *41*, 2673.

[24] N. Lee, D. Yoo, D. Ling, M. H. Cho, T. Hyeon, J. Cheon, *Chem. Rev.* **2015**, *115*, 10637.

[25] G. Chen, H. Qiu, P. N. Prasad, X. Chen, *Chem. Rev.* **2014**, *114*, 5161.

[26] J. Della Rocca, D. Liu, W. Lin, *Acc. Chem. Res.* **2011**, *44*, 957.

[27] E. Phillips, O. Penate-Medina, P. B. Zanzonico, R. D. Carvajal, P. Mohan, Y. Ye, J. Humm, M. Gönen, H. Kalaigian, H. Schöder, H. W. Strauss, S. M. Larson, U. Wiesner, M. S. Bradbury, *Sci. Transl. Med.* **2014**, *6*, 260ra149.

[28] J. V. Jokerst, S. S. Gambhir, *Acc. Chem. Res.* **2011**, *44*, 1050.

[29] Q. Xiao, W. Bu, Q. Ren, S. Zhang, H. Xing, F. Chen, M. Li, X. Zheng, Y. Hua, L. Zhou, W. Peng, H. Qu, Z. Wang, K. Zhao, J. Shi, *Biomaterials* **2012**, *33*, 7530.

[30] H. Lusic, M. W. Grinstaff, *Chem. Rev.* **2013**, *113*, 1641.

[31] N. Lee, S. H. Choi, T. Hyeon, *Adv. Mater.* **2013**, *25*, 2641.

[32] Y.-W. Jun, J.-H. Lee, J. Cheon, *Angew. Chem. Int. Ed.* **2008**, *47*, 5122.

[33] J. Gao, G. Liang, J. S. Cheung, Y. Pan, Y. Kuang, F. Zhao, B. Zhang, X. Zhang, E. X. Wu, B. Xu, *J. Am. Chem. Soc.* **2008**, *130*, 11828.

[34] Z. Liu, W. Cai, L. He, N. Nakayama, K. Chen, X. Sun, X. Chen, H. Dai, *Nature Nanotech.* **2007**, *2*, 47.

[35] J. Xie, G. Liu, H. S. Eden, H. Ai, X. Chen, *Acc. Chem. Res.* **2011**, *44*, 883.

[36] D. C. Niu, X. Wang, Y. S. Li, Y. Y. Zheng, F. Q. Li, H. R. Chen, J. L. Gu, W. R. Zhao, J. L. Shi, *Adv. Mater.* **2013**, *25*, 2686.

[37] D. Ni, W. Bu, S. Zhang, X. Zheng, M. Li, H. Xing, Q. Xiao, Y. Liu, Y. Hua, L. Zhou, W. Peng, K. Zhao, J. Shi, *Adv. Funct. Mater.* **2014**, *24*, 6613.

[38] H. Lee, Y. Lee, C. Song, H. R. Cho, R. Ghaffari, T. K. Choi, K. H. Kim, Y. B. Lee, D. Ling, H. Lee, S. J. Yu, S. H. Choi, T. Hyeon, D.-H. Kim, *Nat. Commun.* **2015**, *6*, 10059.

[39] M. F. Kircher, A. de la Zerda, J. V. Jokerst, C. L. Zavaleta, P. J. Kempen, E. Mittra, K. Pitter, R. Huang, C. Campos, F. Habte, R. Sinclair, C. W. Brennan, I. K. Mellinghoff, E. C. Holland, S. S. Gambhir, *Nat. Med.* **2012**, *18*, 829.

[40] H. Xing, W. Bu, S. Zhang, X. Zheng, M. Li, F. Chen, Q. He, L. Zhou, W. Peng, Y. Hua, J. Shi, *Biomaterials* **2012**, *33*, 1079.

[41] M. H. Oh, N. Lee, H. Kim, S. P. Park, Y. Piao, J. Lee, S. W. Jun, W. K. Moon, S. H. Choi, T. Hyeon, *J. Am. Chem. Soc.* **2011**, *133*, 5508.

[42] Y. S. Jin, X. B. Ma, S. S. Feng, X. Liang, Z. F. Dai, J. Tian, X. L. Yue, *Bioconjug. Chem.* **2015**, *26*, 2530.

[43] Y. S. Jin, Y. Y. Li, X. B. Ma, Z. B. Zha, L. L. Shi, J. Tian, Z. F. Dai, *Biomaterials* **2014**, *35*, 5795.

[44] A. S. Torres, P. J. Bonitatibus, R. E. Colborn, G. D. Goddard, P. F. FitzGerald, B. D. Lee, M. E. Marino, *Invest. Radiol.* **2012**, *47*, 578.

[45] N. Lee, H. R. Cho, M. H. Oh, S. H. Lee, K. Kim, B. H. Kim, K. Shin, T. Y. Ahn, J. W. Choi, Y. W. Kim, S. H. Choi, T. Hyeon, *J. Am. Chem. Soc.* **2012**, *134*, 10309.

[46] P. J. Bonitatibus, A. S. Torres, G. D. Goddard, P. F. FitzGerald, A. M. Kulkarni, *Chem. Comm.* **2010**, *46*, 8956.

[47] A. Jakhmola, N. Anton, T. F. Vandamme, *Adv. Healthcare Mater.* **2012**, *1*, 413.

[48] J. D. Freedman, H. Lusic, B. D. Snyder, M. W. Grinstaff, *Angew. Chem. Int. Ed.* **2014**, *53*, 8406.

[49] Q. He, J. Shi, M. Zhu, Y. Chen, F. Chen, *Microporous Mesoporous*

Mater. **2010**, *131*, 314.

[50] H. Lee, W. S. Lee, J. I. Park, K.-J. Son, M. Park, Y.-b. Bang, Y. B. Choy, S.-J. Ye, *Med. Phys.* **2015**, *42*, 2805.

[51] A. E. Nel, L. Madler, D. Velegol, T. Xia, E. M. V. Hoek, P. Somasundaran, F. Klaessig, V. Castranova, M. Thompson, *Nature Mater.* **2009**, *8*, 543.

[52] B. B. Goldberg, J.-B. Liu, F. Forsberg, *Ultrasound Med. Biol.* **1994**, *20*, 319.

[53] G. Ciapetti, S. Stea, E. Cenni, A. Sudanese, D. Marraro, A. Toni, A. Pizzoferrato, *Biomaterials* **1994**, *15*, 63.

[54] D. M. Toriumi, W. F. Raslan, M. Friedman, M. E. Tardy, *Arch. Otolaryngol. Head Neck Surg.* **1990**, *116*, 546.

[55] M. S. Bradbury, E. Phillips, P. H. Montero, S. M. Cheal, H. Stambuk, J. C. Durack, C. T. Sofocleous, R. J. C. Meester, U. Wiesner, S. Patel, *Integr. Biol.* **2013**, *5*, 74.

[56] J. Black, *Clin. Mater.* **1994**, *16*, 167.

[57] Y.-S. Lin, C. L. Haynes, *J. Am. Chem. Soc.* **2010**, *132*, 4834.

[58] Y. Zhao, X. Sun, G. Zhang, B. G. Trewyn, I. I. Slowing, V. S. Y. Lin, *ACS Nano* **2011**, *5*, 1366.

[59] M. R. Moman, U. A. van der Heide, A. N. T. J. Kotte, R. J. A. van

Moorselaar, G. H. Bol, S. P. G. Franken, M. van Vulpen, *Radiother. Oncol.* **2010**, *96*, 38.

[60] D. Habermehl, K. Henkner, S. Ecker, O. Jakel, J. Debus, S. E. Combs, *J. Radiat. Res.* **2013**, *54*, i61.

[61] A. L. Vahrmeijer, M. Hutteman, J. R. van der Vorst, C. J. H. van de Velde, J. V. Frangioni, *Nat. Rev. Clin. Oncol.* **2013**, *10*, 507.

[62] N. Bhagat, N. Fidelman, J. C. Durack, J. Collins, R. L. Gordon, J. M. LaBerge, R. K. J. Kerlan, *Cardiovasc. Intervent. Radiol.* **2010**, *33*, 1186.

[63] Y. D. Kim, Y. J. Jeong, H. I, J. S. Cho, J. W. Lee, H. J. Kim, S. H. Lee, D. H. Kim, *Acta Radiol.* **2011**, *52*, 64.

Chapter 3. Imaging and drug delivery assisting cell therapy with nanoparticle attachment onto cell surface

3.1 Introduction

Cell-based therapies involving transplantation and direct injection have provided a prospective solution for the treatment of congenital defects and damaged tissues.[1,2] However, declines in survival rate and therapeutic effect of administered cells due to host immune rejection substantially limit the extensive application of cell-based therapy, so a suitable method is required to track/monitor the administered cells to evaluate the efficacy of cell therapy. Hence, incorporating biomaterials/nanomaterials to cells has been spotlighted in cell-based therapies as a strategy to provide therapeutic cells with a protective layer or to tag them with imaging probes.[3-15] In addition, incorporating drug-loaded nanoparticles are expected to enhance the efficiency of drug delivery because of their active targeting capability.[16-19]

One of the main approaches for the incorporation of exogenous materials is cell surface modification via chemical conjugation to functional groups existing on the cell membrane.[5,19-24] Compared to other cell surface engineering methods, this approach enables direct engraftment of various materials, and guarantees their stable attachment to cells when they are implanted into the complex biological environment. The conjugation based surface engineering can modify individual cells uniformly and stabilize them without aggregation, unlike electrostatically driven cell coating.[4,9] Because the approach does not involve hydrophobic interaction, it broadens the selection of the material without compromising the solubility and stability of the exogenous materials.[25] Based on the well-established bioconjugation techniques, the procedure is generally accessible without additional preparation steps or special equipment such as microfluidic channels.[15]

Despite the advantages of conjugation-based modification, the introduction of active functional groups on the cell surface remains challenging because most cell surfaces do not contain chemically reactive moieties.[26] Although amide coupling can be employed for cell surface modificaion[27-29], cross-coupling between carboxylate and amine groups potentially decreases both efficiency and specificity of the

reaction between coating materials and cell surface. There are some reported methods to introduce non-natural functional groups such as ketone and azide on mammalian cell surfaces via glycoengineering.[30-32] These are time-consuming, taking several days for cells to express them and confirming their expression.

Herein, we report a facile and universal method for cell surface engineering that exploits disulfide bonds on cell membranes[33] for subsequent thiol-maleimide conjugation. A variety of cell types can be coated without any adverse effects on cell functions. This method can coat biomolecules and polymers to demonstrate rapid formation of multicellular assembly and facilitation of cell adhesion to a polymeric scaffold. Fluorescent multifunctional nanoparticles can be attached to cell surface for tracking the administered cells and delivering adjuvant drugs simultaneously. Finally, synergistical enhancement of cellular activity is achieved through a dual coating of polymer and nanoparticles.

3.2 Experimental Section

3.2.1 Cell culture and preparation

HeLa, Jurkat, C2C12, and neuro-2A cells were purchased from the Korean Cell Line Bank (Korea). All cells, except induced neuronal stem cells, were cultured in tissue-culture plates with high-glucose Dulbecco's modified Eagle's medium (DMEM; Gibco-BRL, USA) containing 10% fetal bovine serum (FBS; Gibco-BRL), 1% L-glutamine (200 mM, Gibco-BRL), and 1% penicillin-streptomycin (10,000 U/ml of penicillin and 10,000 g/ml of streptomycin, Gibco-BRL). When the cells reached 80% confluency, they were washed twice with phosphate-buffered saline (PBS; pH 7.4, Gibco-BRL). For experiments using detached cells, trypsin-ethylenediaminetetraacetic acid (EDTA) solution (0.25% trypsin, 380 mg/L EDTA-4Na·2H_2O; Gibco-BRL) was added to the culture plate, which was then incubated at 37 °C for 3 min. After the cells were detached from the plate, DMEM was added for neutralization. The cells were collected by centrifugation (266 x g for 5 min) and washed twice with PBS.

3.2.2 Reduction disulfide bonds of proteins on cellular surface

Cells at a density of 2×10^6 cells/ml were collected in 1.7-ml tubes by centrifugation at 300 gravitational force and suspended in 1 ml of PBS containing 0.5, 1, 2, or 3 mM of Tris(2-chloroethyl) phosphate (TCEP , Sigma-Aldrich, USA). Then the samples were incubated at 37 °C for 20 min. After incubation, the cells were washed with PBS twice. For the certification of free thiols, Ellman's assay (5,5-dithio-bis-(2-nitrobenzoic acid), Thermo, USA) was performed following the manufacturer's procedure. The cell viability was measured by Live/Dead® viability/cytotoxicity kit (Thermo) that contains calcein-AM and ethidium homodimer solution. After treatment of TCEP for 20 min on cells, Live/Dead assay were used to indicate live cells and dead cells. Then the cells were imaged by fluorescence microscopy (EVOS® Cell Imaging Systems, Thermo) and counted in separate 5 fields. For proliferation, cells were stained using the ClickiT ® EdU Alexa Fluor® 488 Imaging Kit (Thermo). Prior to EDU assay, cells were cultured overnight in serum free media for the synchronization of cell growth. After synchronization, cells were treated with reductant and incubated in EDU containing growth media for 3 hrs. Then, EDU assay kit was applied to indicate cells in S phase and analyzed by flow cytometry. To

assess cell metabolism, cells were incubated with the growth media containing the alamarBlue® Cell Viability Reagent (Thermo). The relative absorbance difference was measured on same time each day. For morphological analysis, cells were fixed with 4% paraformaldehyde (Sigma-Aldrich) for 10 min and permeabilized with Triton X-100 (Sigma-Aldrich) for 10 min. Fixed cells were stained with DAPI (Thermo) for 10 min and Alexa Fluor® 594 Phalloidin (1:200 dilution, Thermo) for 2 hrs.

3.2.3 Maleimide Alexa Fluor 488 (MFluor) Coating

After TCEP treatment, HeLa cells were washed with PBS twice. Then, Alexa Fluor® 488 C5 Maleimide (MFluor; 1 mg/ml, Thermo) was diluted in PBS solution (final concentration: 3 μg/ml) and added to the cells, which were then incubated for 20 min in an incubator at 37 °C. During incubation, the tubes were tapped every 5 min. After 20 min, the cells were washed with PBS twice and analyzed by confocal microscopy (LSM 780; Carl Zeiss) and flow cytometry (FACS Aria II; BD Biosciences, USA). For confirmation of surface coating, the PKH26 Red Fluorescent Cell Linker Kit (PKH26; Sigma-Aldrich) was used. For flow

cytometric analysis, a fluorescein isothiocyanate (FITC) standard signal was set.

3.2.4 Pre-conjugation of dye-silane derivatives

Fluorescent dye-silane derivatives were prepared in advance by conjugation of (3-aminopropyl)triethoxysilane (APTES, Sigma-Aldrich) and fluorescent dyes, including FITC(Sigma-Aldrich), cyanine 5 NHS ester (Cy5; Lumiprobe), and cyanine 5.5 NHS ester (Cy5.5; Lumiprobe). Each dye with fucntional group was dissolved in ethanol at 3 mM concentration with APTES at 15 mM. The mixture was shaken at room temperature overnight.

3.2.5 Preperation of fluorescent mesoporous silica nanoparticles

Uniform MSN were synthesized as previously reported[4] with slight modification. Two grams of hexadecyl trimethyl ammonium chloride (cetyltrimethylammonium chloride solution 25%, 8 ml, Sigma-Aldrich) and 80 mg of triethanolamine were disolved in 20 ml of distilled water. After the solution was heated at 95 °C for 1 h, 1.5 ml of tetraethyl orthosilicate (Acros Organics) was added dropwise. To prepare

fluorescently labeled mesoporous silica nanoparticle (MSN), the pre-conjugated dye-silane derivatives were subsequently added. Reactions were proceeded for 50 min, resulting in turbid solutions, and 50 mg of APTES was added and reacted for 10 min for amino-functionalization of the MSN. The products were collected by centrifugation and re-dispersed with ethanol several times. For extraction of residual surfactant in MSN, the products were dispersed and stirred in 1 wt% of NaCl in methanol at 60 °C for 3 h, and the same extraction process was repeated twice. The final products were dispersed in ethanol at 10 mg/ml.

3.2.6 PEGylation of amino-fucntionalized MSN for cell coating

Maleimide-PEG 5k succinimidyl NHS acid ester (Mal-PEG5k-SCM), and methoxy-PEG5k succinimidyl glutarate ester (mPEG5k-SG) were purchased from Creative PEGworks and SunBio, respectively. PEG derivatives were pre-dissolved in dimethylformaldehyde at 100 mg/ml. For maleimide-fucntionalized MSN (Mal-MSN), 15 mg of MSN dispersed in ethanol, 10 mg of mPEG-SG, and 5 mg of Mal-PEG-5k-SCM was mixed and shaken at room temperature overnight. After the conjugation, residual PEG was washed away by centrifugation and the products were redispersed in PBS. MSN without fucntional group was

prepared using the same method, except that 15 mg of mPEG-SG was used.

3.2.7 Characterization of MSN

Transmission electron microscopic (TEM) images were obtained with an EM-2010F (Jeol, Japapn). Hydrodynamic radius was analyzed with a size analyzer (Nanozs). The absorption and emission spectra of the fluorescently labeled MSN was measured with SpectroV-550 and FP-5500 instruments (both Jasco, Japan).

3.2.8 Attachment of the MSN to mammalian cells

After mild reduction of the cell surface with TCEP at 0.75 mM, the cell suspension was washed several times with PBS and incubated in 5 mg/ml of Mal-MSN solution for 20 min. Subsequently, mPEG2k-SH (methoxy PEG2k-thiol) dissolved in PBS was added to the suspention at a concentration of 1 mg/ml, and incubated for 10 min to deactivate the maleimide groups on the nanoparticles. The MSN-coated cells were seperated from residual nanoparticles by centrifugation and then washed with PBS several times. Depending on the imaging device, FITC-, Cy5-, or Cy5.5-labeled MSN was used. For dual-coating with MSN and PEG,

5 mg/ml of mPEG 2 kDa maleimide dissolved in PBS was introduced to the MSN coated-cell suspension. The confocal microscope image were obtained using LSM 780 and Cy5 conjugated MSN. The fluorescence signal difference of cells was measured by flow cytometry by using FITC conjugated MSN (BD Accuri^{TM} C6 Plus Cytometer System; BD Biosciences).

3.2.9 Drug or fluorescent dye loading into MSNs and their characterization

One milligram of rhodamine 123, fluorecein or dexamethasone 21-phosphate disoldium salt dissolved in PBS was added to 5 mg of PEGylated MSN and shaken at room temperature for overnight. Excessive rhodamine or dexamethasone was washed by centrifugation and the final product was dispersed in PBS. The fluorecent dye (rhodamine 123 or fluorecein) loaded MSN was also analyzed with fluorescence correlation spectroscopy equiped on confocal microscopy (Zeiss LSM 780 NLO, Zeiss, Germany) and applied to coat HeLa cell with the same used methode, to confirm the surface modification. The coated cells were also visualized with the confocal microscope. The functionalized MSN was transferred into a 1-kDa dialysis tube and stored

in 40 ml of PBS to analyze its release profile. The permitted small molecules were analyzed by spectrophotometry using a Spectro V-550 or a Victor X4 microplate reader (Perkin-Elmer, USA).

3.2.10 Electron microscopic imaging of coated cells

Electron microscopy samples were prepared by fixation and dehydration. Coated Hela cells were fixed with 2.5% of glutaraldehyde and 2% of paraformaldehyde in 0.1 M of sodium cacodylate buffer (pH 7.4), then rinsed with cacodylate buffer. Additional fixation was carried out with 1% osmium tetraoxide in cacodylate buffer. After washing away the residual fixation reagent with distilled water three times, cells were stained overnight with 2% uranyl acetate solution. Dehydration was done gradually by incubating the stained cells for 10 min in each of 30%, 50%, 70%, 80%, 90% ethanol, absolute ethanol, and propylene oxide. The dehydrated cells were suspended in 50% Spurr's resin with propylene oxide for 2 h, and in Spurr's resin overnight. After fresh Spurr's resin was added to the cell suspension, the resin was hardened in oven at 60 °C for 24 h. The embedded cells were sliced with an ultramicrotome (EM UC7; Leica, Germany). TEM images were obtained with JEM1010 (Jeol, Japan).

3.2.11 Evaluation on accessibility to cellular membrane after surface modification

After the surface modification of HeLa or RAW264.7 cells, the cells were washed four times with PBS. The cells were stained with CellMask, CD44-antibody, or CD11b with appropriate condition. The control group or surface-modified group were incubated for 10 min at 4 °C with CellMask (for HeLa cell, 1:2000, Thermo Fisher Scientific), for 30 min at 37 °C with anti-human CD44 (for HeLa cell, 1:200, BD Pharmigen), at 4 °C with FITC anti-mouse/human CD11b Antibody (for RAW 264.7 cell, 1:2000, BioLegend). To the CD44 antibody, fluorescent secondary antibody (FITC Goat anti-Mouse IgG (1:1000, Bethyl Lab. Inc.)) was treated for 30min at 37 °C. Prior to imaging or flow cytometry analysis, residual fluorescent antibody or CellMask were removed by washing four times with PBS. The cells were re-suspended in PBS for flow cytometry (BD Accuri^{TM} C6 Plus Cytometer System; BD Biosciences, BD Biosciences, USA). The corresponding fluorescence images were acquired using a Zeiss LSM 780 NLO inverted laser scanning confocal microscope (Zeiss, Germany).

3.2.12 Animals and Cells

In this study, we used male BALB/c nude and Crl:CD-1 (ICR) mice weighing 28–30 g (Orient, Seoul, Korea). The animals were maintained at 22–24 °C under a 12-h/12-h light/dark cycle. The mice were given at least 1 week to adapt to their environment prior to experiments. The Institutional Animal care and Use Committee at the Korea Basic Science Institute (KBSI-AEC 1601) reviewed and approved this study. All animal procedures were in accordance with the Guide for the Care and Use of Laboratory Animals issued by the Laboratory Animal Resources Commission of KBSI. HeLa-Luc (Xenogen) human cervical adenocarcinoma cancer cells were grown at 37 °C in DMEM (Lonza) containing 10% (v/v) FBS (Gibco-BRL).

3.2.13 Intra-vital imaging

For the implantation of a dorsal skin-fold chamber into mouse, two plastic frames were implanted into extended double layers of skin. One layer of the skin was removed in a circular area of approximately 13 mm

in diameter. One milligram of rhodamine 123 were loaded to 5 mg of PEGylated MSN and the excess rhodamine dye were removed by washing procedure with PBS. One million of Hela cells were coated with rhodamine 123 loaded MSN using the same method described above. About 20 μl of rhodamine loaded MNP-coated HeLa cells (1×10^4) prepared was implanted at the center of the remaining layer (epidermis, subcutaneous tissue, and muscle). A cover glass (12 mm) was then placed on the chamber. Dorsal skin-fold chambers were observed under an intravital microscope (LSM 780 NLO; Carl Zeiss, Germany, KBSI Chuncheon Center, Korea).

3.2.14 In vivo imaging system

The in vivo fluorescence imaging to track the location of cells was obtained by whole body imaging system using Cy5.5 conjugated MSN coated HeLa-Luc cells. The cells were reduced by 0.75 mM TCEP and incubated in 5 mg/ml of Cy5.5 conjugated Mal-MSN solution for 20 min. About 1×10^6 HeLa-Luc cells were injected subcutaneously in each group. The fluorescence and luminescence were imaged by IVIS200 system (Xenogen Corporation, Alameda, CA, USA) for 0-8 days.

3.2.15 Implanting cells with drug delivery vehicle and protective polymer

The protection and immunosuppression with polymer/nanoparticle coating were evaluated with monitoring subcutaneous injected coated cells. For polymer coating, cells were reduced by 1 mM TCEP and treated with 10% (w/v) maleimide-PEG (JenKem Technology, TX, USA) solution for 20 min and washed for several times. For MSN coating, after mild reduction of the cell surface with TCEP at 0.75 mM, the cell suspension was washed for several times with PBS and incubated in 5 mg/ml of (dexamethasone)-loaded Mal-MSN solution for 20 min. Dual-coating of cells was conducted with the mixture of 10% (w/v) maleimide-PEG and 5 mg/ml of (dexamethasone)-loaded Mal-MSN solution for 20 min after 0.75 mM TCEP reduction. For the subcutaneous primary tumor model, mice were anesthetized by exposure to 2–2.5% isoflurane, and 100 μl sterile Dulbecco's phosphate-buffered saline containing 1×10^7 HeLa-Luc cells was injected into the back of each mouse. To check viability of the Hela-Luc, luciferin was dissolved in PBS (30 mg/ml) and 150 μl of the luciferin solution was intraperitoneally

injected. Cellular activities were monitored on the IVIS200 system for 0–7 days, and the regions of interest were quantified with photon flux (p/s) using Living Imaging software v4.2 (Xenogen Corporation).

3.3 Result and Discussion

3.3.1 Activation of thiol group on cellular surface

Scheme 3.1 describes the surface modification method that consists of mild reduction of disulfides on cell surfaces with tris(2-carboxyethyl)phosphine (TCEP) and subsequent thiol-maleimide conjugation. TCEP is nonvolatile and stable in aqueous solution at room temperature over a wide range of pH, and resistant to air oxidation.[34] It can selectively reduce disulfide bonds, but are essentially unreactive towards other functional groups in proteins.[35] Compared to other reducing agents such as dithiothreitol and 2- mercaptoethanol, TCEP does not react with active maleimide groups, retaining the efficiency of cell surface modification.

Fluorescent dye with a maleimide functional group (MFluor) was utilized to evaluate the coating method (**Figure 3.1**). Fluorescence signals were distributed evenly over the cell surfaces without any evidence of internalization. When the cells were post-labeled with a membrane dye (PKH-26), MFluor signals co-localized with those of PKH-26, confirming that the conjugation takes place solely on the cell surface. Dose-dependent effects of TCEP on HeLa cells were evaluated

by flow-cytometric analysis. The reduction reaction dramatically increased the fluorescence of attached MFluor on the cells, which was saturated after treatment with 1 mM TCEP (**Figure 3.2**). In quantitative analysis, the ratio of the amount of MFluor to cellular surface area is nearly identical in attached or detached state, indicating that the conjugation evenly occurs regardless of the cellular morphology. (**Figures 3.1a and 3.3**). Most importantly, no adverse effect on cellular morphology, viability, proliferation, and metabolism was observed for TCEP concentrations equal or below 1 mM (**Figure 3.4**), and the reduced thiols are recovered in a single day (**Figure 3.5**). Thus, 1 mM of TCEP was designated as the optimal concentration for cell surface reduction.

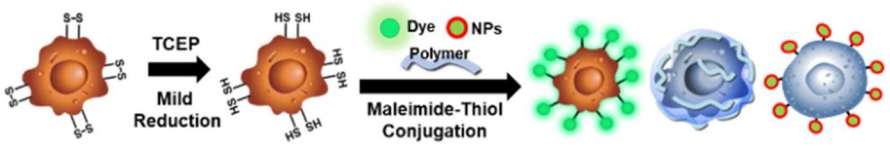

Scheme 3.1 Cell surface modification with fluorescent dye, polymer, and nanoparticles by mild reduction using TCEP.

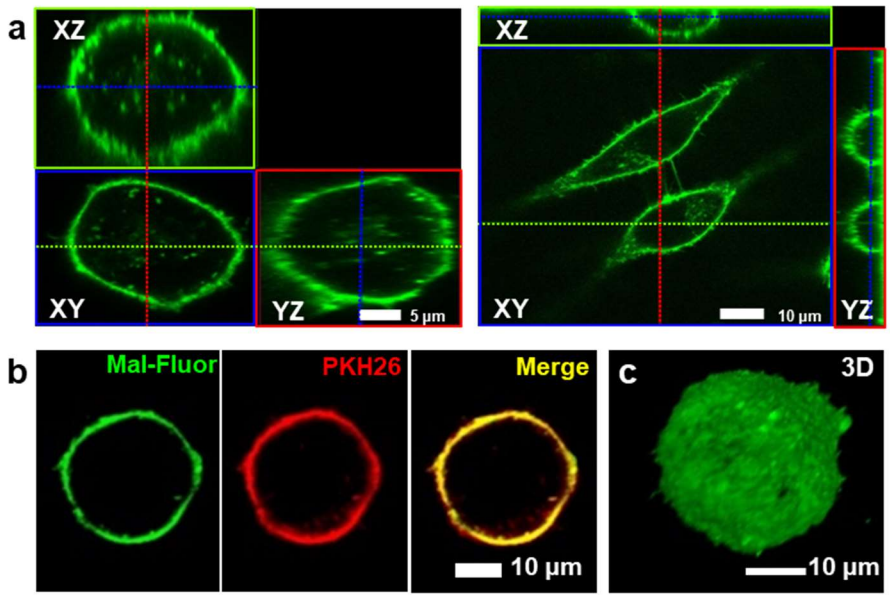

Figure 3.1. Confocal image of Hela cell decorated with MFluor (a) 2D orthogonal plane images of detached (left panel) and attached (right panel) MFluor-coated HeLa cells obtained by confocal microscopy. (b) Confocal microscopic image of cell surface modified with MFluor and PKH26-labeled HeLa cells. (c) 3D-rendered image of MFluor-coated HeLa cells.

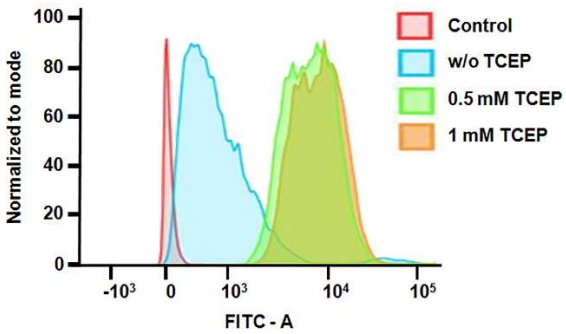

Figure 3.2. Flow-cytometric analysis for comparison of MFluor attachment to HeLa cell depending on the concentration of reductant. Control group represents the cells without any treatment including the MFluor. Without TCEP group represents the cells only treated with MFluor.

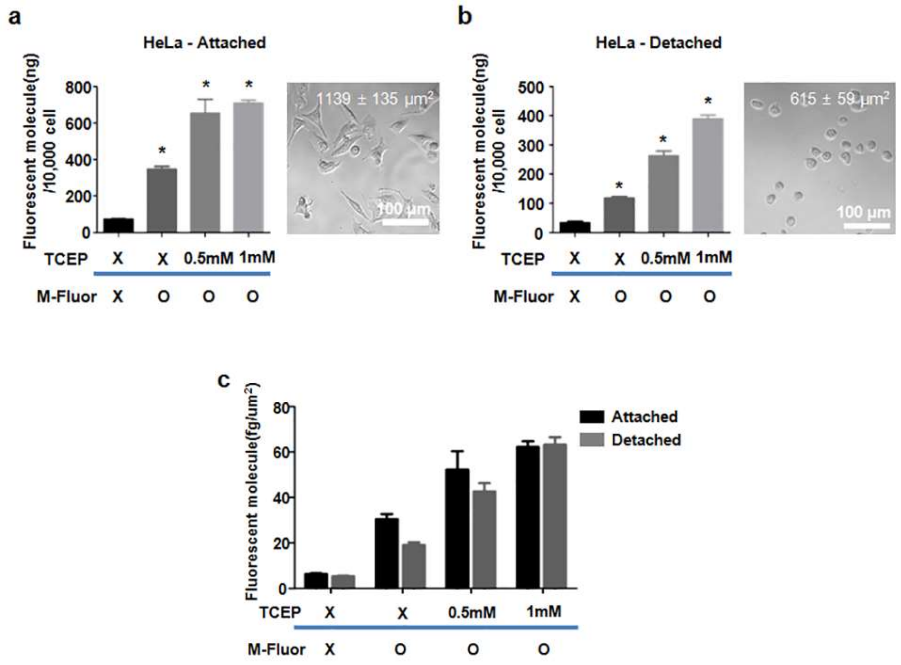

Figure 3.3 Quantification of cell surface reduction by concentration dependent reduction and MFluor coating. a) Analysis plot and the representative image of attached HeLa cells. b) Analysis plot and the representative image of detached HeLa cells. c) Analysis plot of attached and detached HeLa cells normalized by the single cell surface area. (*p < 0.05 vs. non-treated group, n = 5 in (a) and (b), average surface area of attached and detached cells are represented at the edge of (a) and (b)).

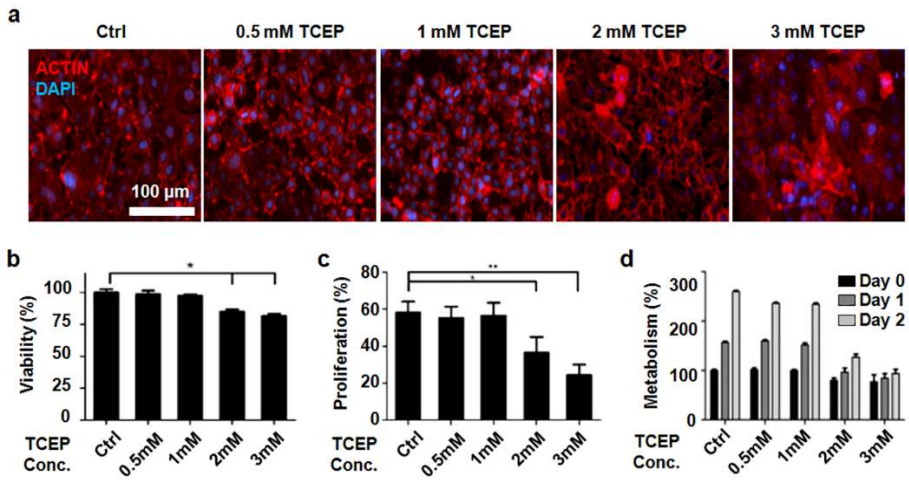

Figure 3.4 Evaluation of cytotoxicity depending on the concentration of reductant. a) Fluorescence images stained with F-actin (red) DAPI (blue) for the cellular morphology analysis depending on the reductant treatment. b) Plot of Live/Dead assay for cell viability measurement. c) Proliferation rate measurement by EDU assay after synchronizing cell growth before reduction. d) Cell metabolism measurement by alamarBlue assay (*$p < 0.05$ vs. non-treated group, **$p < 0.01$ vs. non-treated group, n = 3 in b-d).

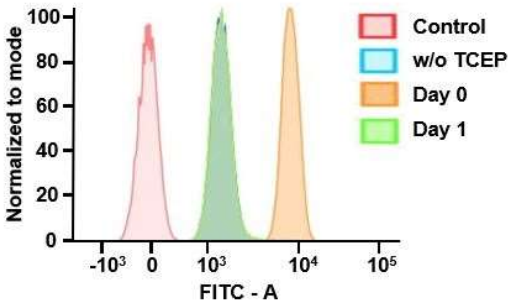

Figure 3.5 Flow-cytometric analysis onthe recovery of reduced thiols on the reduced cells. Control group represents the cells without any treatment including the MFluor. Without TCEP group represents the cells only treated with MFluor. Day 0 represents cells coated with MFluor right after 1 mM TCEP reduction. Day 1 represents cells coated with MFluor for a day after 1 mM TCEP reduction.

3.3.2 Nanoparticle attachment to cellular membrane

Nanoparticles have been employed in a wide range of biomedical applications, such as bioimaging and delivery of therapeutic cargo.[19,36-39] In this study, we functionalized cells by coating with nanoparticles for tracking, imaging, and localized drug delivery. As one of the representative nanomaterial candidates, we chose fluorescent mesoporous silica nanoparticles (MSNs) because of their facile surface modification, high drug-loading capability, and good biocompatibility.[3,40-42] Maleimide-conjugated MSNs were prepared and conjugated to the surface-reduced cells (**Figures 3.6**). The nanoparticles were aligned around the cell surface (**Figures 3.7**). As shown by the flow cytometry, a significant number of nanoparticles was attached to the surface-reduced cells (**Figures 3.8**). Compared to non-specific adsorption of nanoparticles to the cell surface, the MSNs covalently bound to the cells, thus providing sufficient stability to endure multiple washing steps (**Figures 3.9**).

To investigate whether surface receptors are blocked or sterically hindered after the surface modification, we examined the surface accessibility and ligand exposure before and after surface modification in HeLa cell and RAW 264.7 macrophage cell. First, Cellmask-orange

which can target most of lectins on cell surface was used. After cell surface modifications including reduction (TCEP treatment), nanoparticle coating (mesoporous silica attachment), polymer coating (maleimide PEG coating), and nanoparticle/polymer dual coating, we analyzed the cells with flow cytometry and confocal imaging. The little changes of fluorescence intensity and conformal coating of cell mask suggest that the surface lectins of coated cells can be accessible to Cellmask and confirm that blocking by the coating material is also negligible (**Figure 3.10**).

Furthermore, we examined the effect on glycoprotein or protein of the TCEP-mediated reduction and cell surface modification. The CD44 antigen, a glycoprotein ubiquitously expressed on the surface of various human cells including HeLa cell, plays an important role in cell adhesion and cell-cell interaction. With CD44 antibody and its FITC conjugated secondary antibody, we could evaluate the expression level of CD44 on the HeLa cells. After the cell surface modification including reduction of disulfides and coating with nanoparticles, polymers or both, the CD44 antibody can still anchor on the HeLa cell surfaces, which was confirmed by flow cytometry analysis (**Figure 3.11**). Another experiment was also conducted with macrophage cell line, RAW264.7,

which expresses CD11b (known as integrin alpha M) on the surface. We could obtain macrophage cells modified with polymer/nanoparticles and confirm the presence of the specific interaction between the CD11b antibody and macrophage cell surface (**Figure 3.12**). After the MSN-coating, the viability or metabolism were retained. (**Figure 3.13)** The coated nanoparticles were distributed on cell surface for 9 hours *in vitro* (**Figure 3.14**), and taken up by the cells via endocytosis.

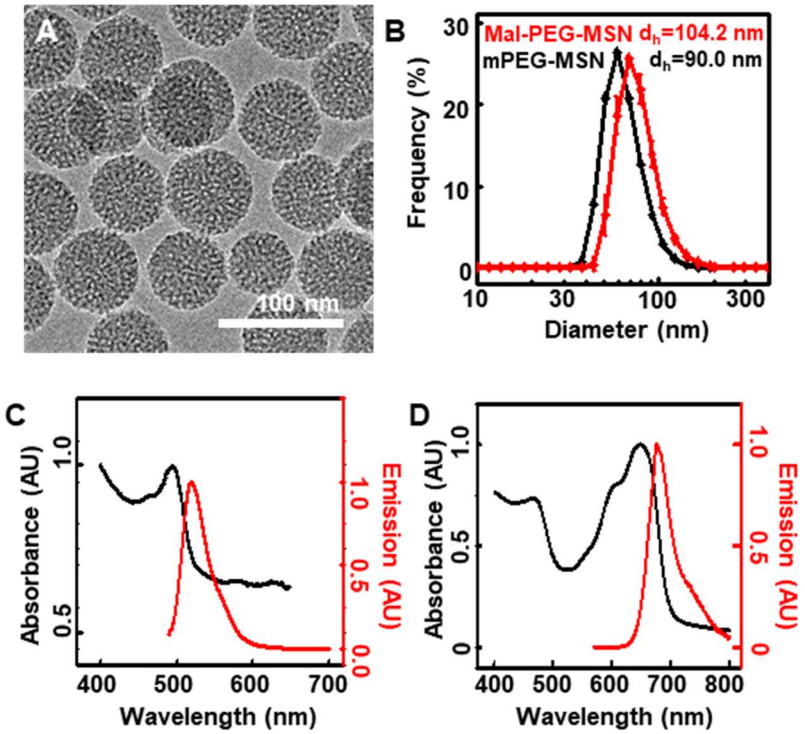

Figure 3.6. Characterization of mesoporous silica nanoparticles (MSN) with maleimide functional moieties. a) TEM image of MSN. b) Distribution of hydrodynamic diameters of PEGylated nanoparticles with maleimide functional moieties (Mal-PEG-MSN) and without maleimide moieties (mPEG-MSN). Average diameters presented in the upper-left side of the plot. c,d) Absorption and emission spectra of FITC-conjugated MSN (c) and Cy5-conjugated MSN (d).

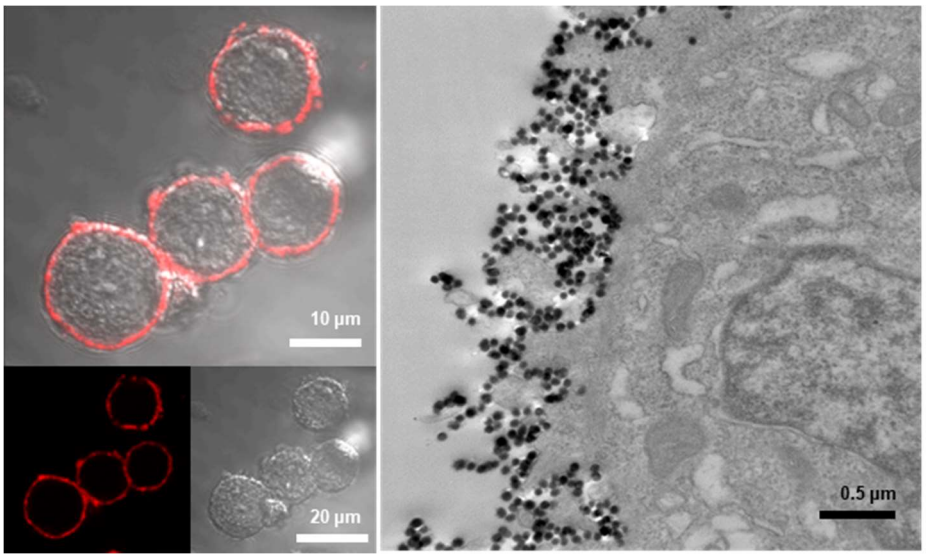

Figure 3.7. Cell surface modification with nanoparticles Confocal image of cells coated with fluorescent MSNs (left). Transmission electron microscopic image of MSNs attached on the cell surface (right).

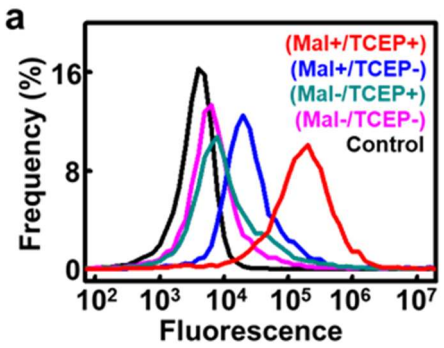

Figure 3.8. Flow-cytometric analysis of nanoparticle attachment onto the cell membrane with mild reduction and conjugation for evaluating efficiency and rigidity of the attachment. MSN attachment depending on the functional moiety on MSN and TCEP treatment. Both TCEP treatment and the existence of maleimide functional groups (Mal+/TCEP+; red) enable efficient attachment of MSN to the cells. In the absence of TCEP treatment (Mal+/TCEP-; blue), fluorescent signal is lower than in the treated group. Without maleimide moieties on MSN (Mal-/TCEP+; dark green or Mal-/TCEP-; magenta), only few nanoparticles are attached by non-specific adsorption on the cells.

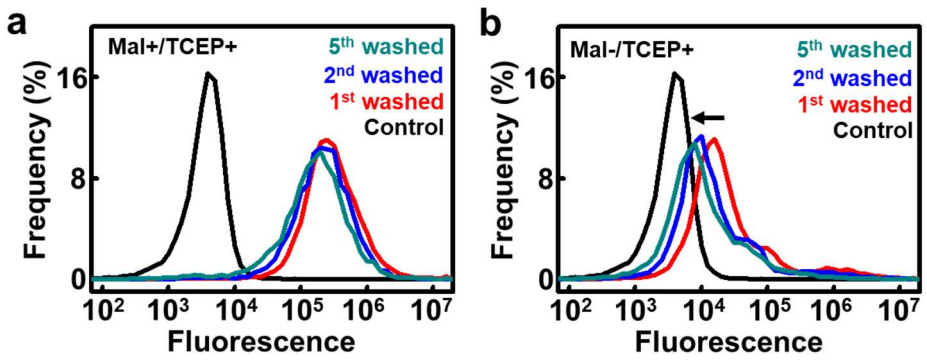

Figure 3.9. Measurement of fluorescent signal of MSN-attached cells, depending on the number of washing procedure. Measurement of fluorescent signal of MSN-adhered cells by (a) covalent conjugation or (b) non-specific adsorption. The fluorescent signals gradually decrease (black arrow), suggesting the detachment of MSN from the cells. All the fluorescent signal used here were from FITC conjugated to MSN.

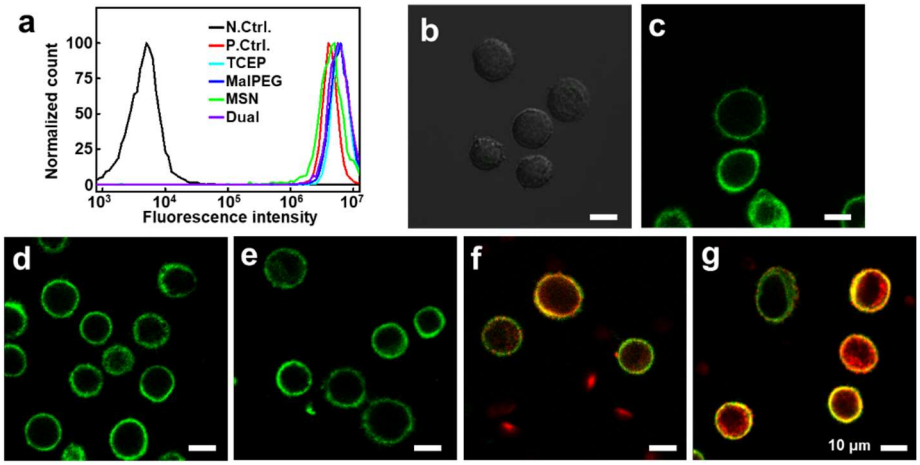

Figure 3.10. Analysis on effect of surface modification on cell surface accessibility. (a) Flow cytometry analysis and (b-g) confocal images of suspended Hela cells stained with CellMask, before or after cell surface modification (b: negative control (N.Ctrl., without CellMask staining), c; positive control (P.Ctrl., treated with cell mask before surface modification), d; TCEP treated (TCEP), e; Maleimide PEG coated cell (MalPEG), f; mesoporous silica nanoparticle coated cell (MSN), g; dual-coated cell (Dual, coated with MSN and MalPEG))

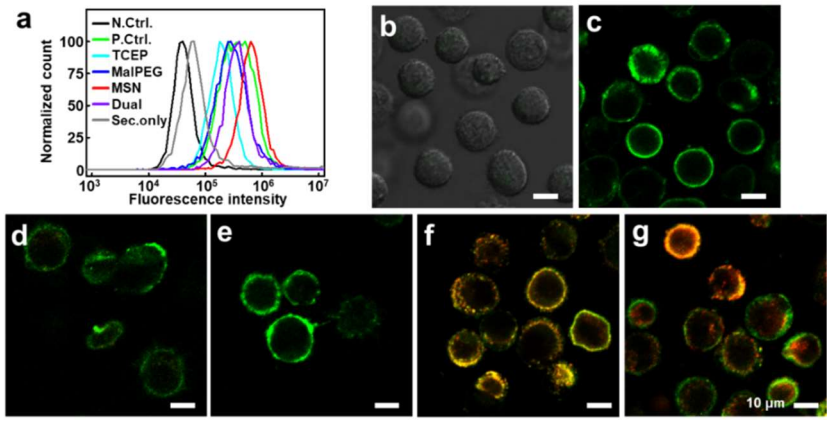

Figure 3.11. Analysis on the effect of surface modification on CD44-antibody attachment to HeLa cell. (a) Flow cytometry analysis and (b-g) confocal images of suspended HeLa cells stained with CD44 antibody before and after cell surface modification (b: stained only with FITC conjugated secondary antibody (Sec.only), c; positive control (P.Ctrl., stained with CD44 antibody and FITC conjugated secondary antibody before surface modification), d; TCEP treated (stained with CD44 antibody and FITC conjugated secondary antibody after TCEP treatment), e; Maleimide PEG coated cell (MalPEG), f; mesoporous silica nanoparticle coated cell (MSN), g; dual-coated cell (Dual, coated with MSN and MalPEG)). The fluorescent intensities of coated cells in flow cytometry analysis have a similar range of fluorescent intensities of uncoated cells, distinguished from negative control group.

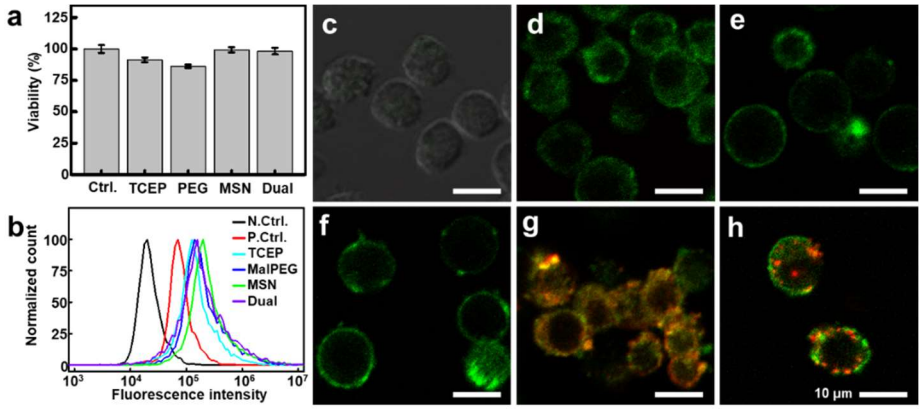

Figure 3.12. (a) Viability evaluation of macrophage cell line (RAW 264.7) depending on surface modification. (b-h) Analysis on the effect of surface modification on CD11b-antibody attachment to macrophage cell line (RAW 264.7). (b) Flow cytometry analysis and (c-h) confocal images of suspended RAW 264.7 stained with CD11b antibody before and after cell surface modification (c: negative control (N.Ctrl.), d; positive control (P.Ctrl., stained with FITC conjugated CD11b antibody before surface modification), e; TCEP treated (stained with FITC conjugated CD11b after TCEP treatment), f; Maleimide PEG coated cell (MalPEG), g; mesoporous silica nanoparticle coated cell (MSN), h; dual-coated cell (Dual, coated with MSN and MalPEG)). The fluorescent intensities of coated cells are distinguished from negative control group.

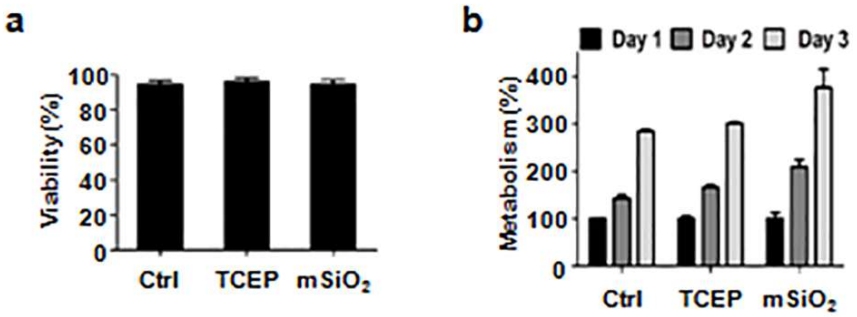

Figure 3.13. Viability and proliferation of MSN-coated Hela cells. a) Plot of cell viability examined by Live/Dead assay. b) Cell metabolism measurement by alamar Blue assay (n = 3 in a) and b)).

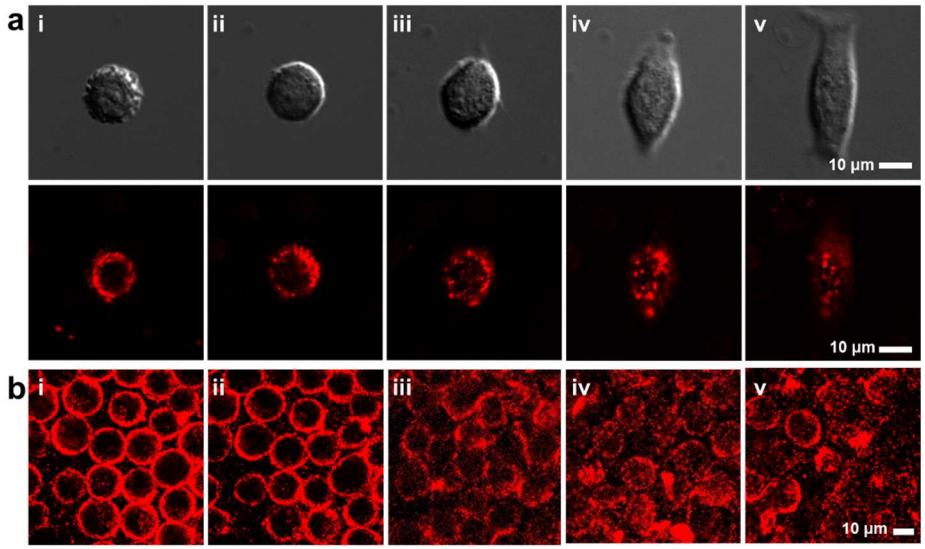

Figure 3.14. Confocal microscope images of MSN decorated onto anchored HeLa cell at different incubation times. (a) *In vitro* images of the cells coated with fluorescent MSN after (i) 3, (ii) 6, (iii) 9, (iv) 12, and (v) 15 hours of the membrane coating. (top: bright field images, bottom: fluorescence images). (b) intravital images of MSN coated cells applied subcutaneously after (i) 2, (ii) 4, (iii) 6, (iv) 12, and (v) 18 hours of the membrane coating and injection.

3.3.2 Tracking and early stage imaging with attached NPs

Using the MSN-coated cells, we performed two animal experiments including *in vivo* fluorescence imaging to track the location of cells and intra-vital microscopic imaging to visualize the early stages of cell therapy. Luciferase-producing HeLa cells were coated with near-infrared fluorescent MSNs and injected subcutaneously in the dorsal region of nude mice (**Figure 3.15**). Strong fluorescence from nanoparticles was observed where the cells were injected, co-localizing with the cellular luminescence, and it lasted for 8 days. Along with the early-stage intra-vital imaging of cells, we studied localized drug delivery using the drug-loaded MSNs to investigate the potential application of the MSN-coated cells for drug delivery.

To study drug diffusion *in vivo*, rhodamine was loaded into the MSNs. We also used fluorescence correlation spectroscopy (FCS) technique to analyze the fluorescence from dye-laden MSNs (**Figure 3.16** and **Figure 3.17**). As shown in the **Figure 3.16**, the fluorescein or rhodamine signals have correlation curves which exhibit two distinct diffusion time spans. The fast diffusion region of the curve is indicative of free dye molecules, and the slow diffusion time coincides with that of Cy5 conjugated MSN. It can be inferred that that some of the fluorescein and rhodamine

molecules are released from MSNs and freely moving, and others are retained within MSN. The results of FCS and confocal imaging suggest that a considerable portion of rhodamine is present within the MSN.

After coating HeLa cells with the rhodamine-loaded MSNs and confirming their coating with confocal microscope images (**Figure 3.18**), the cells were administered subcutaneously to nude mice and imaged with intra-vital confocal microscope. The red signal from the fluorescent MSNs delineated the round shapes of the coated surfaces, while green fluorescence derived from rhodamine diffused from the MSNs (**Figure 3.16**). Initially, most of the rhodamine molecules were distributed in the HeLa cells, but as time progressed, they gradually diffused to neighboring immune cells, upper muscle fibers, and finally, lower muscle fibers (**Figure 3.19** and **Figure 3.20**). The fluorescence signal diminished gradually, showing that rhodamine is steadily released and diffused from the injected area. The MSN-derived red signal and stability of MSN on the cell surface sustained over 18 h, clearly distinguishing the administered cells from the nearby immune cells and tissues (**Figures 3.14b**, **3.20**, and **3.21**) Some of the cells were destroyed by immune rejection, losing their red round shape.

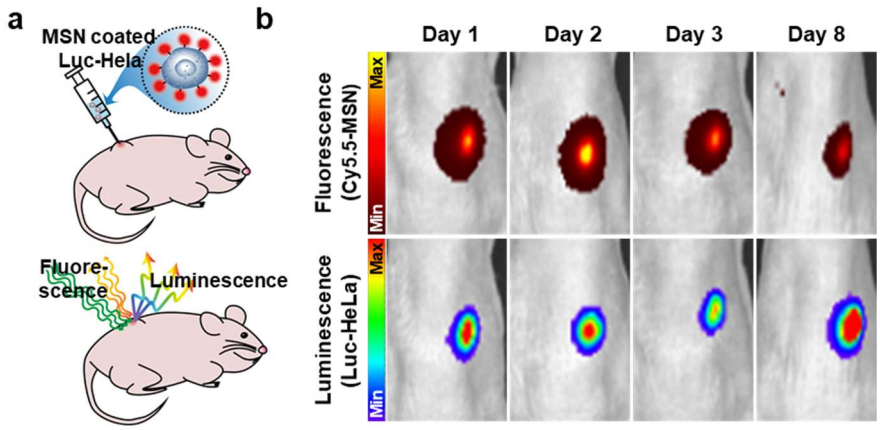

Figure 3.15. Tracking of luciferase-producing HeLa cells coated with near infrared-fluorescent MSN subcutaneously injected in mice. a) Schematic drawing of the tracking experiments. b) Fluorescence and luminescence imaging of nude mouse after injection of Cy5.5-MSN coated Luc-HeLa (luciferase expressing HeLa).

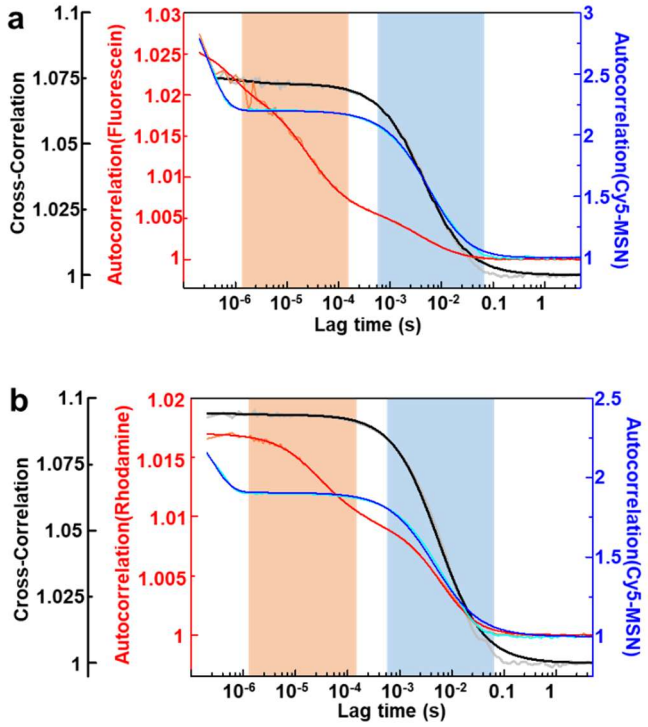

Figure 3.16. Fluorescence correlation spectroscopy analysis on fluorescent dye-loaded MSN. (a) Autocorrelation curve of fluorescein (orange) and its fitting curve (red), autocorrelation curve of Cy5 conjugated on MSN (cyan) and its fitting curve (blue), and cross-correlation curve between fluorescein and Cy5 (gray) and its fitting curve (black). (b) Autocorrelation curve of rhodamine (orange) and its fitting curve (red), autocorrelation curve of Cy5 conjugated on MSN (cyan) and its fitting curve (blue), and cross-correlation curve between rhodamine and Cy5 (gray) and its fitting curve (black). The shaded region remarks

two distinct diffusion times of free dye (pale red) and loaded dye (sky-blue). The autocorrelation curves of MSN and cross-correlation curves were fitted with single component normal diffusion model with triplet relaxation, and autocorrelation curves of fluorescein and rhodamine were fitted with double component normal diffusion model with triplet relaxation. The cross-correlation curves with the same diffusion time of MSN represents the bounded movement of fluorescein and rhodamine with Cy5 conjugated on MSN.

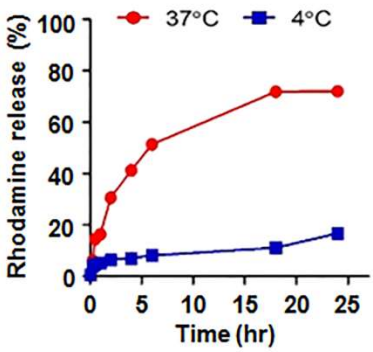

Figure 3.17. Release profiles of rhodamine, used as an alternative for small-molecule drugs, from rhodamine-loaded MSN, in function of time at two temperatures.

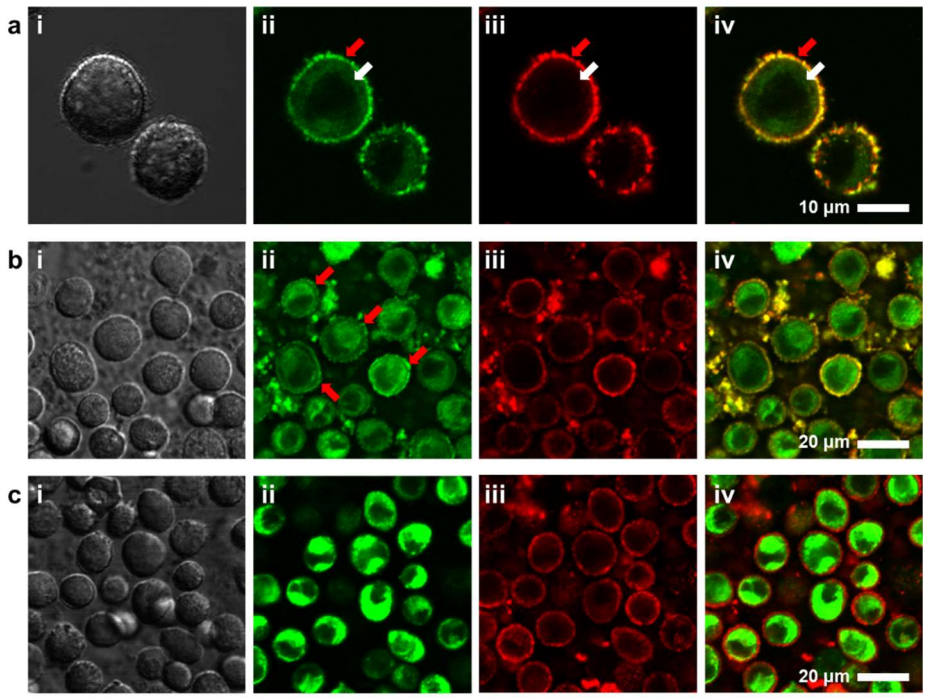

Figure 3.18. Confocal microscope images of dye-loaded MSN onto anchored HeLa cell membrane. (a) High magnified images, (i) bright field image, (ii) green fluorescent image from fluorescein locating in and around cell, (iii) Cy5 conjugated onto mesoporous silica, and (iv) merged image. (b) Low magnified image of the fluorescein loaded MSN, (i) bright field image, (ii) green as fluorescein, (iii) red as Cy5 on MSN, (iv) merged image. (c) Low magnified image of the rhodamine loaded MSN, (i) bright field image, (ii) green as rhodamine, and (iii) red as Cy5 on MSN. There is distinct colocalization on cell membrane of fluorescein and MSN, confirming that both fluorscein and Cy5 are present in MSN.

The red arrows point out the location of fluorescent dye molecules and MSN on membrane, and the white arrows point out the signals from dye molecule which are released and diffused into cytoplasm.

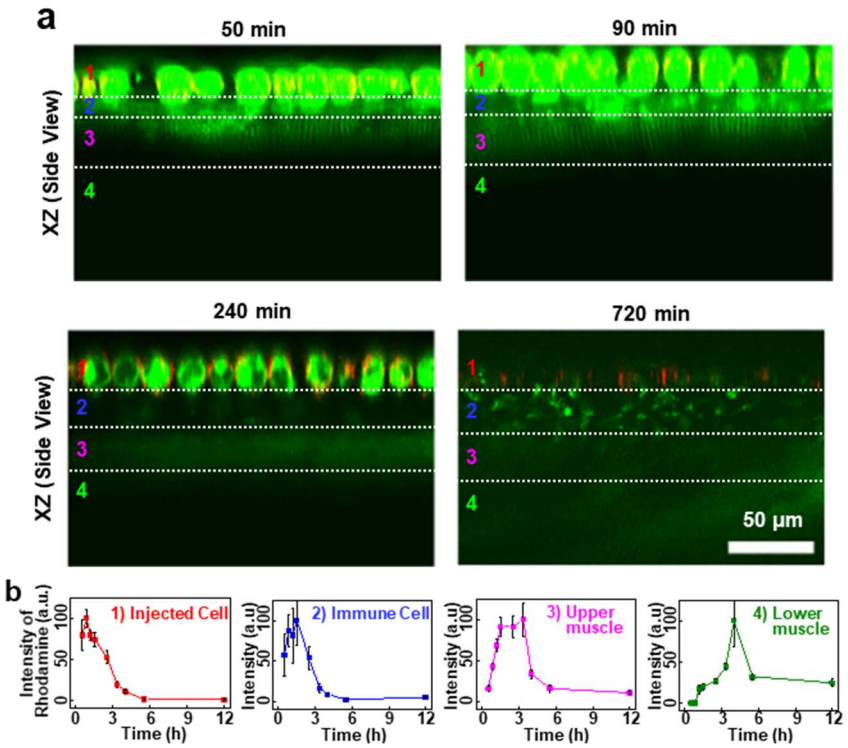

Figure 3.19. Intra-vital confocal image showing the rhodamine delivery (a) Time-lapse intra-vital imaging showing early stage of applied cells coated with rhodamine(green)-containing MSNs (red) on the muscle under subcutaneous layer. XZ-planes of images of administered cells neighbouring tissues. (b) Time-dependent variation of the rhodamine concentration in each tissue.

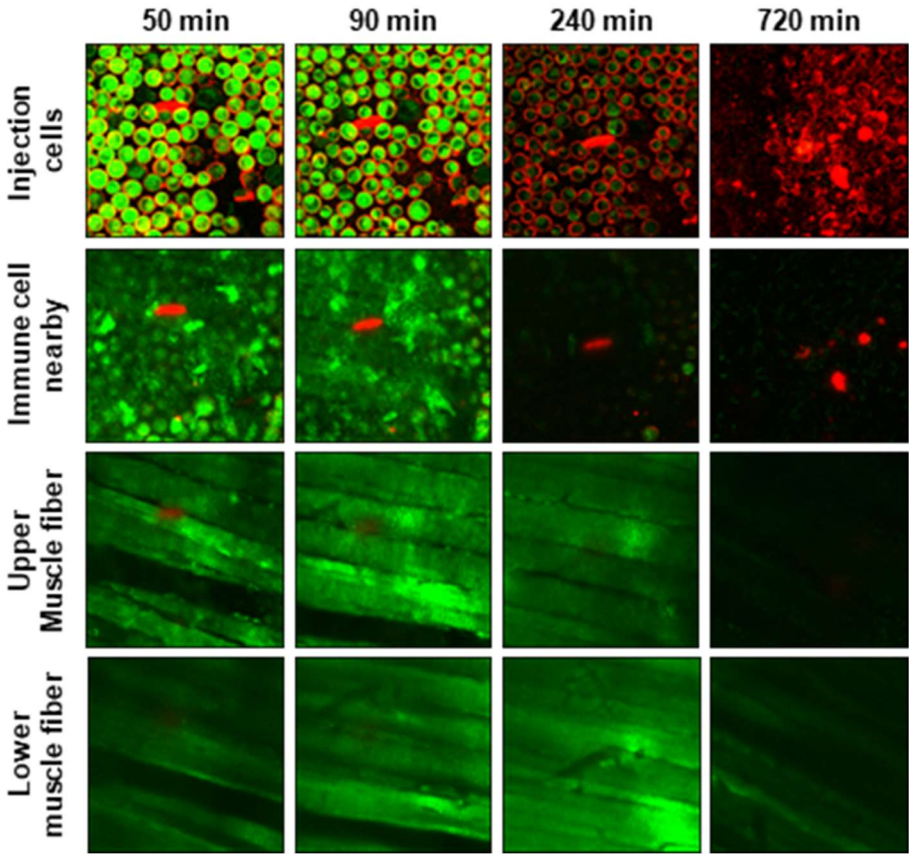

Figure 3.20. Intra-vital confocal image of cells coated with fluorescent MSNs. Administered on the muscle under subcutaneous layer. XY-planes of images of administered cells neighbouring tissues. Rhodamine (green) and Cy5-MSNs (red).

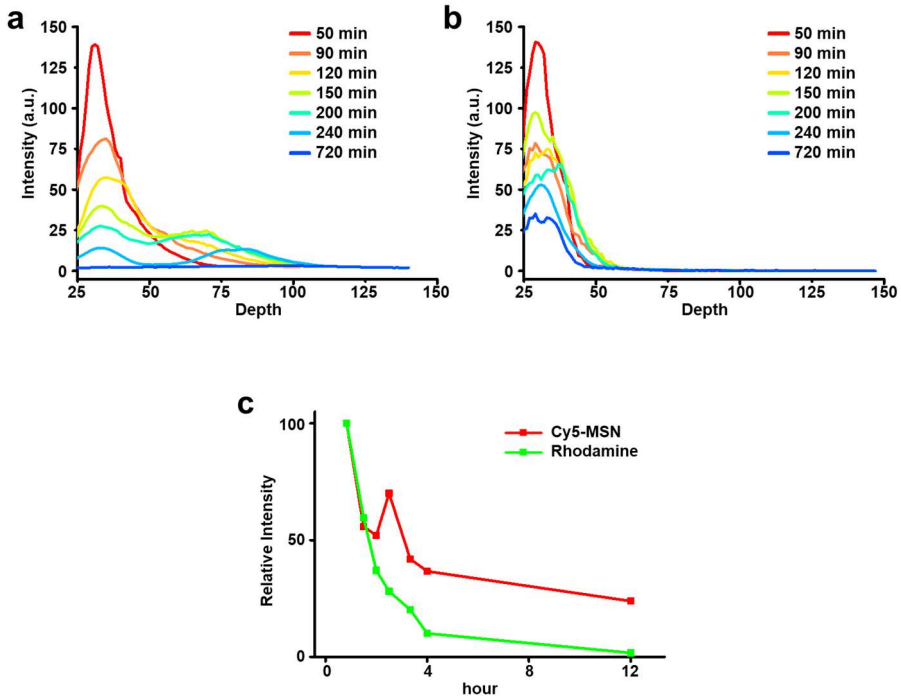

Figure 3.21. Average **i**ntensity profiles of fluorescent signals from (a) Cy5 conjugated on MSN and (b) rhodamine diffusing into tissue, depending on depth and time. Variation of intensity signals of the Cy5-MSN or rhodamine from treated HeLa cell.

3.3.3 Demonstration drug delivery and protection for cell therapy

We demonstrated that dual coating of drug-loaded nanoparticles and protective polymer can enhance the activity of implanted cells. Dexamethasone immunosuppressant was loaded into MSNs and used with maleimide-conjugated PEG to coat luciferase-expressing HeLa cells. The cells were subcutaneously injected to mice with normal immunity. Cellular activity was evaluated based on luminescence of the implanted cells.

As shown in **Figure 3.22** the activity of the administered cells was reduced gradually due to the innate immune rejection. The PEG coated cells have slightly higher activity after two days of post-injection, and MSN-coated cells also showed enhanced activities, compared with the uncoated cells. It shows that the immunosuppressant and PEG coating can protect the implanted cells by chemically and physically respectively. We also prepared the cells which have both polymer and nanoparticle coating onto cell surface. Notably, the polymer/nanoparticle dual-coated cells showed highly increased activities at two days post-injection and maintained higher activities than the other groups, suggesting the synergistic effect of the multiple coatings (**Figure 3.22**).

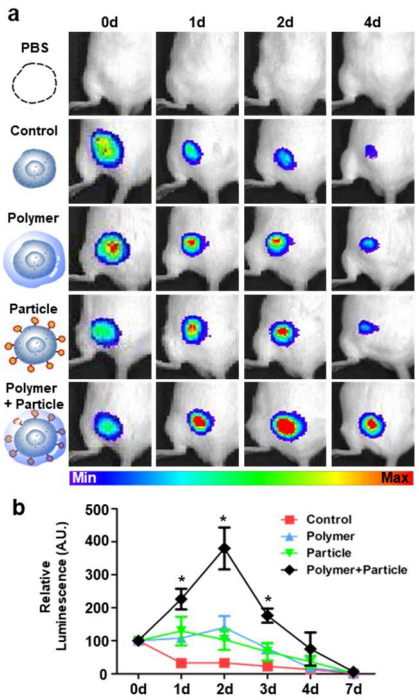

Figure 3.22. Enhancement of cellular activity of implanted cells with drug delivery vehicle and protective polymer coatings. Maleimide-PEG was used for polymer coating, and immunosuppressant (dexamethasone)-loaded MSN for NP coating. (a) Luminescence image showing the cellular activity after transplantation of non-treated, MPEG-coated, drug-loaded nanoparticle-coated, and MPEG/nano-particle dual-coated HeLa cells. (b) Comparison of luminescence intensity obtained at the indicated time points after cell transplantation (n=5, *$p<0.01$ versus control group at the same time point).

3.3.4 Discussion

Although there are previous reports which employ exogenous material on the cell surface for similar purposes, this method has definite advantages. The existing methods have limitations such as complicated preparation of coating materials, inability to coat individual cells, and the need for additional incubation time or microfluidic apparatus. Here in this section I would like to discuss the strength of our strategy in light of the existing coating methods.

(1) Coating with positively charged polymers

The slightly negative charge of the cellular membrane can be advantageous for the coating of positively charged polymers. Such idea is suitable for cell spheroids or cells attached on plate [4,9], but it is hard to coat the cells discretely in a suspension because it induces aggregation among cells. Using a large amount of positively charged polymers may reduce aggregation, but it can cause cytotoxicity to cells[43]. Our method can coat the biological cells separately with polymers or nanoparticles, preventing the aggregation of cells without adverse effect on a wide variety of cells.

(2) Coating with lipid derivatives or alkyl chain conjugated molecules

The hydrophobic double layer of cellular membrane has been the target site of exogenous material. Derivatives of lipid, alkyl-chain, and cholesterol are used to incorporate functional materials on the cell surface.[25] However, it is difficult to dissolve the macromolecules decorated with hydrophobic chains in physiological medium. Multiple hydrophobic chains attached to proteins would disrupt protein structure. Furthermore, the hydrophobic moiety grafted materials easily penetrate the cellular membrane., causing potential off-target interactions. Our method using conjugation of maleimide functional group does not compromise the solubility of macromolecules and nanoparticles, and allows the attached materials to remain in their position,

(3) Conjugation with amine-carboxylate functional group

Although functional groups using amine and carboxylic acid can be utilized in cell surface modification[27-29], there are several advantages of thiol-maleimide labeling over amine labeling of cell surface proteins.

Many biomacromolecules, proteins, and small molecular drugs contain amine and carboxylate groups. Both efficiency and specificity of the reaction between coating materials and target functional groups on cell surface can be affected by the formation of undesired amide bonding. Conjugation of amine and carboxylate groups also necessitates an extraneous activation of carboxylate using sulfosuccinimidyl ester and 1-ethyl-3-(3-dimethylaminopropyl)carbodiimide (EDC). After the amide bonding, byproducts including isourea or *N*-hydroxysuccinimide should also be removed. Conjugation between thiol and maleimide is free from byproducts or pre- or post-treatment processes and occurs in physiological condition. These features of thiol-maleimide coupling broaden the selection of the coating materials and drugs to deliver. We can apply various types of molecules and polymers to our surface modification method.

(4) Introduction of reactive functional groups through glycoengineering

Glycoengneering of the cells through metabolism of sialic acid or mannose is investigated to introduce desirable functional groups on the glycoproteins of cell surface.[30-32] However, these methods are time-

consuming, taking several days to induce and confirm the expression of the target moieties onto cells. The mild reduction and subsequent conjugation require about half an hour. As this method does not require any additional stabilization and culturing steps, it will be suited to cell therapy using primary cells, such as cancer immunotherapy and hematopoietic stem cell transplantation.

(5) Hydrogel coating using microfluidic channel

Mooney group reported the unique method to coat the cell surface with hydrogel using microfluidic channels.[15] However, it is only operable with the experimental setup with rigorous optimization. In this manuscript, we focus on generally accessible and facile procedures using well-known bioconjugation. This method is expected to be accessible to broader audience, even for those who are not thoroughly skilled with special apparatus such as microfluidic devices.

3.4 Conclusion

In conclusion, we demonstrated a universal and innocuous method of cell surface modification to impart various properties of exogenous materials to cells. As this method does not have any adverse effect and require any additional stabilization and culture steps, it is expected to be suitable for cell therapy using primary cells, such as cancer immunotherapy and hematopoietic stem cell transplantation. An examination of surface ligand and targeting capacity will be necessary prior to practical therapeutic applications, considering the nonspecificity of reduction using TCEP. Given the need for incorporation of materials onto cell surfaces to monitor cell therapy and produce artificial tissue, this versatile technique is anticipated to play a key role in next-generation cell-based therapies.

Most of the contents of this chapter will be published in the article, "General and Facile Coating of Single Cells via Mild Reduction." (*Journal of the American Chemical Society* **2017, 10.1021/jacs.7b08440.)

3.5 References

[1] A. A. Mangi, N. Noiseux, D. Kong, H. He, M. Rezvani, J. S. Ingwall, V. J. Dzau, *Nat. Med.* **2003**, *9*, 1195.

[2] M. A. Laflamme, K. Y. Chen, A. V. Naumova, V. Muskheli, J. A. Fugate, S. K. Dupras, H. Reinecke, C. Xu, M. Hassanipour, S. Police, C. O'Sullivan, L. Collins, Y. Chen, E. Minami, E. A. Gill, S. Ueno, C. Yuan, J. Gold, C. E. Murry, *Nat. Biotechnol.* **2007**, *25*, 1015.

[3] X. Huang, F. Zhang, H. Wang, G. Niu, K. Y. Choi, M. Swierczewska, G. Zhang, H. Gao, Z. Wang, L. Zhu, H. S. Choi, S. Lee, X. Chen, *Biomaterials* **2013**, *34*, 1772.

[4] J. T. Wilson, V. R. Krishnamurthy, W. Cui, Z. Qu, E. L. Chaikof, *J. Am. Chem. Soc.* **2009**, *131*, 18228.

[5] A. Singh, M. Corvelli, S. A. Unterman, K. A. Wepasnick, P. McDonnell, J. H. Elisseeff, *Nat. Mater.* **2014**, *13*, 988.

[6] T. Kim, E. Momin, J. Choi, K. Yuan, H. Zaidi, J. Kim, M. Park, N. Lee, M. T. McMahon, A. Quinones-Hinojosa, J. W. Bulte, T. Hyeon, A. A. Gilad, *J. Am. Chem. Soc.* **2011**, *133*, 2955.

[7] N. Lee, H. Kim, S. H. Choi, M. Park, D. Kim, H. C. Kim, Y. Choi,

S. Lin, B. H. Kim, H. S. Jung, H. Kim, K. S. Park, W. K. Moon, T. Hyeon, *Proc. Natl. Acad. Sci. U.S.A.* **2011**, *108*, 2662.

[8] X. Huang, F. Zhang, Y. Wang, X. Sun, K. Y. Choi, D. Liu, J.-s. Choi, T.-H. Shin, J. Cheon, G. Niu, X. Chen, *ACS Nano* **2014**, *8*, 4403.

[9] J. T. Wilson, W. Cui, V. Kozlovskaya, E. Kharlampieva, D. Pan, Z. Qu, V. R. Krishnamurthy, J. Mets, V. Kumar, J. Wen, Y. Song, V. V. Tsukruk, E. L. Chaikof, *J. Am. Chem. Soc.* **2011**, *133*, 7054.

[10] J. Y. Kim, B. S. Lee, J. Choi, B. J. Kim, J. Y. Choi, S. M. Kang, S. H. Yang, I. S. Choi, *Angew. Chem. Int. Ed.* **2016**, *55*, 15306.

[11] R. F. Fakhrullin, A. I. Zamaleeva, R. T. Minullina, S. A. Konnova, V. N. Paunov, *Chem. Soc. Rev.* **2012**, *41*, 4189.

[12] K. Tatsumi, K. Ohashi, Y. Teramura, R. Utoh, K. Kanegae, N. Watanabe, S. Mukobata, M. Nakayama, H. Iwata, T. Okano, *Biomaterials* **2012**, *33*, 821.

[13] J. Lee, J. Choi, J. H. Park, M. H. Kim, D. Hong, H. Cho, S. H. Yang, I. S. Choi, *Angew. Chem. Int. Ed.* **2014**, *53*, 8056.

[14] J. Niu, D. J. Lunn, A. Pusuluri, J. I. Yoo, M. A. O'Malley, S. Mitragotri, H. T. Soh, C. J. Hawker, *Nat. Chem.* **2017**, *9*, 537.

[15] A. S. Mao, J. W. Shin, S. Utech, H. Wang, O. Uzun, W. Li, M.

Cooper, Y. Hu, L. Zhang, D. A. Weitz, D. J. Mooney, *Nat. Mater.* **2017**, *16*, 236.

[16] W. Chen, L. W. Fu, X. Y. Chen, *J. Control. Release* **2015**, *219*, 560.

[17] M. T. Stephan, D. J. Irvine, *Nano Today* **2011**, *6*, 309.

[18] L. A. L. Fliervoet, E. Mastrobattista, *Adv. Drug Deliv. Rev.* **2016**, *106*, 63.

[19] M. T. Stephan, J. J. Moon, S. H. Um, A. Bershteyn, D. J. Irvine, *Nat. Mater.* **2010**, *16*, 1035.

[20] N. A. Rossi, I. Constantinescu, D. E. Brooks, M. D. Scott, J. N. Kizhakkedathu, *J. Am. Chem. Soc.* **2010**, *132*, 3423.

[21] Y. Teramura, H. Iwata, *Soft. Matter.* **2010**, *6*, 1081.

[22] Y. Takaoka, A. Ojida, I. Hamachi, *Angew. Chem. Int. Ed.* **2013**, *52*, 4088.

[23] J. L. Lilly, G. Romero, W. Xu, H. Y. Shin, B. J. Berron, *Biomacromolecules* **2015**, *16*, 541.

[24] T. Hayashi, Y. Yasueda, T. Tamura, Y. Takaoka, I. Hamachi, *J. Am. Chem. Soc.* **2015**, *137*, 5372.

[25] D. Rabuka, M. B. Forstner, J. T. Groves, C. R. Bertozzi, *J. Am. Chem. Soc.* **2008**, *130*, 5947.

[26] S. G. Sampathkumar, A. V. Li, M. B. Jones, Z. Sun, K. J. Yarema, *Nat. Chem. Biol.* **2006**, *2*, 149.

[27] D. Dutta, A. Pulsipher, W. Luo, M. N. Yousaf, *J. Am. Chem. Soc.* **2011**, *133*, 8704.

[28] N. A. Rossi, I. Constantinescu, R. K. Kainthan, D. E. Brooks, M. D. Scott, J. N. Kizhakkedathu, *Biomaterials* **2010**, *31*, 4167.

[29] H. Cheng, C. J. Kastrup, R. Ramanathan, D. J. Siegwart, M. Ma, S. R. Bogatyrev, Q. Xu, K. A. Whitehead, R. Langer, D. G. Anderson, *ACS Nano* **2010**, *4*, 625.

[30] L. K. Mahal, K. J. Yarema, C. R. Bertozzi, *Science* **1997**, *276*, 1125.

[31] S. T. Laughlin, J. M. Baskin, S. L. Amacher, C. R. Bertozzi, *Science* **2008**, *320*, 664.

[32] K. Kang, S. Joo, J. Y. Choi, S. Geum, S. P. Hong, S. Y. Lee, Y. H. Kim, S. M. Kim, M. H. Yoon, Y. Nam, K. B. Lee, H. Y. Lee, I. S. Choi, *Proc. Natl. Acad. Sci. U.S.A.* **2015**, *112*, E241.

[33] C. Metcalfe, P. Cresswell, L. Ciaccia, B. Thomas, A. N. Barclay, *Open Biol.* **2011**, *1*, 110010.

[34] J. C. Han, G. Y. Han, *Anal. Biochem.* **1994**, *220*, 5.

[35] T. L. Kirley, *Anal. Biochem.* **1989**, *180*, 231.

[36] J. J. Moon, B. Huang, D. J. Irvine, *Adv. Mater.* **2012**, *24*, 3724.

[37] H. Cheng, C. J. Kastrup, R. Ramanathan, D. J. Siegwart, M. Ma, S. R. Bogatyrev, Q. Xu, K. A. Whitehead, R. Langer, D. G. Anderson, *ACS Nano* **2010**, *4*, 625.

[38] G. Chen, H. Qiu, P. N. Prasad, X. Chen, *Chem. Rev.* **2014**, *114*, 5161.

[39] N. Lee, D. Yoo, D. Ling, M. H. Cho, T. Hyeon, J. Cheon, *Chem. Rev.* **2015**, *115*, 10637.

[40] Q. He, J. Shi, *Adv. Mater.* **2014**, *26*, 391.

[41] Y. Chen, H. Chen, J. Shi, *Adv. Mater.* **2013**, *25*, 3144.

[42] L. Pan, Q. He, J. Liu, Y. Chen, M. Ma, L. Zhang, J. Shi, *J. Am. Chem. Soc.* **2012**, *134*, 5722.

[43] D. Fischer, Y. Li, B. Ahlemeyer, J. Krieglstein, T. Kissel, *Biomaterials* **2003**, *24*, 1121.

Bibliography

1. Journal Publication

1) **Kwangsoo Shin**(*co-first author*)+, Jin Woo Choi+, Giho Ko+, Seungmin Baik, Dokyoon Kim, Ok Kyu Park, Kyoungbun Lee, Hye Rim Cho, Sang Ihn Han, Soo Hong Lee, Dong Jun Lee, Nohyun Lee*, Hyo-Cheol Kim*, and Taeghwan Hyeon*
"Multifunctional nanoparticles as a tissue adhesive and an injectable marker for image-guided procedures"
Nat. Commun. **2017**, 8, 15807.

2) Hyunbum Kim+, **Kwangsoo Shin**(*co-first author*)+, Ok Kyu Park+, Daheui Choi, Hwan D. Kim, Seungmin Baik, Soo Hong Lee, Seung-Hae Kwon, Kevin J. Yarema, Jinkee Hong, Taeghwan Hyeon*, and Nathaniel S. Hwang*
"General and Facile Coating of Single Cells via Mild Reduction"
J. Am. Chem. Soc. **2018**, 10.1021/jacs.7b08440.

3) Seungmi Ryu, Hyunbum Kim, Seokyung Kang, **Kwangsoo Shin**, Seon-Yeop Jung, Jiwoong Heo, Jin Han, Jeong-Kee Yoon, Ju-Ro Lee, Jinkee Hong, Kyung Hyun Ahn, Taeghwan Hyeon, Nathaniel Suk-Yeon Hwang*, and Byung-Soo Kim* "Reversible Cell Layering for Heterogeneous Cell Assembly Mediated by Ionic Crosslinking of Chitosan and Functionalized Cell Surface Membrane"
Chem. Mater. **2017**, 29, 5294.

4) Hyunjae Lee+, Changyeong Song+, Yong Seok Hong, Min Sung Kim, Hye Rim Cho, Taegyu Kang, **Kwangsoo Shin**, Seung Hong Choi, Taeghwan Hyeon*, and Dae-Hyeong Kim "Wearable/disposable sweat-based glucose monitoring device with multistage transdermal drug delivery module"
Sci. Adv. **2017**, 3, e1601314.

5) Hyo-Jun Lee+, Jun-Ho Ha+, Sang-Gyu Kim+, Han-Kyu Choi, Zee Hwan Kim, Yun-Jeong Han, Jeong-Il Kim, Youngjoo Oh, Variluska Fragoso, **Kwangsoo Shin**, Taeghwan Hyeon,

Hong-Gu Choi, Kyung-Hwan Oh, Ian T. Baldwin*, and Chung-Mo Park*

"Stem-piped light activates phytochrome B to trigger light responses in Arabidopsis thaliana roots"

Sci. Signal. **2017**, 9, ra106.

6) Jinkyung Park+, Suji Choi+, Ajit H. Janardhan, Se-Yeon Lee, Samarth Raut, Joao Soares, **Kwangsoo Shin**, Shixuan Yang, Chungkeun Lee, Ki-Woon Kang, Hye Rim Cho, Seok Joo Kim, Pilseon Seo, Wonji Hyun, Sungmook Jung, Hye-Jeong Lee, Nohyun Lee, Seung Hong Choi, Michael Sacks, Nanshu Lu, Mark E. Josephson, Taeghwan Hyeon*, Dae-Hyeong Kim*, and Hye Jin Hwang*

"Electromechanical cardioplasty using a wrapped elasto-conductive epicardial mesh"

Sci. Transl. Med. **2016**, 8, 344ra86.

7) Hyek Jin Kwon+, Moon-Yong Cha+, Dokyoon Kim, Dong Kyu Kim, Min Soh, **Kwangsoo Shin**, Taeghwan Hyeon*, and

Inhee Mook-Jung*
"Mitochondria-Targeting Ceria Nanoparticles as Antioxidants for Alzheimer's Disease"
ACS Nano **2016**, 10, 2860.

8) Mohammadreza Shokouhimehr+, Taeho Kim+, Samuel Woojoo Jun, **Kwangsoo Shin**, Youngjin Jang, Byung Hyo Kim, Jaeyun Kim, Taeghwan Hyeon*
"Magnetically separable carbon nanocomposite catalysts for efficient nitroarene reduction and Suzuki reactions"
Appl. Catal. A **2014**, 476, 133.

9) Kunsu Park, Jae Sung Son, Sung Ill Woo, **Kwangsoo Shin**, Min-Wook Oh, Su-Dong Park and Taeghwan Hyeon*
"Colloidal synthesis and thermoelectric properties of La-doped SrTiO3 nanoparticles"
J. Mater. Chem. A, **2014**, 2, 4217.

10) Radhu Subha, Venkatram Nalla, Jung Ho Yu, Samuel Woojoo

Jun, **Kwangsoo Shin**, Taeghwan Hyeon, C. Vijayan, and Wei Ji

"Efficient Photoluminescence of Mn2+-doped ZnS Quantum Dots Excited by Two-photon Absorption in Near-IR Window II"

J. Phys. Chem. C, **2013**, 117, 20905.

11) Soo Hong Lee+, Seung-Ho Yu+, Ji Eun Lee, Aihua Jin, Dong Jun Lee, Nohyun Lee, Hyungyung Jo, **Kwangsoo Shin**, Tae-Young Ahn, Young-Woon Kim, Heeman Choe, Yung-Eun Sung*, and Taeghwan Hyeon*

"Self-Assembled Fe3O4 Nanoparticle Clusters as High-Performance Anodes for Lithium Ion Batteries via Geometric Confinement"

Nano Lett., **2013**, 13, 4249.

12) Jung Ho Yu, Seung-Hae Kwon, Zdeněk Petrášek, Ok Kyu Park, Samuel Woojoo Jun, **Kwangsoo Shin**, Moonkee Choi, Yong Il Park, Kyeongsoon Park, Hyon Bin Na,

Nohyun Lee, Dong Won Lee, Jeong Hyun Kim, Petra Schwille, and Taeghwan Hyeon

"High-resolution three-photon biomedical imaging using doped ZnS nanocrystals"

Nat. Mater. **2013**, 12, 359.

13) Byung Hyo Kim, **Kwangsoo Shin**, Soon Gu Kwon, Youngjin Jang, Hyun-Seok Lee, Hyunjae Lee, Samuel Woojoo Jun, Jisoo Lee, Sang Yun Han, Yong-Hyeon Yim, Dae-Hyeong Kim, and Taeghwan Hyeon*

"Sizing by Weighing: Characterizing Sizes of Ultra-small-sized Iron Oxide Nanocrystals Using MALDI-TOF Mass Spectrometry."

J. Am. Chem. Soc. **2013**, 135, 2407.

14) Nohyun Lee+, Hye Rim Cho+, Myoung Hwan Oh+, Soo Hong Lee, Kangmin Kim, Byung Hyo Kim, **Kwangsoo Shin**, Tae-Young Ahn, Jin Woo Choi, Young-Woon Kim, Seung Hong Choi*, and Taeghwan Hyeon*

"Multifunctional Fe3O4/TaOx Core/Shell Nanoparticles for Simultaneous Magnetic Resonance Imaging and X-ray Computed Tomography"

J. Am. Chem. Soc. **2012**, 134, 10309.

15) Byung Hyo Kim+, Nohyun Lee+, Hyoungsu Kim, Kwangjin An, Yong Il Park, Yoonseok Choi, **Kwangsoo Shin**, Youjin Lee, Soon Gu Kwon, Hyon Bin Na, Je-Geun Park, Tae-Young Ahn, Young-Woon Kim, Woo Kyung Moon, Seung Hong Choi*, and Taeghwan Hyeon*

"Large-Scale Synthesis of Uniform and Extremely Small-Sized Iron Oxide Nanoparticles for High-Resolution T-1 Magnetic Resonance Imaging Contrast Agents"

J. Am. Chem. Soc. **2011**, 133, 12624.

2. Patents

1) Inventor: Taeghwan Hyeon, Hyo-Cheol Kim, **Kwangsoo Shin**, Jin Woo Choi, Giho Ko

"Synthesis of nanoparticles containing image-contrasting effect for tissue adhesive and image-guided marker"

- Country: Korea

- Application No.: KR1-1-2016-0997871-02

초 록

최소 침습시술은 최소한의 절개를 통해서 치료하여 염증과 합병증을 줄이고 환자의 회복속도를 빠르게 하여 다양한 분야의 침습적인 개방 수술을 대체하고 있다. 영상 장비와 시술 도구의 개발과 함께, 고감도의 표지물질과 시술 부위를 접합할 수 있는 무독성 접착제의 개발은 최소 침습 시술에서 매우 중요하다. 고감도의 표지물질은 시술 부위를 정확하게 파악 할 수 있도록 도와주고, 접착제는 시술 중에 발생한 손상 부위를 접합하게 도와준다. 또한 다양한 수술요법을 대체하여 각광을 받고 있는 세포 치료에서도 효과적인 고감도물질의 표지는 세포의 이식과 세포치료의 치료 효과를 관찰하는데 있어서 필요한 과정이다.

나노입자의 월등한 조영 효과와 생체적합성은 최소침습 시술에서 필요한 영상화를 돕기에 적합한 물질이다. 나노입자의 표면을 개질 하여 세포와 조직의 접착성을 증대시키는 방법은 세포 치료 전의 효율적인 세포 표지와 시술 중에 발생한 내부 상처 접합에 적합하다.

첫번째는 실시간 영상 장비에 적합하고 접착력이 우수한 나노입자의 개발에 대한 연구로, 탄탈륨 옥사이드의 표면을 개질하여 접착성질을 갖도록하고 실시간 영상 시술에서 사용하는 X-선 투시영상, X-선 전산화 단층촬영, 초음파 영상, 형광영상에서 이용 할 수 있도록 하였다. 탄탈륨 옥사의드의 표면을 얇은 실리카로 코팅하여, 분산도와 접착력을 확보하여, 기존에 개발되어 사용되고 있는 시아노아크릴레이트를 기반한 접착제와 비교하여 비슷한 수준의 접착력을 갖고있으며, 월등한 조영효과 또한 갖게 되었다. 이는 세포독성과 염증반응에 취약한 합성고분자의 단점을 또한 극복하여, 내부의 조직 장기에 사용하기에 적합하다. 이 물질을 통해 실시간 영상과, 수술 전 암과 같은 수술 부위를 표지하기에도 적합함을 동물실험을 통해 보여주었다.

다음은 세포 치료를 위한 세포 표지에 대한 연구로, 약물이 담재될 수 있고, 형광을 띌 수 있는 나노입자를 짧은 시간 내로 손쉽게 세포의 표면에 부착할 수 있는 방법에 대한 연구이다. 다공성 실리카 나노입자에 형광 물질을 부착하고, 이를 세포 표면에 안정적으로 부착을 함으로써, 장기간의 추적과 세밀한 관찰을 위한 생체내 현미경 영상을 할 수 있게

해 주었다. 기존의 세포 안에 흡수를 통해서 진행하는 표지 방법에 비해서 빠른 시간내에 진행 할 수 있었고, 또한 약물을 나노입자에 담재하여 국부적인 부위에 약물을 전달을 도모할 수 있었다. 이 세포 표면의 개질을 통하여 세포 치료의 초기단계에 대한 정보를 생검없이 실시간으로 보여주었고, 약물의 전달에 대한 정보를 얻을 수 있었다. 추가적으로 세포에 고분자와 면역억제제가 담재된 나노입자를 붙여, 면역거부반응을 극복하며 세포의 활성을 더 증진 시킬수 있었다.

주요어: 나노입자, 다기능성, 약물 전달, 나노바이오기술, 생의학적 응용, 최소침습시술, 접착제, 세포표면개질

학 번: 2011-22921